

**ATOMTRONICS: QUANTUM
TECHNOLOGY WITH
COLD ATOMS IN RING SHAPED
OPTICAL LATTICES**

DAVIT AGHAMALYAN

(MSc. (PHYSICS), YEREVAN STATE UNIVERSITY)

A THESIS SUBMITTED FOR THE
DEGREE OF DOCTOR OF PHILOSOPHY

CENTRE FOR QUANTUM TECHNOLOGIES
NATIONAL UNIVERSITY OF SINGAPORE

2015

**THIS THESIS IS DEDICATED TO THE
MEMORY OF MY FATHER, ALEXANDER
AGHAMALYAN.**

DECLARATION

I hereby declare that the thesis is my original work
and it has been written by me in its entirety. I have
duly acknowledged all the sources of information
which have been used in the thesis.

This thesis has also not been submitted for any
degree in any university previously.

Davit Aghamalyan

26 June 2015

Acknowledgments

First of all, I would like to thank my supervisor Prof. Leong Chuan Kwek for introducing me to many researchers and for including me in several collaborations. Here, especially, I would like to mention the collaboration with Luigi Amico and with the group of Rainer Dumke from NTU. I would also like to thank Prof. Kwek for the huge amount of optimism which he has been constantly supporting me during the 4 years of my PhD. He has always given me nice advice and suggestions regarding schools and workshops to attend.

Another person who has played a big role in my scientific life is Luigi Amico, a visiting professor at CQT who originally suggested the project on ring optical lattices. During the 4 years of my PhD program we have been in touch through Skype, email and simply by visiting each other. I have learned two most important qualities for being a successful researcher from him: patience and persistence. Luigi also showed me the beauty of many-body physics and formed my taste in numerical many-body physics. I would also like to thank him for involving me in a big collaboration with researchers from Grenoble, Germany and Italy and also for giving me opportunity to give a talk during the recent workshop on Atomtronics (where he was one of the organizers) in Benasque.

I would like to thank all my collaborators from whom I learned a lot. Here, especially, I would like to mention Marco Comminotti who has been sharing with me his deep knowledge in 1D systems and who always patiently answered all my questions. I would also like to thank Davide Rossini for critical viewing of my numerical results, and his intuition in many-body physics, which was very helpful for our common project which is introduced in Chapters 4 and 5. I would also like to thank Anna Minguzzi and Frank

Hekking for hosting my visit in Grenoble. That visit opened the whole new chapter in my scientific life. I am indebted to Anna for helping me with finding a Postdoc position.

I also want to thank all my group members for constantly supporting and encouraging me. Here I would like to mention Sai Vinjanampathy and Thi Ha Kyaw, who have been sharing with me their deep knowledge in numerical simulations. Sai helped me a lot with writing the code for exact diagonalization of the Bose-Hubbard model and Thi Ha provided me a code which gives the spectrum of a flux-qubit.

I would like to thank our admins Tan Hui Min Evon and Chui Theng who has been "faster than speed of light" in assisting me with all my inquiries and requests.

Finally, I would like to thank my mother Aida who has been supporting me during my PhD with all her kindness, devotion and positiveness.

Contents

Declaration	i
Acknowledgments	iii
Table of Contents	v
Summary	ix
List of Publications	xi
1 Introduction and Outline	1
2 Quantum technology devices realized with cold atoms trapped in potentials with closed geometries	9
2.1 Introduction	9
2.2 Cold atoms confined in toroidal trapping potentials	11
2.3 Methods for generation and for measurement of the neutral particle current in the ring geometries	14
2.4 Current-phase relation for the atomtronics SQUID devices .	20
2.5 Theoretical and experimental proposals towards realization ring lattices	24
2.6 Experimental realization of the ring-lattice potential with a weak link	27
2.7 Setup for adjustable ring-ring coupling	29
2.7.1 Realization with Laguerre-Gauss beams	30
2.7.2 Realization with SLM	33
2.7.3 Summary	35

3 Models for many-body bosonic systems confined in ring shaped optical potentials	37
3.1 Introduction	37
3.2 Bose-Hubbard model	38
3.2.1 Bose-Hubbard model for a single ring with a weak link	43
3.2.2 The model for two coupled rings	44
3.3 Lieb-Liniger model for a homogeneous ring with a delta-barrier	46
3.4 Luttinger model for a homogeneous ring with a delta-barrier	47
3.5 Gross-Pitaevskii equation for the AQUID	48
3.6 Theoretical analysis of macroscopic superposition states in the AQUID	49
3.7 Summary	56
4 Realization of qubits with ring optical lattices	59
4.1 Introduction	59
4.2 The physical system	62
4.2.1 Identification of the qubit: effective two-level system	64
4.2.2 Density profiles	70
4.3 Energy gap of the two-level current-flow system	71
4.3.1 Scaling with the system size	72
4.3.2 Dependence of the qubit energy spectrum on the filling factor in mesoscopic rings	74
4.4 Conclusions	78
5 Coherent superposition of current flows in the AQUID	81
5.1 Introduction	81
5.2 Momentum distributions	83
5.3 Optimal scaling of persistent currents for the AQUID	89

Contents

5.3.1	Scaling of persistent currents with a system size	92
5.4	Conclusions and Discussion	94
6	Interacting AQUIDs and quantum gates	97
6.1	Introduction	97
6.2	Two-rings-qubit	99
6.3	Real time dynamics: Two coupled Gross-Pitaevskii equations	101
6.3.1	Population imbalance and oscillation frequencies in the limit $\lambda\rho = 0$	104
6.3.2	Population imbalance and oscillation frequencies in the limit $\lambda\rho \ll 1$	105
6.3.3	Population imbalance and oscillation frequencies for the intermediate values of $\lambda\rho$	108
6.3.4	Population imbalance and oscillation frequencies for $\lambda\rho \rightarrow \infty$	109
6.4	MQST and phase space diagrams	110
6.5	Demonstration of the one- and two- qubit unitary gates .	113
6.5.1	Single qubit gates	114
6.5.2	Two-qubit coupling and gates	115
6.6	Conclusions	116
7	Conclusions and Outlook	119
Bibliography		123
A Appendix		135
A.1	Quasi one dimensionality and 1D s-wave scattering length .	135
A.2	Tonks-Girardeau gas	138

Contents

A.3	Exact solution in the limits of ideal and Tonks-Girardeau gas for the homogeneous ring with a delta-barrier	141
A.4	Luttinger liquid theory	143
A.4.1	The limits of weak and strong barrier for the homo- geneous ring with a delta-barrier	146
A.5	Gross-Pitaevskii equation	148
B	Appendix	151
B.1	Peierls substitution for the Bose-Hubbard ladder model . . .	151
B.2	Effective qubit dynamics for the AQUID	152
B.3	Effective qubit dynamics for a double-ring setup	156
B.4	Solution in terms of elliptic functions	160
C	Appendix	167
C.1	Momentum distribution for $\Lambda = 0$ and various interaction strengths	167
C.2	Momentum distribution for $U = 0$ and weak barrier limit . .	167
C.3	Derivation of the Energy gap with the WKB approximation	170
D	Appendix	173
D.1	Infinite interaction limit of BH model: $U \rightarrow \infty$	173
D.2	Exact diagonalization schemes	174
D.3	DMRG method	177

Summary

The context of the thesis is Atomtronics: circuits of laser light in which the flow of cold atoms can be manipulated through quantum optical means. Specifically, we studied systems composed of Bose-Einstein condensates trapped in a ring-shaped optical potential interrupted by a weak link. In this way, we provide a physical realization of the Atomtronics Quantum Interference Device(AQUID), the atomic analog of the celebrated SQUID realized with Josephson junctions. The promise is to harness the power of a macroscopic quantum phenomena with the typically low decoherence rates of cold atom devices. In this thesis, AQUID is envisaged as a platform for possible quantum simulation as well as acting as a core unit for the quantum technologies and quantum computation. Our AQUID presents an additional lattice confinement along the ring potential. The lattice is demonstrated to bring important added features. For our system: *(i)* We demonstrate that the effective dynamics of our AQUID is, indeed, governed by a two-level system, demonstrating that the AQUID indeed defines a qubit. *(ii)* We identify the set of parameters, like atom-atom interaction, strength of the weak link, size of a system, for which the AQUID can perform as a qubit. *(iii)* We studied our system as a quantum simulator *(iv)* We demonstrate how integrated Atomtronics circuits, in which different AQUIDs can interact with each other, can be constructed - we show, in particular, how one- and two-qubit gates can be realized.

List of Publications

Publications:

- [1] D. Aghamalyan, M. Cominotti, M. Rizzi, D. Rossini, F. Hekking, A. Minguzzi, L.C. Kwek, and L. Amico. “Coherent superposition of current flows in an Atomtronic Quantum Interference Device”, *New J. of Phys.* **17**, 045023 (2015).
- [2] D. Aghamalyan, L. Amico, and L.C. Kwek. “Effective dynamics of cold atoms flowing in two ring shaped optical potentials with tunable tunneling”, *Phys. Rev. A* **88**, 063627 (2013).
- [3] L. Amico, D. Aghamalyan, H. Crepaz, F. Auksztol, R. Dumke, and L.C. Kwek. “Superfluid qubit systems with ring shaped optical lattices”, *Scien. Rep.* **4**, 4298 (2014).
- [4] M. Cominotti, M. Rizzi, D. Rossini, D. Aghamalyan, L. Amico, L.C. Kwek, F. Hekking, and A. Minguzzi. “Optimal scaling of persistent currents for interacting bosons on a ring”, *Eur. Phys. Journ. Spec. Top.*, **224**, 3, 519 (2015).

CHAPTER 1

Introduction and Outline

Quantum technology is currently advancing towards realistic applications. There has been much progress in this direction by combining new ideas and techniques from several fields, including quantum optics, quantum information and condensed matter physics. Although devising new technological applications remains a major goal in the field, quantum technologies have granted us access to new physical regimes, uncovering new fundamental science [1]. Ultracold atoms loaded into optical lattices have been playing an important role in this context [2, 3, 4, 5]: they are perfect candidates for precise and easily accessible quantum simulators [6] and they could provide the insights and solutions to numerous existing puzzles and problems in fields other than quantum information science like condensed matter physics, astrophysics, high energy physics and material science as well as the engineering of new quantum phases of extended systems[7]; at the same time, they provide new devices for future technologies, like quantum cryptography, quantum metrology and quantum computation [2].

In recent years, methods to produce versatile potentials beyond conventional magnetic and dipole trapping arrangements have advanced steadily. The progress achieved in optical micro-fabrication has defined a new field - Atomtronics [7, 8] - where a variety of "optical circuits" of very different spatial shapes and intensities have been designed for atoms manipu-

Chapter 1. Introduction and Outline

lations, with a precision that nowadays approaches that of the most advanced lithographic techniques [9, 10, 11, 12]. Another feature that results from such a design would be a reduced decoherence rate due to the charge neutrality of the atomic currents, an ability to realize quantum devices with fermionic or bosonic carriers, and a tunable carrier-carrier interaction ranging from weak-to-strong, from short-to-long range, from attractive-to-repulsive interactions. Experimental Atomtronic implementations [13, 10, 14, 15, 16, 17, 18, 19, 20] promise to open up a new platform for quantum simulation. This may lead, in turn, to an improved understanding of electronic systems and consequently provide new impetus to the design of conventional circuits. Particularly important in the scope of the thesis are the Josephson junctions and the Superconducting Quantum Interference Devices (SQUIDs).

The Josephson effect is the phenomenon for which an electric current can flow without any voltage applied across a Josephson junction, two superconductors coupled by a weak link [21]. The effect arises due to the phase difference in the macroscopic wave functions of Cooper pairs in superconductors. Superconducting loops pierced by magnetic field and interrupted by weak links define the SQUID [22, 21]. Josephson junctions and SQUIDs are core units both for quantum simulators (as the Josephson junction arrays, indeed are[23]) and for quantum technologies like ultra-sensitive metrology [22, 21]. In principle, Josephson junctions can provide platforms for quantum computers, with a great potential for scalability [24]. In this context, two different configurations were realized. The first solution, providing the charge qubits, for which the logical bits are encoded in the surplus of charges (with respect to neutrality) in the superconducting islands. In the second solution, the logical qubits are flux qubits, with

the two states corresponding to the clockwise and anti-clockwise current flows along the arms of the SQUID. The serious challenge in such devices is decoherence. Although decoherence occurs following complex mechanism, [22, 24, 25], crudely speaking, it arises because of interactions between the electrical charges through long range Coulomb forces. For charge qubits, the main problem arises from dephasing due to background charges in the substrate; flux qubits are insensitive to the latter decoherence source, but are influenced by magnetic flux fluctuations that may be due to impaired spins proximal to the device[26].

As noted above, cold atoms promise to mitigate the decoherence problem. Quantum technology with cold atoms has been confined mainly to physical systems with open boundaries. In particular, several routes to quantum computation exploiting cold atoms confined to optical lattices in open boundaries have been proposed [3, 4, 5, 27]. In the standard design, the qubits are defined using the two lowest energy levels of the atoms. Notwithstanding the remarkable progress achieved so far [28, 29], atomic single-site addressing is a bottleneck for realizing quantum processing in a large scale structures. In such systems, decoherence occurs basically due to particle loss [3, 30]), and compared with the one based on Josephson junctions, this effect is easier to control in cold atom system since the degrees of freedom in many cold atom systems are, of course, neutral particles.

The scientific community has been devoting an outgrowing effort to combine the know-how developed on superconducting circuits with the new opportunities offered by cold-atom systems. The Josephson effect in cold-atom systems has been thoroughly analyzed. The set up essentially consists of two BECs, trapped in a double-well potential [31, 32, 33, 34, 30].

This thesis deals with cold atoms confined on optical lattice with closed

Chapter 1. Introduction and Outline

architecture [35, 36, 17, 37]. Our motivation is to extend the complexity of the physics that can be effectively addressed through cold atom quantum simulators. On the other hand, we want to draw the basis for novel designs for devices in quantum technologies. In the long run, we believe that we can overcome basic scientific challenges as well as to build a bridge from the scientific results to concrete engineering technologies.

We are primarily concerned with a BEC confined to ring-shaped lattice potentials, interrupted by weak links: barrier potentials created along the ring. The weak link acts as a source of backscattering for a condensate flowing along the ring, thus creating an interference pattern with the forward scattered current. Therefore, the configuration provides an atomic condensate counterpart of the rf-SQUID: the Atomtronic Quantum Interference Device (AQUID)(See [18, 38, 14, 39] for experimental realizations).

A number of comments are in order to explain the challenges presented by AQUID devices.

- To begin with, just because of the main virtue of our devices, the charge neutrality, it is not a trivial task to generate a current in the AQUID. There are three different methods for generating currents of the neutral particles at current disposal.

The first method is based on rotating the condensate in the system. The essential observation is that the Coriolis force for our system plays the role of the Lorentz force for charged particles [40, 41]. The rotation of the condensate is achieved by stirring the cloud of BEC by a well-focused, blue-detuned laser that does not interfere with the underlying optical rings, but capable of dragging the condensate [42, 43, 39, 14, 19]. The second method is based on a phase-imprinting technique [41, 44, 45, 46, 18]. The main idea is to make

use of Laguerre-Gauss beam and to transfer its orbital angular momentum to the atoms. This can be achieved by shining the condensate with two combined laser beams, one Gaussian and other one Laguerre-Gaussian [46, 18]. A two-photon Raman transition(between the internal states $|F = 1, m_F = -1\rangle$ and $|F = 1, m_F = 0\rangle$) coherently transfers \hbar angular momentum to the atoms due to the absorption of a photon in one beam and the stimulated emission of a photon in other beam. This method has been applied for ring systems with various configurations [46, 18]. The last method (in chronological order) exploits the so called geometrical artificial gauge fields [47]. Schematically, such a solution relies on the Berry's phase [48], that is acquired when a particle moves adiabatically around a closed contour in parameter space[49, 50, 35, 51]. The spatial or time dependent behavior of the phase and the intensity of a light beam or the detuning with respect to the atomic resonance can generate artificial magnetic and electric fields.

- The other challenge that is required to design AQUID's as quantum simulators and quantum devices is to let different AQUIDs interact in a tunable way.

In the present thesis we design a specific configuration to address such an issue. To achieve the goal, we rely on experimental progress in the field of micro-optics [9, 10]. The basic idea is to create ring-shaped lattice potential along a cylinder by means of a Spatial Light Modulator (SLM) and combine it with a couple of focused laser beams shined in a transverse direction to the cylinder with adjustable spatial period . Small periodicity of the lattice modulation is essential to achieve significant tunneling rates between neighboring sites and large

periodicity makes single-site manipulation and detection possible [52, 53].

The thesis is outlined as follows. In Chapter 2, we review experimental achievements [16, 17, 18, 14, 19] in the field of cold atoms trapped in toroidal potentials. Previous theoretical proposals and experimental achievements towards the generation of ring lattices are also reviewed [36, 35]. We explain, at length, about the necessary building blocks for an experimental realization of the AQUID. In particular, we address the questions like: How to realize toroidal trapping potentials? How to generate and measure currents of neutral particles in ring geometries? And finally, how to simulate atomic Josephson junctions? Then we focus on the systems which are playing the central role for this thesis. We introduce two different systems that are modeled with help of ring optical lattices. First one, is the ring lattice filled with cold atoms which has a weak link on one of the lattice sites and it is pierced by an artificial magnetic flux, the second one is a double-ring setup, that aims at introducing a tunable coupling between the rings. We also introduce our proposals and experimental results [54, 55] for engineering this kind of systems. In this chapter we also discuss how it is possible to realize coupled AQUID devices. Scaled ring-lattice potentials that could host, in principle, $n \sim 10$ of such ring-qubits, arranged in a stack configuration, along the laser beam propagation axis have been experimentally realized in Nanyang Technological University(in collaboration with Rainer Dumke's group).

In Chapter 3, we introduce 1D many-body bosonic systems to describe the systems introduced in Chapter 2, aiming at providing the necessary background for the content of the thesis. Here we introduce the following models: Bose-Hubbard, Lieb-Liniger, Luttinger liquid, Gross-Pitaevskii. We

formulate these models for two types of AQUID devices: ring lattice with a weak link; homogeneous ring which hosts a delta-barrier. In this chapter we also review theoretical proposals towards the generation of the superposition states of neutral current flows with the AQUID [56, 57, 58, 59].

In Chapter 4, we demonstrate how persistent currents flowing in a ring shaped optical lattice can provide a physical implementation of a qubit [35, 58, 60] in the limit given by the quantum phase model(namely, high number of atoms per lattice well). We find that the two-level system emerges at the specific value of external "magnetic flux"(referred below as a frustration point). It is shown that an effective action of the system is equivalent to the action of the solid state rf-SQUID [24]. We also study the two-level nature of the AQUID by going beyond the quantum phase model by exploring the Bose-Hubbard model with different numerical (exact diagonalization and DMRG) and analytical methods. We asses the quality of the qubit, in terms of its inner resolution and its separation from the rest of the many-body spectrum, across the different physical regimes. In order to achieve this goal, we examine the dependence of the qubit energy gap on the bosonic density, the interaction strength, and the barrier depth. Based on our analysis, we provide viable protocols to initialize and address the qubits.

In Chapter 5 we show how the superposition between current states appears in the momentum distribution (time-of-flight) images, which serves as a method for the qubit state readout. By combining different numerical and analytical methods we study TOF images as function of bosonic density, the interaction strength, and the barrier depth.

In the second part of this chapter we study the scaling of the persistent current with the system size for the homogeneous 1D ring which is inter-

Chapter 1. Introduction and Outline

rupted by the delta-potential and pierced with an artificial magnetic flux. Here we ask the following question: for which values of the interaction the amplitude of the persistent current decreases slowest with the system size? In Chapter 6 we study the *two-ring* setup introduced in the Chapter 2 [61, 52, 62, 63]. We demonstrate that in the limit of the quantum phase model, after integrating out microscopic degrees of freedom, an effective action of the system gives rise to the atomic analog of the specific solid state flux-qubit worked out by Mooij and coworkers [64, 65]. We analyze the time dynamics by reducing the Bose-Hubbard ladder model to the two-mode Gross-Pitavevskii equation description. We study the time dependent dynamics of the population imbalance in different regimes of interaction as well an effect of the Macroscopic Quantum Self Trapping(MQST) going beyond the regimes introduced in the Refs. [33, 34].

We study a specific device to realize two-qubit gates in the limit of the quantum phase model. We also show that arbitrary one-qubit rotations are feasible with AQUID devices.

In Chapter 7 we summarize all the results introduced in this thesis, mention the open problems and outline some future directions which in our opinion could be fruitful for the field of quantum technology with ring optical lattices.

CHAPTER 2

Quantum technology devices realized with cold atoms trapped in potentials with closed geometries

2.1 Introduction

Closed confined potentials can sustain atomic currents. The simplest geometry which allows to generate persistent currents is the toroidal optical trap filled with cold atoms [16, 17, 18]. In a quantum fluid confined on a toroidal geometry persistent current phenomenon occurs when the phase coherence length of the fluid extends to the whole system. The toroidal potential filled with cold atoms is a perfect testing platform for exploiting persistent/superfluid currents which can be generated with artificial gauge fields or simply by rotating the system.

The generation of current flows in AQUID systems is one of the building blocks for a qubit suggested in this thesis.

William Philips and his collaborators at the National Institute for Standards were the first to announce the successful experimental realization of the persistent current of cold atoms trapped in toroidal trapping poten-

Chapter 2. Quantum technology devices realized with cold atoms trapped in potentials with closed geometries

tials [66]. In a series of experiments, they have also studied the different physical properties (principally on the generation and the measurement of persistent currents) of the atomic analogue of the rf-SQUID, in which the weak link was realized by shining the system with strongly focused blue-detuned laser [18, 14, 19]. The current states have been created by rotating the weak link with a barrier height which is lower than the chemical potential, and the generated currents were probed via the time-of-flight measurements. In recent experiment, they also have demonstrated [39] an interferometric technique for the measurement of the amplitude and direction of the persistent current generated in the toroidal trap as well as in AQUID.

In this chapter we present our ring-shaped lattice AQUID. This set-up presents several advantages for the design of an AQUID(See for details Section 4.1). Ring lattice structures provide an easy route to realize interacting ring-ring architectures [55, 54]. One of the first proposals [35] on realization of ring optical lattices had already a hint in it, that it should be possible to realize many-ring coupling, since in [35] a stack of ring lattices has been obtained. In this chapter we suggest how to obtain a stuck of ring lattices or AQUIDs with tunable tunneling. This kind of device might be very relevant for quantum information since it can realize two-qubit gates and also can be used for the engineering complex Atomtronics devices [7, 8].

This chapter is outlined as follows. In Section 2.2 We review some experimental methods for generating toroidal traps [17, 18]. In Section 2.3 we summarize different experimental methods [18, 14, 19] for generating and measuring persistent current of neutral bosonic particles which are confined in ring potentials. In Section 2.4 we discuss current-phase relation in AQUID devices. In Section 2.5 we review different methods for

2.2. Cold atoms confined in toroidal trapping potentials

realizing ring optical lattices with help of Laguerre-Gauss beams [67, 35].

In Section 2.6 we elaborate in greater detail on how to realize ring optical lattice with a weak link with a spatial light modulator(SLM) [68, 69, 70].

In Section 2.7 we suggest different protocols for creating a potential which allows tunable ring-ring coupling. Finally, in Section 2.7.3 we summarize our results.

For the sake of clarity, it is worth noting that while the author of this thesis was involved in suggesting the experiments on ring lattices, the actual experimental work on realization of the ring lattices with SLM devices was done at Nanyang Technological University.

2.2 Cold atoms confined in toroidal trapping potentials

Toroidal trapping potentials have been made by combining magnetic traps with optical dipole barriers[66, 71]. However, these proposals have a major drawback: the ratio of the annulus length to the ring radius is not sufficiently small, which cause generation of vortices that were introducing heating of the BEC and consequently destroy the persistent current. We review here some of the advanced methods towards the generation of ring geometry "optical traps". For the dipole trap the Ac-Stark Potential U and the photon scattering rate S are given by the following expressions:

$$U \approx \frac{\hbar\Gamma^2 I}{8\Delta I_s} \quad S \approx \frac{\Gamma^3 I}{8\Delta^2 I_s} \quad (2.1)$$

here $\Delta = \omega - \omega_0$ and is the detuning from atomic transition with frequency ω_0 and linewidth Γ , and I_s is the saturation intensity. A variety of static and dynamic quasi-2 dimensional trapping potentials(which can be consid-

ered efectively 1d systems if conditions mentioned in the Appendix A.1 are satisfied) are realized using time-averaged tweezer beam which "paints" a desired potential for the BEC which is confined to a light sheet[17]. Typically, 5×10^5 ^{87}Rb atoms, which are in the state $5^2S_{1/2} |F = 2, m_F = 2\rangle$, are transferred into the horizontal light sheet ($\lambda = 1064\text{nm}$) with very high efficiency. The experimental false-color scheme is demonstrated on Fig.2.1 a). This light sheet has vertical and horizontal waists of 7.4 and $300\mu\text{m}$ as well as well depth of $10\mu\text{K}$. Condensates of the desired spatial shapes are created in the region of the intersection of the horizontal sheet and time-averaged tweezer beam which is switched on for 100ms after the initial step of 400ms of evaporation (also, the well depth of light sheet is linearly decreased) of cold atoms into the light sheet. The evaporation process is continued for the next 600 ms, while the tweezer is still on. In this way, the atoms are condensed into the desired combined dipole trap. As examples, we show in Figs.2.1 b) and e) the toroidal and ring lattice BECs obtained through such a process. The thickness of the annulus is smaller than $5\mu\text{m}$ (which makes these systems quasi one dimensional). By allowing several atomic clouds (created by the same method) to expand and overlap in typical time-of-flight type of experiments, formation of interferometric fringes were observed, providing a signature that the trapped cold atoms are condensates with negligible heating introduced by the time averaged potentials.

Another method which has been successfully implemented by the NIST group in a series of experiments [18, 14, 19] is based on Laguerre-Gaussian [72, 35] light beams. Laguerre-Gaussian beams possess phase singularity and the shapes are described by generalized Laguerre-Gauss polynomials LG_p^l . Each photon in this mode has an angular momentum of

2.2. Cold atoms confined in toroidal trapping potentials

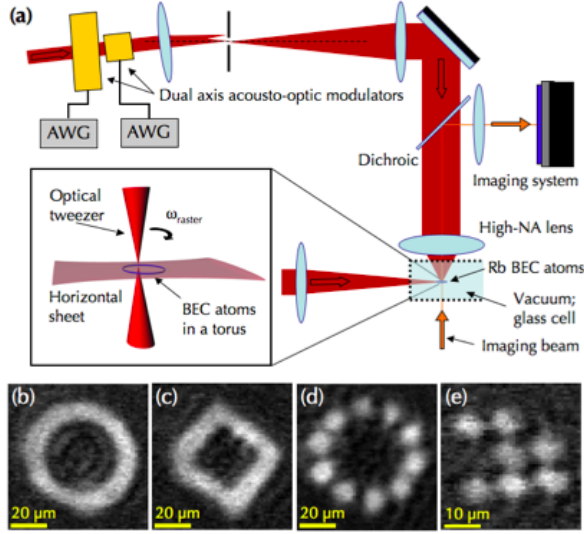


Figure 2.1: Experimental setup for the generation of arbitrary 2d trapping potentials a) An optical tweezer, which is controlled by dual axis acousto-optic modulator, is focused by a lens onto a sheet of light where Rubidium atoms are trapped b)-e) In situ absorption images of BECs which are trapped in toroidal, diamond, ring lattice and lattice with a defect optical confinements, respectively. Taken from [17].

$l\hbar$ and p is a number of radial nodes. In our discussion, the mode LG_1^0 is of particular importance. In polar coordinates (ρ, ϕ) , it has a torus structure given by:

$$LG_1^0(\rho, \phi) = \frac{2}{\sqrt{\pi}w_0^2}\rho e^{-\frac{\rho^2}{w_0^2}}e^{i\phi} \quad (2.2)$$

where the waist of a beam is given by $\sqrt{2}w_0$. Typical experimental setup(Fig.2.2) to create a toroidal trapping potential is achieved by combining a horizontal light sheet(with vertical half-width of $9\mu\text{m}$ and vertical half-width of $400\mu\text{m}$) with a vertical LG_1^0 beam(which had a radius of $\approx 20\mu\text{m}$). $3^2S_{1/2} |F = 1, m_F = -1\rangle$ ²³ Na atoms are first cooled close to the degeneracy in the magnetic trap and then transferred to the effective toroidal trap with help of evaporative cooling performed in the light sheet. A BEC with $\approx 3 \times 10^5$ atoms with a temperature $<10\text{nK}$ is then trapped in the toroidal potential with the vertical and radial frequencies $2\pi \times 550$

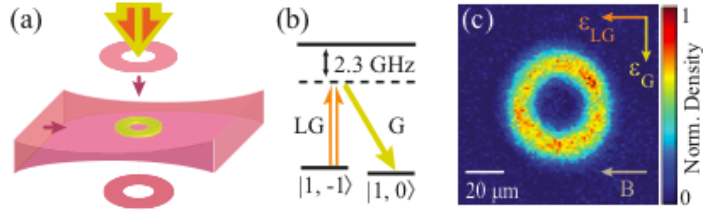


Figure 2.2: Experimental setup. a) generation of toroidal all-optical trap formed at the region of the overlap of two red-detuned beams: a horizontal "light sheet", and vertical Laguerre-Gaussian(LG_0^1) beam. Large downwards arrows show a pulsed pair of Raman beams b)atomic energy level structure and demonstration of Raman transition $|F = 1, m_F = -1\rangle \rightarrow |F = 1, m_F = 0\rangle$. One of the Raman beams is Laguerre-Gauss(LG_0^1) and the other one is GAussian. c) Absorption image of the toroidal BEC viewed from above. Arrows are showing polarizations of Raman beams and the direction of magnetic bias field. Taken from [18].

Hz and $2\pi \times 110$ Hz, respectively.

2.3 Methods for generation and for measurement of the neutral particle current in the ring geometries

Persistent currents (with lifetimes up to 40 s) with toroidal traps have been experimentally obtained by the NIST group[18]. To achieve the goal, pairs of pulsed co-propagating Raman beams (which are detuned 2.3 GHz below the D_2 line) were used[73], as shown on Fig. 2.2. The coupling to the state $|1, -1\rangle$ has been avoided with help of 0.5 mT externally applied magnetic field. The Raman beams have perpendicular polarizations. The Laguerre-Gauss beam has \hbar orbital angular momentum and the Gaussian beam possesses no angular momentum. The Raman process coherently transfers the atoms to the $l = 1$ current state. By optimizing the experi-

2.3. Methods for generation and for measurement of the neutral particle current in the ring geometries

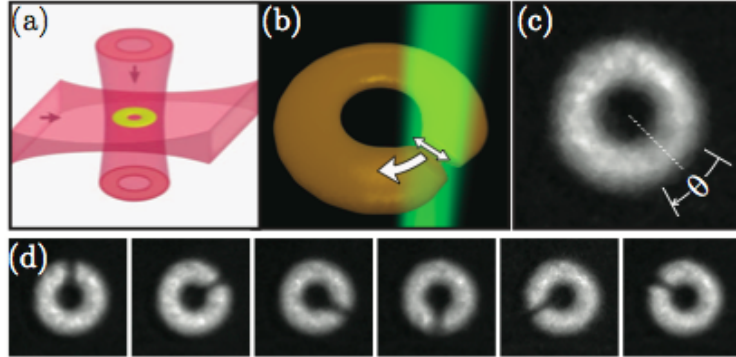


Figure 2.3: Experimental setup for creating a persistent current with the rotating weak link. a) generation of toroidal optical trap b) False-color picture demonstrating the barrier generation with rapidly moving blue-detuned laser($\lambda = 532nm$). Arrows are indicating radial and azimuthal movements of the Gaussian beam. c) In situ absorption image of the toroidal BEC viewed from above d) Sequence of in situ images demonstrating the rotation of the weak link on $\pi/3$ radians during each exposition. Strength of the barrier $U \approx 0.6\mu_0$. Taken from [14].

mental conditions, a minimum transfer efficiency of 90 percent is obtained and the remaining atoms(which are in the state $|1, -1\rangle$) are transferred to the state $|2, -2\rangle$ and subsequently removed from the trap with imaging light. Other method of current generation [14] can be realized with a rotating weak link as demonstrated on Fig.2.3. The rotating weak link, which is created by focusing a blue detuned laser, is rapidly moved in the radial and azimuthal directions(using 2-axis acoustic deflector) to create a time averaged effective potential. By focusing a blue-detuned beam, a spot with $8\mu m$ in diameter is obtained. By scanning a spot with acoustic deflector, wide and flat effective barrier is created. The barrier is rotated during 1.5 s at constant angular velocity $\Omega/2\pi < 3$ Hz, facilitating the generation of currents with winding numbers up to 3. During the first 0.5 s, the height of barrier has been increased linearly then is held constant for 0.5 s before it is linearly ramped down to zero. Consistent with the Heisenberg uncertainty principles, the particles located in the region of the weak link have

high velocities since the density is very small in that region. We arrive to the same conclusion by considering a hydrodynamical model and, since in the region of a weak link, the flow has smaller area, the velocities of the particles should be higher. Consequently, by rotating the weak link, more and more particles acquire high velocities.

As soon as atoms are trapped and cooled down, it is important to develop some methods to extract information about physical properties of the system. In the case of cold atoms, time-of-flight (TOF) imaging has been successfully used in several experiments[3]. In TOF measurement, demonstrated in Fig.2.4, the trapping potentials are switched off abruptly and the BEC starts to fall due to the gravity. As the BEC falls, the cloud expands due to the internal momentum of atoms. After it has fallen for some finite time t , an absorption image is taken. The spatial distribution of the BEC , obtained with a CCD camera, is related to the initial momentum distribution of the gas in the following way:

$$\langle n(\mathbf{x}) \rangle_{TOF} \propto \langle n(\mathbf{k}) \rangle_{init}, \quad (2.3)$$

where \mathbf{x} is related to \mathbf{k} by $\mathbf{k} = M\mathbf{x}/\hbar t$ according to the ballistic expansion assumption. Eq.(2.3) holds if interactions between particles during expansion process can be neglected.

The wave function of the condensate is given by $\psi(\mathbf{r}) = \sqrt{\rho(\mathbf{r})}\mathbf{e}^{i\phi}$, where ρ is the superfluid density and ϕ is the phase. The velocity of a superfluid is given by the gradient of the phase: $\mathbf{v}_S = \frac{\hbar}{m}\nabla\phi$. To satisfy the condition of single-valuedness, angular part of the wave function should be of the form $e^{in\theta}$, where θ is an azimuthal angle and n is an integer number(winding number). It is easy to see that the quantized behavior of the phase results in the quantization of the circulation:

2.3. Methods for generation and for measurement of the neutral particle current in the ring geometries

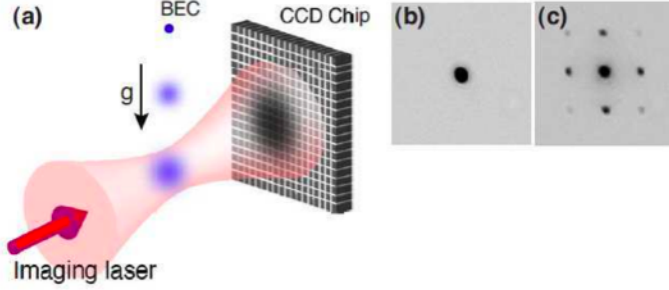


Figure 2.4: a) Experimental scheme for the TOF imaging b) an absorption imaging for the case of the harmonic trap c) an absorption imaging for the case of the optical lattice. Taken from[3].

$$\Gamma = \oint \mathbf{v}_S d\mathbf{l} = n \frac{\hbar}{m} \quad (2.4)$$

Now let us assume that current is generated in the narrow-toroidal confinement. Then current can be easily obtained from Eq.(2.4).

$$I = nv_S = nI_0 \quad (2.5)$$

where $I_0 = n\hbar/mR$, here n is the density of the condensate and R is the radius of the ring. As theoretically suggested in Ref. [35], an experimental signature of the current in TOF images is a ring structure of the absorption image and it is intuitive that there should be a correspondence between the size of the hole and the amplitude of the generated persistent current. This idea has been experimentally implemented by the NIST group [14]. The current is generated with the rotating weak link created by the blue-detuned focused laser. If there is no imprinted phase then there is no hole in the TOF image and the maximum of the density is observed at the central part of BEC (Fig.2.5 a)). When the rotation is applied with a rotating weak link, a hole appears at the center of BEC. However the states with

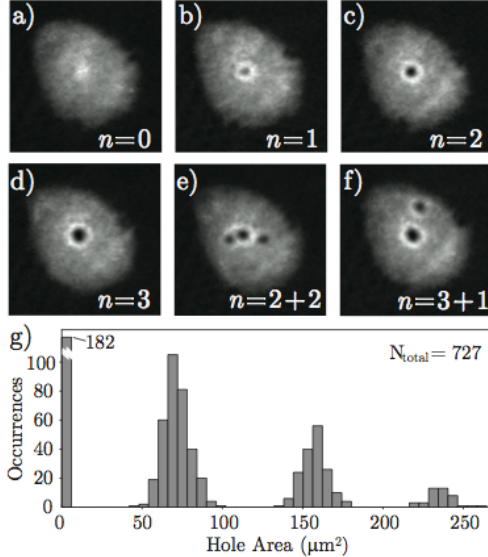


Figure 2.5: Experimental observation of different current flows a)-f) TOF images of the condensate after 10 ms expansion times. The images were observed on the 180 μm square g)Histogram showing grouping around discrete values of the hole area, which is a signature of the quantization of circulation in the ring. Taken from [14].

a winding number $n > 3$ become harder to observe due to the presence of vortices generated in the annulus(Fig.2.5 e) and f)). A major drawback of this kind of current measurement is that the direction of a current remains unknown. A histogram has been obtained after making 727 measurements and shown in Fig.2.5. Using this kind of diagram, the correspondence between the area of the hole and the winding number is obtained.

Recently, a new interferometric method has been suggested [39]. This new method has an added advantage of measuring the direction of the current flow. Indeed, currents with winding numbers up to 12 has been reported. The idea is to use two BECs, instead of one, and allow both of them to expand and overlap, generating interferometric pattern. One of the BECs is a disk shape and it is located in the middle of the toroidal BEC as it is shown on Fig.2.6. The interferogram measured in TOF images has

2.3. Methods for generation and for measurement of the neutral particle current in the ring geometries

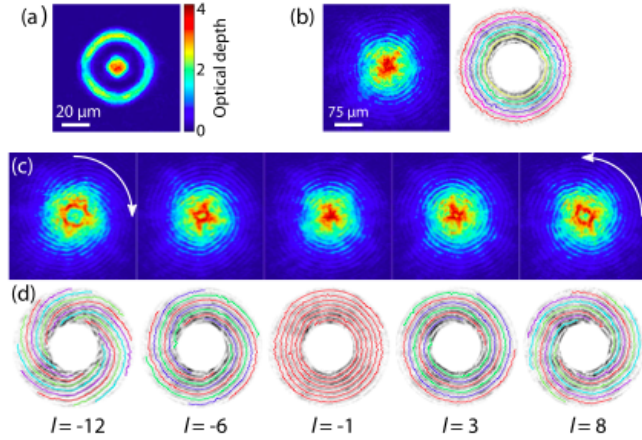


Figure 2.6: Interferometric method for the measurement of the generated current. a) In situ absorption of the toroidal and disk BECs b) TOF images of the resulting interference pattern of two BECs which are at rest c) Interferograms for different winding numbers d) obtaining the winding number and the direction of current from the number of spirals and their chirality, respectively. Taken from [39].

a different behavior for the cases of "rotating" and "non rotating rings". When there is no current in the ring, concentric rings are observed (Fig.2.5 b)) and if there is a non-zero winding number imprinted on the ring, then a spiral-like structure is generated in the interferograms (Fig.2.5 b) and c)). It turns out that the number of spirals gives the winding number and the chirality of spirals coincides with the direction of the superfluid current.

This behavior can be explained by analyzing the density $|\Psi|^2$ which results from the overlap of two BECs.

$$|\Psi|^2 = |\psi_D|^2 + |\psi_R| + \psi_D^* \psi_R + \psi_D \psi_R^* \quad (2.6)$$

The first term does not generate any fringe structure. As discussed, the second term produces a hole with a quantized size. However, the spiral structure appears because of the interference terms in Eq.(2.6). The interference terms depend on the azimuthal angle through dependence of

$\psi_R \propto \exp in\theta$. And the dependence on azimuthal angle disappears when there is no current in the ring ($n = 0$). We conclude that the interferometric technique allows us to measure both the magnitude and the direction of the superfluid current.

Read out of the angular momentum states can also be accomplished experimentally with interference of different flow states (i.e. corresponding to a fragmented superfluid) which maps the phase winding into a density modulation that can be measured using time-of-flight imaging[74].

2.4 Current-phase relation for the atomtronics SQUID devices

One of the added features of AQUID devices is the possibility to modify the current-phase relation, contrary to the solid-state counterparts where once the device is manufactured, its current-phase relation is fixed.

To understand different regimes of current-phase relation, it is important to introduce the notion of the healing length ξ . A healing length describes the distance over which the wave function tends to its bulk value when subjected to a localized perturbation and for the weakly interacting gas it is given by:

$$\xi = \frac{1}{\sqrt{8\pi n a}} \quad (2.7)$$

This equation shows that healing length is an interaction-induced effect and as the interaction strength or density increases, the healing length decreases. Depending on the relation between the width of the barrier ε and the healing length ξ , different current-phase relations can be achieved. In Ref. [75], an experimental realization of an atomic analogue of the dc-SQUID has been realized with help of the setup shown on Fig. 2.7. As

2.4. Current-phase relation for the atomtronics SQUID devices

seen from the intensity distribution of the ring trap, this system has two barriers (atomic Josephson junctions) which can be moved circumferentially towards each other with rotation frequency f . This system can be modeled as two condensates connected by a single Josephson junction. If N_1, N_2 and ϕ_1, ϕ_2 are the total atom numbers and the phases of the two condensates on the two sides of torus respectively, then it is convenient to define the population imbalance as $z = (N_1 - N_2)/(N_1 + N_2)$ and the phase slip across the junction $\phi = \phi_1 - \phi_2$. It can be shown [76] that the time dynamics of the system is governed by the following Josephson equations:

$$\begin{aligned}\dot{z} &= I_c \sqrt{1 - z^2} \sin \phi \\ \dot{\phi} &= -\omega_C(z - z_0) - I_c \frac{z}{\sqrt{1 - z^2}} \cos \phi\end{aligned}\quad (2.8)$$

Here $I_c = 2E_J/\hbar N$ and $\omega_C = E_C/s\hbar N$, where $N = N_1 + N_2$, E_J is the Josephson coupling energy, and E_C is the capacitance energy. E_J and E_C can be expressed as the integrals over the wave functions of two BECs (when the so-called two mode approximation is applied [76]). The bias current $z_0 = 4f$ is created by moving the Josephson junctions against each other and the normalized current at the junction is given by \dot{z} . A good agreement has been demonstrated between Eqs.(2.8) and experimental results for the final population imbalance. These equations predict sinusoidal current phase relation for small values of z . However, in this experiments $\varepsilon \approx 2\mu m$ and $\xi \approx 0.5\mu m$, which means that the healing length and the barrier height were roughly of the same order. However, if $\varepsilon \gg \xi$, then system is operating in so-called "hydrodynamic" regime and the current-phase relations becomes almost linear. This effect is clearly seen on Fig.2.8, which is obtained by an experimental measurement of the current I_{WL} as a function of the phase slip γ for the atomic rf-SQUID. In these experiments,

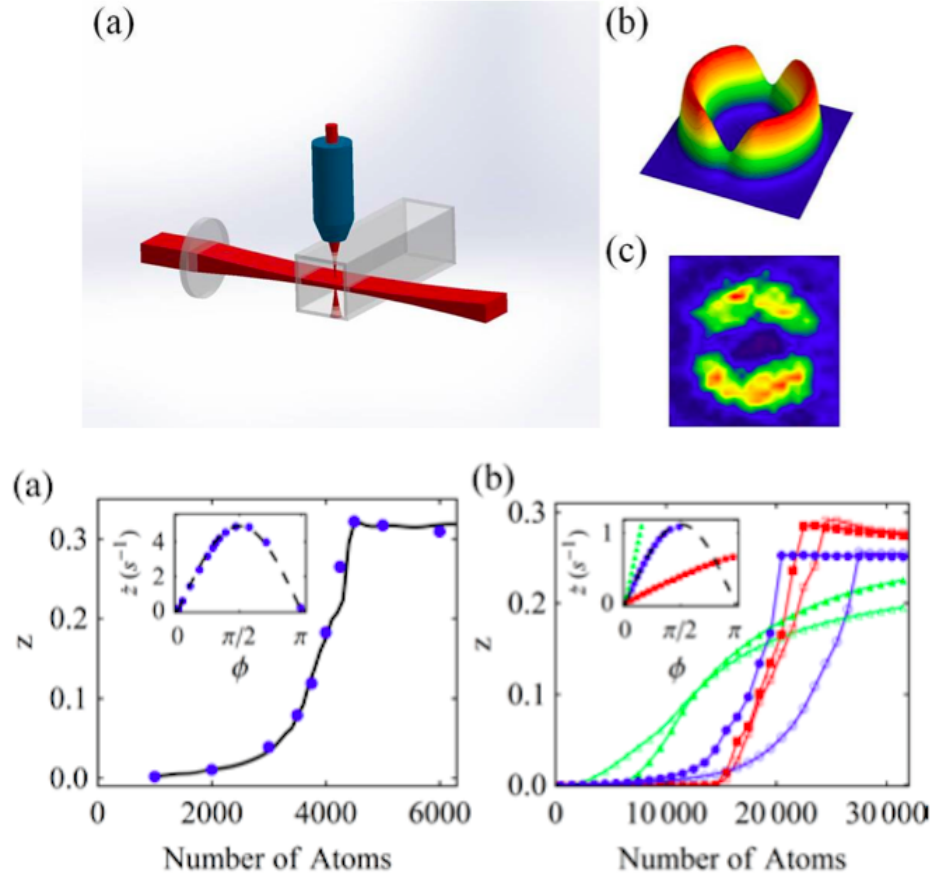


Figure 2.7: Upper panel: a) The scheme of the experimental setup, explained in section 2.2. b) Calculated potential for realizing an atomic dc-SQUID which has $8\mu\text{m}$ diameter c) In situ absorption image of an atomic dc-SQUID. Lower panel: a) Final value of the population imbalance z for $f = 1\text{Hz}$ as a function of the total number of atoms calculated using the Josephson equations(solid lines) and 3D GP simulations(disks). Inset shows current-phase relation obtained by GP simulations(disks) and ideal current-phase relation(dashed line) $\dot{z} = 2E_J/\hbar N \sin \phi$. Here $N = 4250$ and the ring radius is $4\mu\text{m}$. b) 1D GP simulations for the ring with radius $20\mu\text{m}$ and $N = 22000$. Calculations are done for the following set of width of the barrier(in the units of the healing length) and height of the barrier(in the units of the chemical potential): 3.9 and 1.8(disks), 37 and 0.93(squares), and 36 and 0.51(triangles). Inset: same as in Inset in the a). Taken from [75].

2.4. Current-phase relation for the atomtronics SQUID devices

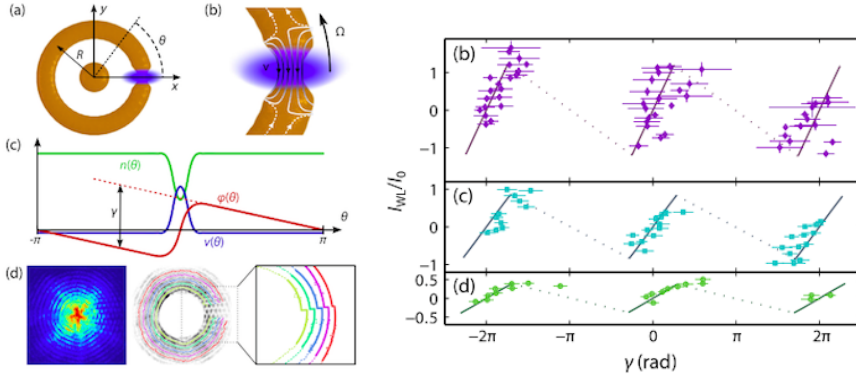


Figure 2.8: Left panel: a) atoms in the trap with a weak link b) the velocity field of the rotating atoms which are going through the weak link. c) Typical density $n(\theta)$, velocity $v(\theta)$ and phase of the condensate $\phi(\theta)$ as a function of azimuthal coordinate θ for the system. Phase slip across the weak link is given by γ . d) an interferogram obtained with the same method explained in the previous section. Right panel: current-phase linear relation for three different weak link barrier heights: b) $0.45\mu_0$ c) $0.6\mu_0$ d) $0.7\mu_0$. I_{WL} is the current in the system rotating with the weak link, and $I_0 = n_{1D}R\Omega_0 \approx 5 \times 10^5$ atoms/s. The solid curves represent the results of the theoretical model. Taken from [39].

$$\xi \approx 0.3\mu m \text{ and } \varepsilon \approx 6\mu m.$$

The ability to modify current-phase relations by changing the width of a barrier has been numerically evidenced in [75] for the setup depicted on Fig. 2.7. The figure clearly demonstrates that in the limit when healing length is of the same order as the barrier width, a sinusoidal current-phase relation is obtained (see inset of the Fig. 2.7 a)), and an almost linear current-phase relation results when $\varepsilon \gg \xi$ (see triangles and squares on the inset of Fig. 2.7 b)). We also conclude that thin and thick barriers behave differently. Specifically, it is found that as the total number N increases, flow for the thick barrier starts only if the chemical potential is bigger than height of a barrier, contrary to the case of the thin barrier, where current can be created in the system even if chemical potential is smaller than height of the barrier.

2.5 Theoretical and experimental proposals towards realization ring lattices

As it was discussed in the section 2.2 a variety of static and dynamic quasi-2 dimensional trapping potentials, including ring lattices, are realized using time-averaged tweezer beam which "paints" a desired potential for the BEC, which is confined to a light sheet[17].

However, early proposals and protocols to realize ring lattices were based on the Laguerre-Gaussian beams which have cylindrical symmetry. The electric field , with a frequency ω , a wave vector k and an amplitude E_0 , which is propagating along the z axis, can be written for LG beams in cylindrical coordinates (r, ϕ, z) as $E(r, \phi, z) = E_0 f_{pl}(r) e^{il\phi} e^{i(\omega t - kz)}$, $f_{pl}(r) = (-1)^p \sqrt{\frac{2p!}{\pi(p+|l|)!}} \varepsilon^l L_p^{|l|}(\varepsilon^2) e^{-\varepsilon^2/2}$, $\varepsilon = \sqrt{2r/r_0}$, where r_0 is the waist of the beam and $L_p^{|l|}$ are associated Laguerre polynomials $L_p^{|l|}(z) = (-1)^m d^m/dx^m [L_{n+m}(z)]$, with $L_{n+m}(z)$ being the Laguerre polynomials. The numbers p and l label the radial and azimuthal quantum-coordinates. In this thesis we will consider only the case of $p = 0$. For this case $L_0^{|l|}(z) = 1$, $f_{pl}(r) = f_l(r) = \sqrt{\frac{2}{\pi|l|!}} \varepsilon^l e^{-\varepsilon^2/2}$ and the expression for the electric field takes form:

$$E(r, \phi, z) = E_0 \sqrt{\frac{2}{\pi|l|!}} \varepsilon^l e^{-\varepsilon^2/2} e^{il\phi} e^{i(\omega t - kz)} \quad (2.9)$$

The intensity profile reaches the maximum value $I_{max} = \sqrt{\frac{2}{\pi^3 l!}} I$ (this result improves with increasing l) at $r_{max} = r_0 \sqrt{\frac{|l|}{2}}$. Here $I = P/\pi r_0^2$, where P is the power of the laser. The electric field in the radial direction has a full-width-half-maximum (FWHM) of $\sqrt{2 \ln 2} r_0$. In Ref. [35] it has been suggested that ring lattice can be generated as a result of interference of

2.5. Theoretical and experimental proposals towards realization ring lattices

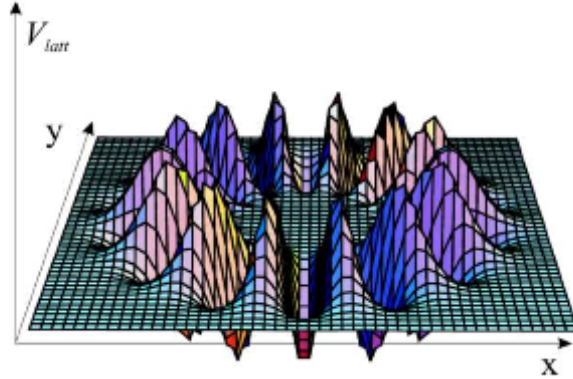


Figure 2.9: The optical potential resulting from the interference of a plane wave with an LG mode with $l = 14$. Taken from Ref. [35].

two counter-propagating pair of LG beams and plain waves. As a result, a stack of ring lattices is obtained and each of rings of the stack is a ring lattice with l wells as it is shown on Fig.2.9. The resulting light field intensity for this configuration takes form:

$$I(r, \phi, z) = 4E_0^2(1 + f_l(r) + 2f_l(r)\cos(l\phi))\cos(kz)^2 \quad (2.10)$$

It is important to point out that since tunneling between the rings can be made much smaller than intra-ring tunneling(this can be achieved by controlling the ratio r_0/λ), in principle it is possible to consider one isolated ring out of the stack. However filling only one ring with cold atoms can be experimentally challenging.

A similar approach has been experimentally implemented in Ref. [36] by making use of the interference of two counter-propagating LG beams which have different azimuthal numbers l_1 and l_2 . This kind of interference leads to the ring lattice which has $\delta l = l_2 - l_1$ wells. An added feature of this method is the fact that if the beams have frequency shift $\delta\omega$ then the resulting potential is rotating with an angular velocity $\delta\omega/\delta l$. The result-

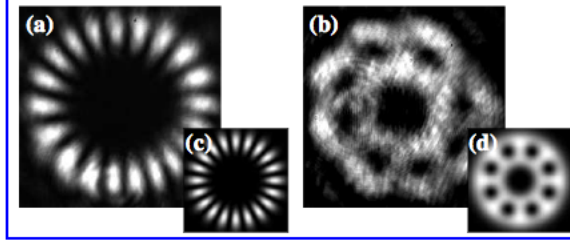


Figure 2.10: Intensity distribution for the bright and dark ring lattices: a) the bright lattice generated by overlapping two LG beams with $l_1 = -l_2 = 10$ and with equal intensities b) a theoretical prediction for a) c) dark lattice generated by overlapping two LG beams with $l_1 = 3$ and $l_2 = 11$ and with $I_2 = \sqrt{l_2/l_1}I_1$ d) theoretical prediction for b). Taken from Ref. [36].

ing intensity of two counter propagating beams, with different azimuthal numbers and different frequencies is given by:

$$I = E_0^2(f_{l_1}(r)^2 + f_{l_2}(r)^2 + 2f_{l_1}(r)f_{l_2}(r)\cos(\delta l\phi - \delta\omega t)) \quad (2.11)$$

A complete constructive or destructive interference happens at a radius where both beams have equal intensity. For generating bright lattices a simple choice is $l_1 = -l_2 = l$ and $I_1 = I_2$. In this case two beams have the same radial intensity distribution(see Fig.2.10 a) and c)). If l_1 and l_2 are different then two beams reach the maximum of intensity for different values of the radius. However, by choosing $r_{l_1} - r_{l_2} = \sqrt{2 \ln 2}r_0$ and $I_2 = \sqrt{l_2/l_1}I_1$, one can obtain dark lattices (See Fig.2.10 b) and d)) with an approximately uniform depth in the radial and azimuthal directions. It is useful to consider a specific example for the $D2$ transition of ^{87}Rb which has the following parameters: $\Gamma = 2\pi \times 6MHz$, $\lambda = 780nm$ and $I_S = 16.3W m^{-2}$. For the laser with the power $2W$, which has a beam waist $r_0 = 30\mu m$ the wavelengths of $1064nm$ and $660nm$ can be used for trapping the atoms in the bright and dark lattices, respectively. For the bright lattice with 10 potential wells, each potential well is approximately $65\mu K$ deep and for

2.6. Experimental realization of the ring-lattice potential with a weak link

the dark lattice with the same number of wells we get $15\mu K$. For the red-detuned lattice, cold atoms are trapped in the high intensity regions and they scatter 1 photons per 2 s and for the blue-detuned lattice atoms are trapped in the low intensity regions and they scatter 1 photon every 6 s. The potentials can be rotated with frequencies ranging from mHz to 10's of MHz.

However, this scheme has a drawback, that an additional trapping potential should be applied in z-direction in order to confine atoms.

2.6 Experimental realization of the ring-lattice potential with a weak link

The ring lattice optical potential is created with a liquid crystal on a silicon spatial light modulator (PLUTO phase only SLM, Holoeye Photonics AG) which imprints a controlled phase onto a collimated laser beam from a 532 nm wavelength diode pumped solid state (DPSS) laser. The SLM acts as a programmable phase array and modifies locally the phase of an incoming beam. Diffracted light from the computer generated phase hologram then forms the desired intensity pattern in the focal plane of an optical system (doublet lens, $f=150$ mm). The resulting intensity distribution is related to the phase distribution of the beam exiting the SLM by Fourier transform. Calculation of the required SLM phase pattern (kinoform) has been carried out using an improved version of the Mixed-Region-Amplitude-Freedom (MRAF) algorithm[69, 70] with angular spectrum propagator. This allows to simulate numerically the wavefront propagation in the optical system without resorting to the paraxial approximation. A region outside the desired ring lattice pattern (noise region) is dedicated to collect unwanted

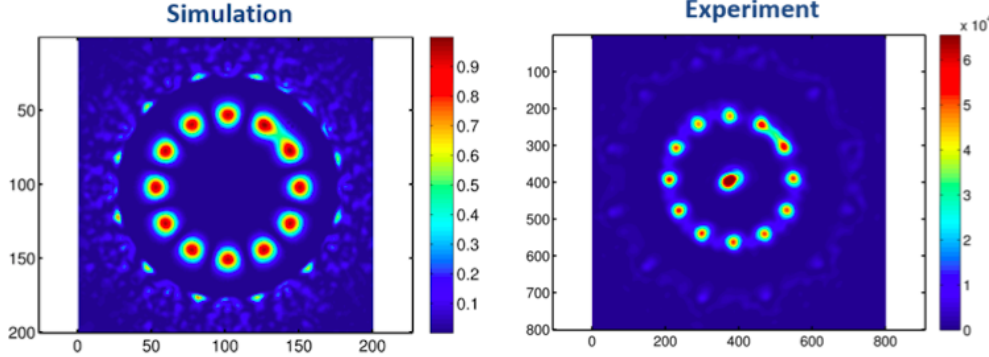


Figure 2.11: Simulation(left) and experimentally realized(right) intensity distribution of a ring- lattice with a weak link between two lattice sites.

light contributions resulting from the MRAF algorithm's iterative optimization process. This can be seen in the measured intensity pattern in Fig. 2.11 as concentric, periodic structures surrounding the ring-lattice and can be filtered out by an aperture.

The intensity generated by SLM shown on Fig. 2.11 has been chosen to be of the following form:

$$I(r, \phi) = I_0 e^{-\frac{(r-R)^2}{2\sigma^2}} \cos(0.5N\phi)^2 + 0.5I_0 e^{-\frac{(r \cos \phi - 5/7R)^2}{2\sigma^2}} e^{-\frac{(r \sin \phi + 5/7R)^2}{2\sigma^2}} \quad (2.12)$$

where in the radial direction the ring has a Gaussian tight confinement with amplitude I_0 and a half width at the maximum $\sigma \approx 9.5\mu m$ and in azimuthal direction the intensity profile is a sinusoidal lattice which has $N = 12$ lattice sites. Here in the Eq.(2.12) σ is chosen in the following way $\sigma = 1.3R/N$, where R is the average radius of the ring. The second line of Eq.(2.12) is introducing the weak link, which is added as a Gaussian dimple with amplitude $0.5I_0$ between 2 lattice sites. The effect of the dimple is clearly seen on the Fig.2.12 panel b), where an azimuthal intensity distribution is demonstrated.

2.7. Setup for adjustable ring-ring coupling

The ring-lattice potential shown in Fig. 2.11 and Fig. 2.12 can be readily scaled down from a radius of $\sim 90 \mu\text{m}$ to $5 - 10 \mu\text{m}$ by using a 50x microscope objective with NA=0.42 numerical aperture (Mitutoyo 50x NIR M-Plan APO) as the focusing optics for the SLM beam and with $\lambda_2 = 830 \text{ nm}$ light, suitable for trapping Rubidium atoms.

For experimental reasons, it is easier to confine atoms in attractive potentials (red-detuned optical potentials, where atoms are located in the maximum intensity regions) and it is planned to use a 840 nm laser for this purpose which is far detuned from the ^{87}Rb atom D1,D2 transitions. The drawback of red-detuned optical potentials is a higher spontaneous heating rate, so the laser has to be far detuned off-resonance. Accounting for the limited reflectivity and diffraction efficiency of the SLM, scattering into the noise region and losses in the optical system, only about 5% of the laser light contributes to the optical trapping potential. However this is not a limiting factor for small ring-lattice sizes in the tenth of micrometer range as discussed here, where $\sim 50 \text{ mW}$ laser power is sufficient to produce well depths of several E_{rec} . The generated structures are sufficiently smooth, with a measured intensity variation of 4.5% rms, to sustain persistent flow-states[18]. The barrier height can be dynamically modified at a rate up to 50 ms per step, with an upper limit imposed by the frame update rate of the SLM LCD panel (60 Hz).

2.7 Setup for adjustable ring-ring coupling

In this section two different proposals for experimental realization of ring lattices/AQUIDs with tunable distance between the rings/AQUIDs are suggested. First proposal based on the interference of Laguerre-Gauss beams [67, 35] and the second one makes us of the SLM technic [68, 69, 70].

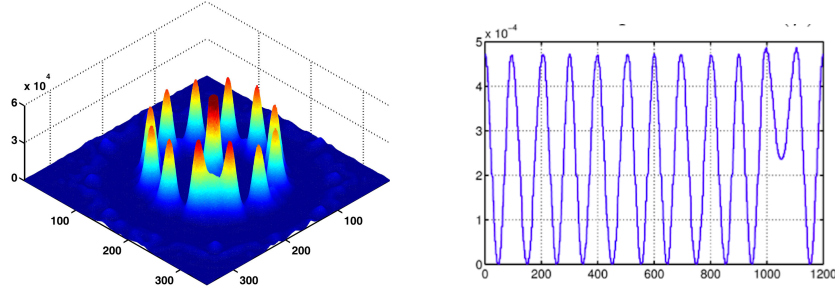


Figure 2.12: Experimental realization of a ring-lattice potential with an adjustable weak link. a) Measured intensity distribution with an azimuthal lattice spacing of $28 \mu\text{m}$ and a ring radius of $88 \mu\text{m}$. The central peak is the residual zero-order diffraction. The size of the structure is scalable and a lower limit is imposed by the diffraction limit of the focusing optics. b) Azimuthal intensity distribution for the fixed value of $r = R$.

2.7.1 Realization with Laguerre-Gauss beams

In this subsection, we describe the experimental setup for realizing two ring-shaped optical lattices with a tunable interaction between the atoms which are trapped in the rings. To achieve the task, we use Laguerre-Gauss (LG) modes to produce closed optical lattices[77, 78]. Fig.2.13 in the main text illustrates the experimental arrangement to produce two adjustable 1d ring-lattices by intersecting two Gaussian beams (G_1, G_2) with wavelength λ_1 . The ring-ring separation is controllable by changing the beam spacing D between beams G_1 and G_2 , allowing adjustment of the ring-ring tunnelling.

The inset in Fig.2.13 shows two vertically spaced ring lattice potentials separated by $d = \lambda_1 f / D$ [63]. In an experimentally feasible arrangement using light from a Ti:Sa laser at $\lambda_1 \approx 830 \text{ nm}$, with a beam separation adjustable between $D = 10 - 40 \text{ mm}$ and a lens focal length $f = 75 \text{ mm}$, the ring-ring separation can be varied from $d = 1.5 - 6.2 \mu\text{m}$. This compares to the inter-ring well spacing of $1.5 \mu\text{m}$ for a ring lattice with 20 lattice sites and ring radius of $5 \mu\text{m}$. To allow controlled tunnelling between neighboring lat-

2.7. Setup for adjustable ring-ring coupling

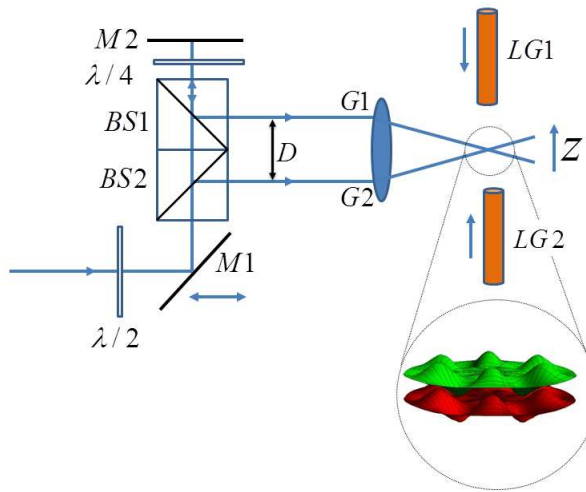


Figure 2.13: Proposed setup for the ring-ring coupling. Two gaussian laser beams of wavelength λ and with a distance D in between, pass through a lens and interfere in the focal plane (f is the focal length). The distance D can be easily controlled by moving one of the mirrors. The distance between the fringes is a function of $1/D$ [63]. The resulting Gaussian laser beam with wave vector $k_G = 2\pi D/(\lambda f)$, then, interferes with two counter propagating Laguerre-Gauss laser beams of amplitude E_0 . The inset shows the ring lattice potentials separated by $d = \lambda f/D$. Here $l = 6$ and $p = 0$.

tice stacks the distance between the ring potentials needs to be adjustable in the optical wavelength regime. Small distances allow high tunnelling rates, a necessity for fast gate operations. This makes it less efficient to read out and address individual stack sites, however. Increasing the lattice stack separation after the tunnelling interaction has occurred well above the diffraction limit ($\sim\lambda$) while keeping the atoms confined, optical detection and addressing of individual rings becomes possible. Fig.2.13 in the main text illustrates the experimental arrangement to produce two adjustable 1d ring-lattices by intersecting two Gaussian beams (G1,G2) with wavelength λ_1 .

The ring lattice potential shown in the inset in Fig. 2.13 can be written as

$$V_{latt} = 4E_0^2(f_{pl}^2 \cos(k_{LG}z)^2 + \cos(k_G z)^2 + 2f_{pl} \cos(k_{LG}z) \cos(k_G z) \cos(\phi l)), \quad (2.13)$$

where k_{LG} is the wave-vector of the Laguerre-Gauss beam. $k_G = \frac{2\pi D}{\lambda f}$ is an effective wave vector for the Gaussian beams, where D , λ and f are respectively the distance between the two beams passing through the lens, the wavelength of the Gaussian beams and the focal length of the lens. Using this equation, we conclude that a stack of closed rings is initially obtained, with $N = l$ lattice sites. The distance between rings can be controlled by changing the distance between the two Gaussian beams. This can be realized by moving the mirror $M1$. It can be shown that when $k_G = k_{LG}$, Eq.((2.13)) gives the potential obtained in [35]. So, this potential can be regarded as a generalization of previously obtained potential for the ring-shaped optical lattices.

The tunneling matrix element between two rings in the limit $V_0 \gg E_r$,

2.7. Setup for adjustable ring-ring coupling

where $V_0 = 4E_0^2$ and $E_r = \frac{\hbar^2 k^2}{2m}$ is the recoil energy, is given by

$$g = 4\sqrt{\frac{\hbar}{\sqrt{2m}}}\frac{V_0^{3/4}}{\sqrt{d}}e^{-\frac{\sqrt{2mV_0}}{\pi\hbar}d} \quad (2.14)$$

here $d = \lambda f/D$ is the lattice spacing along z-direction.

2.7.2 Realization with SLM

With a SLM arbitrary optical potentials can be produced in a controlled way only in a $2d$ -plane – the focal plane of the Fourier transform lens – making it challenging to extend and up-scale this scheme to 3d trap arrangements. The experiment, however, showed (see Fig.2.14) that axially the ring structure potential remains almost undisturbed by a translation along the beam propagation axis of $\Delta z = \pm 2.2 \cdot R$, where R denotes the ring-lattice radius. The ring-lattice radius is only weakly affected by an axial shift along z and scales with $\Delta R/R = 0.0097 \cdot z$, where z is normalized to the ring-lattice radius. For larger axial shifts from the focal plane the quality of the optical potential diminishes gradually. Based on our measurements this would allow implementation of ring-lattice stacks with more than 10 rings in a vertical arrangement, assuming a stack separation comparable to the spacing between two adjacent lattice sites. Propagation invariant beams may allow a potentially large number of rings to be vertically arranged[79].

The SLM method also can be extended to produce stack of ring-lattices/AQUIDs by combining it with a method introduced in a previous section. To achieve a goal it is enough to shine a cylinder shown on Fig.2.14 with two Gaussian beams in a transverse direction as it is shown on Fig.2.15. To allow controlled tunnelling between neighbouring

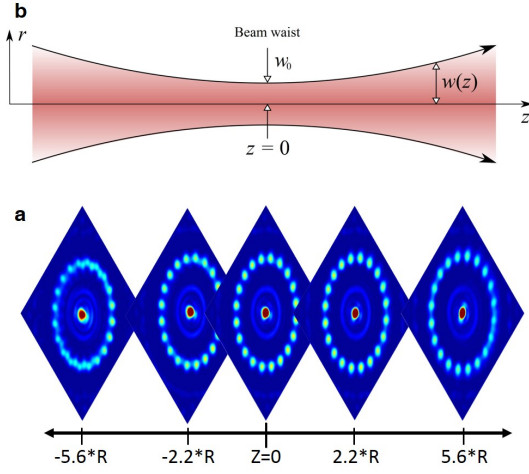


Figure 2.14: Effect of an axial translation on the ring lattice potential. a) Ring lattice intensity distribution measured at various positions along the beam propagation axis around the focal plane ($Z=0$). Note that the initial beam, phase modified by the SLM, is not Gaussian any more. The optical potential remains undisturbed by a translation of 2.2 times the ring-lattice radius centered around the focal plane ($Z=0$). b) This is in contrast to a Gaussian laser beam which exhibits a marked dependence on the axial shift from the focal plane where the beam waist $\omega(z)$ scales with $\sqrt{1 + (z/z_0)^2}$ and Rayleigh range z_0 .

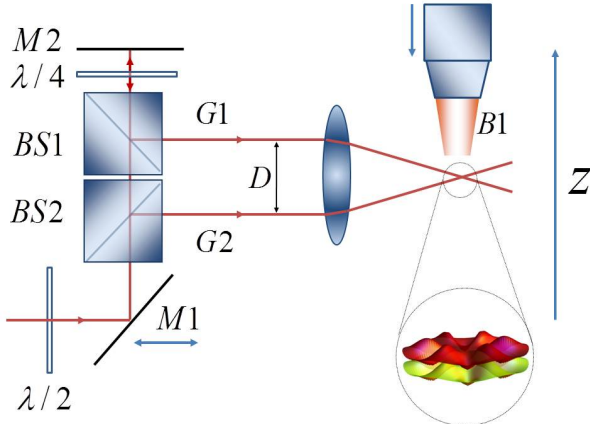


Figure 2.15: Experimental scheme for generating the stack of ring lattices/AQUIDs with tunable distance between the rings/AQUIDs. $B1$ shows the region where the cylinder of rings is formed.

2.7. Setup for adjustable ring-ring coupling

ring lattices/AQUIDs along the stack, the distance between the ring potentials/AQUIDs needs to be adjustable in the optical wavelength regime. A trade-off between high tunnelling rates (a necessity for fast gate operations) and an efficient read out and addressability of individual stack sites, needs to be analysed. Increasing the lattice stack separation after the tunnelling interaction has occurred well above the diffraction limit while keeping the atoms confined, optical detection and addressing of individual rings becomes possible.

2.7.3 Summary

In this chapter we summarized theoretical proposals and experimental advances in the field of cold atoms trapped in toroidal and ring lattice potentials [16, 17, 18, 14, 19, 36, 35, 54]. In particular, we focused on the techniques for generating, manipulating and measuring the current states in these systems. We then discussed, in more detail, on our proposed experimental setups and on some experimental results towards realization of the following ring lattice systems:

(*i*) Single ring lattice with an impurity, (*ii*) Stack of homogeneous ring lattices with tunable distance, which are distributed along the cylinder, and (*iii*) Stack of AQUIDs (all the weak links are distributed along the same axis), which are distributed along the cylinder. These systems have been realized by making use of a cylindrical symmetry of Laguerre-Gaussian beams and SLM devices, which imprints a desired phase onto incoming laser beam.

We note that it is not only important to make ring condensates to interact but also make the interaction tunable. This is an important feature for driving and controlling qubit-qubit interactions. To achieve the goal,

we first generated a light field which has a cylindrical shape and the desired intensity distribution along the azimuthal direction. We then illuminated the system in a transverse direction with two Gaussian beams which are intersecting at angle α , resulting in a stack of rings with a tunable distance $d = \lambda/2 \sin(\alpha/2)$ between the rings [52, 63], where λ is the wavelength of the beams. In order to make d tunable, it is sufficient to change the angle α which can be implemented by rotating or displacing one of the mirrors of the experimental setup.

By carefully analyzing our proposed experimental configuration, we conclude that it is feasible to arrange $n \sim 10$ ring-qubits in stacks configuration (as sketched on Fig.2.14) along the beam propagation axis.

CHAPTER 3

Models for many-body bosonic systems confined in ring shaped optical potentials

3.1 Introduction

In this chapter we introduce the many-body bosonic models relevant to our systems: the homogeneous ring interrupted by a delta-barrier and a ring optical lattice with a weak link; both structures are subjected to an artificial gauge field. We assume that the system dynamics is one dimensional. In the second part of the chapter we discuss how the models can be employed to study the emergence of quantum superposition states in ring-shaped potentials.

The chapter is outlined as follows. In Section 3.2 we introduce Bose-Hubbard model and discuss qualitatively the Mott-superfluid transition. We also formulate the model for a ring lattice with a weak link(subsection 3.2.1), and for two coupled ring lattices(subsection 3.2.2). In Section 3.3 we present Lieb-Liniger model for a homogeneous ring with a delta-barrier. In Section 3.4 we introduce Luttinger liquid formulation(which works well in the limit from intermediate to strong interactions) for the homogeneous ring with a delta-barrier. In Section 3.5 we discuss,

a simple mean-field approach for the AQUID, which is given by Gross-Pitaveskii equation, and describes well the bosonic dilute systems in the limit of weak interactions. In Section 3.6 we review the theoretical analysis of possible formation of the macroscopic superposition states in ring condensates [57, 58, 59]. Finally, we summarize our results in Section 3.7.

We give more details about these models in Appendix A.

3.2 Bose-Hubbard model

Since at the low temperatures the energies of particles are quite low, then we can assume that interactions are well described the the s-wave scattering a_s , and that the atomic potential $U(\mathbf{x})$ can be replaced by a two-body contact-interaction :

$$U(\mathbf{x}) = \frac{4\pi\hbar^2 a_s}{m} \delta(\mathbf{x}) = g\delta(\mathbf{x}) \quad (3.1)$$

Our starting point is the second-quantised Hamiltonian in terms of bosonic field operators $\hat{\Psi}(\mathbf{x})$:

$$\begin{aligned} \hat{H} &= \int d\mathbf{x} \hat{\Psi}^\dagger(\mathbf{x}) \left(-\frac{\hbar^2}{2m} \nabla^2 + V_0(\mathbf{x}) + V_T(\mathbf{x}) \right) \hat{\Psi}(\mathbf{x}) \\ &+ \frac{g}{2} \int d\mathbf{x} \hat{\Psi}^\dagger(\mathbf{x}) \hat{\Psi}^\dagger(\mathbf{x}) \hat{\Psi}(\mathbf{x}) \hat{\Psi}(\mathbf{x}) \end{aligned} \quad (3.2)$$

where $V_0(\mathbf{x})$ is the optical lattice potential, which normally takes form $V_0(\mathbf{x}) = V_0 \sin^2(kx)$, with wavevector $k = 2\pi/\lambda$, where λ is the wavelength of the laser and $V_T(\mathbf{x})$ describes an external magnetic trapping potential , which is usually slowly-varying on the scale of the lattice spacing.

3.2. Bose-Hubbard model

The energy eigenstates of single atoms are given by Bloch wave functions, and the superposition of Bloch states forms the set of orthogonal wave functions, which are called Wannier functions. These functions are well localized on the individual lattice sites(this condition is of course satisfied for relatively deep lattices). Here it is crucial that we assume that energies involved in the system are small compared to the excitation energy to the second Bloch band. Under this assumption, we expand the field operators in the Wannier basis and keeping only lowest vibrational states $\hat{\Psi}(\mathbf{x}) = \sum_i a_i w(\mathbf{x} - \mathbf{x}_i)$, where $w(\mathbf{x} - \mathbf{x}_i)$ are the single particle Wannier functions(which can be determined from a one-dimensional bandstructure calculation) localized around lattice site \mathbf{x}_i . After substituting this expansion in Eq. (3.3) we arrive at the BH model:

$$H_{BH} = -J \sum_i (a_i^\dagger a_{i+1} + h.c.) + \frac{U}{2} \sum_i n_i(n_i - 1) + \sum_i \varepsilon_i n_i \quad (3.3)$$

here the annihilation and creation operators obey the bosonic commutation relations $[a_i^\dagger, a_j] = \delta_{ij}$ and operators $n_i = a_i^\dagger a_i$ give the total number of bosonic atoms at the i-th lattice site. The parameter $J = \int d\mathbf{x} w(\mathbf{x} - \mathbf{x}_i)(-\frac{\hbar^2}{2m}\nabla^2 + V_0)w(\mathbf{x} - \mathbf{x}_i^{a,b})$ is the tunneling rate within neighboring lattice sites, and $\varepsilon_i \approx V_T(\mathbf{x})$. The parameter U takes into account the finite scattering length for the atomic two-body collisions on the same site and it is given by $U = \frac{4\pi a_s \hbar^2}{m} \int d\mathbf{x} |w(\mathbf{x})|^4$ [80].

Here we outline the assumptions which were used for derivation of BH Hamiltonian.

1. The tunneling matrix elements between neighboring sites, are much larger than those between next nearest neighboring sites.
2. The nearest-neighbor interaction energies are much smaller then on-site

interaction energies.

3. The interaction energies $\frac{U}{2} \sum_i n_i(n_i - 1)$ and thermal energies are much smaller than the separation to the first excited Bloch band.

The separation to the first excited Bloch band can be obtained in the harmonic approximation, which is based on the expansion of the potential close to the minima ($\sin^2(x) \approx x^2$). After making this expansion, we obtain the harmonic oscillator with the frequency $\nu = \sqrt{4E_R V_0}/\hbar$, where the recoil energy E_R is given by $E_R = \hbar^2 k^2 / 2m$. This gives an estimate of $\hbar\nu$ for the separation to the first Bloch band. Normally first two conditions are satisfied provided that the lattice is deeper than $2E_R$.

In order to understand the different phases of BH model it is useful to consider two limiting cases: the limit of vanishing interactions, where the system is in the superfluid phase, and the opposite limit where system can be in the Mott phase.

The superfluid limit can be realized in shallow optical lattices where the kinetic energy dominates over the two particle contact interaction. By hopping from one lattice site to other lattice site the atom loses the kinetic energy J , and therefore in order to minimize its energy single particle wave function spreads over all lattice sites. The ground state wave function in the case $U = 0$, is given by the following expression:

$$|\Psi_{SF}\rangle = \frac{1}{\sqrt{N!}} \left(\frac{1}{\sqrt{M}} \sum_{l=1}^M a_l^\dagger \right)^N |0\rangle \quad (3.4)$$

where N is the number of particles and M is the number of lattice sites. This state is clearly corresponding to each particle occupying lowest Bloch state with momentum $q = 0$. We comment that this kind of states are well described with Gross-Pitaevskii equation [30], where interactions are taken into account through simple mean-field approximation. One of the

3.2. Bose-Hubbard model

properties of this state is that it shows large off diagonal coherence, which can be seen by calculating one-body density matrix $\rho_{ij} = \langle a_i^\dagger a_j \rangle = N/M$. It is also interesting to point out that particle number fluctuations are also big in this state $(\Delta n_l)^2 = N/M$. The energy difference between the first excited state and the ground state scales like $\propto J/M^2$ and goes to 0 in the thermodynamic limit ($N \rightarrow \infty$, $M \rightarrow \infty$ and $M/N = const$). So in the thermodynamic limit superfluid phase has a vanishing gap. It is instructive to notice that in thermodynamic limit, Eq.(3.4) can be represented as the product of coherent states and takes the form:

$$|\Psi_{SF}\rangle = \prod_{i=1}^M \exp \left[\sqrt{\frac{N}{M}} a_i^\dagger \right] |0\rangle_i \quad (3.5)$$

Therefor the distribution for the number of atoms per lattice site will be Poissonian. By increasing the depth of the optical lattice two things happen: the hopping term goes down because the barrier height increases and the size of each lattice site decreases which facilitates stronger interactions between the atoms confined in the same lattice well. In this limit we can neglect the kinetic energy. Now let us consider systems with commensurate fillings which means $\bar{n} = N/M$ is an integer number. It is obvious that for the case filling 1 ground state energy will be minimized (and it is zero in this case) by putting one atom per lattice site. Similarly to this case, the ground state for any filling is given by:

$$|\Psi_{MI}\rangle = \prod_{i=1}^M |\bar{n}\rangle \quad (3.6)$$

so in this state each lattice site is occupied by \bar{n} atoms. This state has no long range off diagonal coherence $\rho_{ij} = 0$, for $i \neq j$, and the particle number fluctuations are also vanishing $(\Delta n_l)^2 = 0$. The lowest lying excitation is

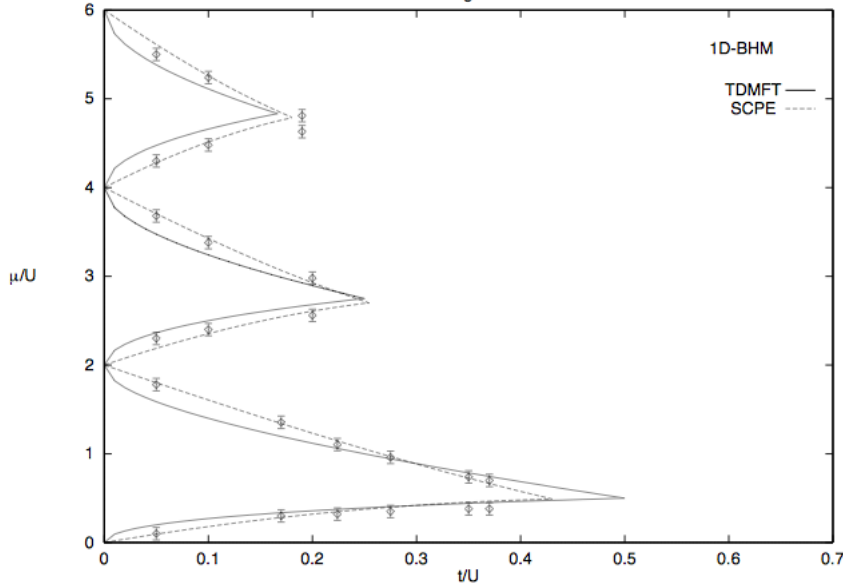


Figure 3.1: Phase diagram for the 1 dimensional BH model. The error boxes are the QMC results , the dashed lines are the result of the SCPE and the solid lines are TDMFT results. Taken from Ref.[81].

obtained by taking one atom from the lattice site and putting it on the top of atom sitting on other lattice site. The energy required for this is given by U and it does not depend on the system size. So we conclude that opposite to the superfluid phase, the Mott phase always has a finite gap given by the interaction strength.

The zero temperature phase diagram of the BH model is shown on Fig. 3.1, where the y-axis is given by μ/U and the x-axis by J/U . Here μ is the chemical potential and it controls the number of atoms per lattice site. It is seen that the phase diagram has a lobe-like structure. As was mentioned before, in the limit $J/U \rightarrow \infty$ the system is in the superfluid state and the ground state is described by Eq. (3.5) in the lowest order. In the opposite limit, series of Mott insulating phases are obtained with fixed filling $\bar{n} = 1, 2, \dots$. The defining property of the Mott phase is its incompressibility , which means $\partial n / \partial \mu = 0$. For an intermediate value of the fraction J/U it is not trivial to find out which phase the system is in and more detailed

3.2. Bose-Hubbard model

analysis is required. Several analytical and numerical approaches have been developed to study that problem. On Fig.3.1 we demonstrate the Mott-superfluid phase diagram for the 1D BH model which is obtained by the following methods: Quantum Monte-Carlo simulations(QMC) [82], strong coupling perturbative expansion(SCPE) [83], and time-dependent dynamical mean-field theory(TDMFT) [81]. The TDMFT(which is a mean-field analytical approach) is a simple approach for obtaining the phase diagram and at the same time it agrees quite well with SCPE and QMC results, which are considered as most precise approaches for obtaining the phase diagram of the 1 dimensional BH model.

3.2.1 Bose-Hubbard model for a single ring with a weak link

We consider a system of interacting bosons at zero temperature, loaded into a 1D ring-shaped optical lattice of N sites. The discrete rotational symmetry of the lattice ring is broken by the presence of a localized potential on one lattice site (located at the site $N - 1$), which gives rise to a weak link. The ring is pierced by an artificial (dimensionless) magnetic flux Φ , which can be experimentally induced for neutral atoms as a Coriolis flux by rotating the lattice at constant velocity [41, 14], or as a synthetic gauge flux by imparting a geometric phase directly to the atoms via suitably designed laser fields [48, 84, 47].

In the tight binding approximation [80], the system is described by the Bose-Hubbard Hamiltonian:

$$H_{BH} = \frac{U}{2} \sum_{i=0}^{N-1} n_i(n_i - 1) - \sum_{i=0}^{N-1} t_i(e^{i\Phi/N} a_i^\dagger a_{i+1} + h.c.) \quad (3.7)$$

Chapter 3. Models for many-body bosonic systems confined in ring shaped optical potentials

where a_j (a_j^\dagger) are bosonic annihilation (creation) operators on the j -th site and $n_j = a_j^\dagger a_j$ is the corresponding number operator. The parameters t_i describe the tunnelling between the wells along the ring. Since the wells are all identical but one, $t_i = t, \forall i = 0 \dots N-2$ and $t_{N-1} = t'$.

The presence of the flux is taken into account through the Peierls substitution(see appendixB.1): $t \rightarrow e^{-i\Phi/N}$ (t is the hopping amplitude). The "magnetic flux" is given by $\Phi = \int_{x_i}^{x_{i+1}} \mathbf{A}(\mathbf{z}) d\mathbf{z}$, where $\mathbf{A}(\mathbf{z})$ is the a synthetic vector potential. The effect of the dimple is to induce a phase slip at the site $N-1$. Periodic boundaries are imposed by taking $a_N \equiv a_0$.

The presence of the barrier can be also taken into account through a site-dependent chemical potential. In that case the 1D Bose-Hubbard Hamiltonian takes the form:

$$H = \sum_{j=1}^M \left[-t(e^{-i\Omega/M} b_j^\dagger b_{j+1} + \text{h.c.}) + \frac{U}{2} n_j(n_j - 1) + \Lambda_j n_j \right], \quad (3.8)$$

where b_j (b_j^\dagger) are bosonic annihilation (creation) operators on the j th site and $n_j = b_j^\dagger b_j$ is the corresponding number operator. Periodic boundaries are imposed by taking $b_{M+1} \equiv b_1$. The potential barrier considered here is localized on a single site j_0 , i.e., $\Lambda_j = \Lambda \delta_{j,j_0}$ with $\delta_{i,j}$ being the Kronecker delta.

3.2.2 The model for two coupled rings

A single-species bosonic condensate is envisaged to be loaded in the setup described on Fig.2.13. Our system is thus governed by a Bose-Hubbard ladder Hamiltonian:

$$H_{BH} = H_a + H_b + H_{int} - \sum_{\alpha=a,b} \sum_{i=0}^{N-1} \mu_\alpha \hat{n}_i^\alpha \quad (3.9)$$

3.2. Bose-Hubbard model

with

$$\begin{aligned}
 H_a &= -t \sum_{i=0}^{N-1} (e^{i\Phi_a/N} a_i^\dagger a_{i+1} + h.c.) + \frac{U}{2} \sum_{i=1}^N \hat{n}_i^a (\hat{n}_i^a - 1) \\
 H_b &= -t \sum_{i=0}^{N-1} (e^{i\Phi_b/N} b_i^\dagger b_{i+1} + h.c.) + \frac{U}{2} \sum_{i=1}^N \hat{n}_i^b (\hat{n}_i^b - 1) \\
 H_{int} &= -g \sum_{i=0}^{N-1} (a_i^\dagger b_i + b_i^\dagger a_i)
 \end{aligned} \tag{3.10}$$

where $H_{a,b}$ are the Hamiltonians of the condensates in the rings a and b and the H_{int} describes the interaction between rings. Operators $\hat{n}_i^a = a_i^\dagger a_i$, $\hat{n}_i^b = b_i^\dagger b_i$ are the particle number operators for the lattice site i . Operators a_i and b_i obey to the standard bosonic commutation relations. The parameter $t = \int w^{a,b}(\mathbf{x} - \mathbf{x}_i^{a,b}) (-\frac{\hbar^2}{2m} \nabla^2 + V_{latt}) w^{a,b}(\mathbf{x} - \mathbf{x}_i^{a,b})$ is the tunneling rate within lattice neighboring sites(in the rings a and b), and $g = \int w^a(\mathbf{x} - \mathbf{x}_i^a) (-\frac{\hbar^2}{2m} \nabla^2 + V_{latt}) w^b(\mathbf{x} - \mathbf{x}_i^b) d^3\mathbf{x}$ is the tunneling rate between the rings, where $w^{a,b}(\mathbf{x})$ and are the single particle Wannier functions and site index for the rings a and b respectively and $w^{a,b}(\mathbf{x} - \mathbf{x}_i^{a,b}) = w(x - x_i)w(y - y_i)w(z - z_i \pm d/2)$ (where + sign holds for the ring a and - sign for the ring b), with d being distance between the rings. Here we assume that Wannier functions for the two rings are identical. Finally, the phases Φ_a and Φ_b are the phase twists responsible for the currents flowing along the rings. They can be expressed through vector potential of the so-called synthetic gauge fields in the following way: $\Phi_a/N = \int_{x_i}^{x_{i+1}} \mathbf{A}(z) dz$, $\Phi_b/N = \int_{x_i}^{x_{i+1}} \mathbf{B}(z) dz$, where $\mathbf{A}(z)$ and $\mathbf{B}(z)$ are generated vector potentials in the rings a and b , respectively (see appendixB.1).

3.3 Lieb-Liniger model for a homogeneous ring with a delta-barrier

We generalize the Lieb-Liniger model for the ring when due to the presence of a delta-barrier the system becomes nonintegrable. We consider a system of N bosons of mass m , subjected to contact interaction with an effective 1D interaction strength g (see Appendix A.1), accounting for s-wave scattering, and loaded into a 1D ring (the conditions under which a 2D system can be reduced to a 1D one are introduced in Appendix A.1) of length L , with density $n = N/L$. An important dimensionless parameter for the model is given by $\gamma = mgL/\hbar^2N$, where L is the length of the system. The position along the ring is parameterized by the angular coordinate $\theta \in [0, 2\pi)$. The ring contains a localized barrier potential, modeled as a delta function, and is threaded by an artificial (dimensionless) ‘magnetic flux’ Ω . The corresponding Hamiltonian reads:

$$H = \sum_{i=1}^N \frac{\hbar^2}{2m} \left(-i \frac{\partial}{\partial x_i} - \frac{2\pi\Omega}{L} \right)^2 + \Lambda\delta(x) + g \sum_{i < j}^N \delta(x_i - x_j) \quad (3.11)$$

where we adopted Λ is the strength of the barrier.

In this thesis, we will be interested only in the stationary regime, which can be achieved by adiabatically switching on the barrier at early times, to avoid the creation of higher excitations.

3.4. Luttinger model for a homogeneous ring with a delta-barrier

3.4 Luttinger model for a homogeneous ring with a delta-barrier

At low temperatures most 1D bosonic models have a liquid phase which has two main properties: 1) the low energy excitations are collective sound-like modes with linear dispersion. 2) Zero temperature correlations functions have algebraic decay. It turns out that these two properties are defining a universality class of 1d systems which can be characterized by the so-called Luttinger liquid theory, which is not a mean-field theory and can describe systems both in the intermediate and strong interaction limits. This universal approach was first time suggested by Haldane [85] and it is also called bosonisation. At strong interparticle interactions we characterize the system of bosonic particles with the Luttinger liquid Hamiltonian: To take into account the effect of quantum fluctuations in the intermediate- to strong-interaction regime we describe the system with a Luttinger Hamiltonian:

$$\begin{aligned} H = & \frac{\hbar v_s}{2\pi} \int_0^L dx \left[K \left(\nabla \phi(x) - \frac{2\pi\Omega}{L} \right)^2 + \frac{1}{K} (\nabla \theta(x))^2 \right] \\ & + \int_0^L dx \Lambda \delta(x) \rho(x), \end{aligned} \tag{3.12}$$

here θ and ϕ corresponding to the density fluctuation and the superfluid phase, the interaction strength is given by the Luttinger parameter K and the sound velocity v_s . More details about the Luttinger model and the dependence of the parameters K and v_s on the parameter γ are discussed in Appendix A.4. As the vanishing interactions K tends to infinity and v_s vanishes, while in the opposite limit, $K = 1$ and v_s is given by the Fermi velocity of the fermionized system.

3.5 Gross-Pitaevskii equation for the AQUID

In the limit of weak interactions the AQUID system is governed by a Gross-Pitaevskii (GP) equation:

$$\frac{\hbar^2}{2m} \left(-i\partial_x - \frac{2\pi\Omega}{L} \right)^2 \Psi + U_b \delta(x) \Psi + V_0 \sin^2 \left(\frac{M}{L} \pi x \right) \Psi + g_{1D} |\Psi|^2 \Psi = \mu \Psi \quad (3.13)$$

where Ψ is the condensate wavefunction, μ is the chemical potential, V_0 is the optical-lattice depth, U_b is the strength of the localized barrier, modeled as $\delta(x)$ in this continuous model. The continuous-model barrier strength U_b is connected to the discrete-model one Λ by $U_b = \Lambda L/M$. An expression for g_{1D} is given in Appendix A.1. We comment, that for the case $V_0 = 0$ Eq. (3.13) captures also the system given by homogeneous ring, pierced by "magnetic flux". In absence of the lattice potential, an analytical soliton solution for Eq. (3.13) has been found in [86]. In the further limiting case of vanishing interaction and small barrier strength, the expression for the wavefunction can be obtained perturbatively with respect to the barrier strength (see C.2). This approach helps the understanding of the corresponding momentum distribution and time-of-flight images. In the presence of the lattice potential, we solve Eq. (3.13) numerically by integrating it in imaginary times. We pursue this approach as a benchmark case for the BH model at weak interaction. Moreover the GP equation is a particularly suitable tool for the large- N regime, which is routinely realized in experiments. We introduce the derivation of the Gross-Pitaevskii equation and also discuss its applicability for 1D systems in Appendix A.5.

3.6. Theoretical analysis of macroscopic superposition states in the AQUID

3.6 Theoretical analysis of macroscopic superposition states in the AQUID

In this section we review the formation of superposition states in ring condensates [56, 57, 58, 59]. At first we focus on the system of homogeneous ring which hosts a delta-barrier and is subject to artificial gauge field. The Hamiltonian of this system is given by Eq. (3.11). By considering the non-interacting, weakly interacting and strongly interacting regimes of this system, different superposition states can be obtained as a ground state of the Hamiltonian. In order to gain a better understanding of the formation of superposition states, it is convenient to write down the Hamiltonian in the second quantized form(as it is done in the section 3.2) and write it in momentum space(by using $\Psi(x) = 1/\sqrt{L} \sum_k e^{2\pi kx/L} a_k$, where a_k^\dagger creates an atom with angular momentum $k\hbar$):

$$\begin{aligned}
 H &= H_K + H_B + H_I \\
 &= \sum_{k=-\infty}^{\infty} E_0 \left(k - \frac{\Omega}{\Omega_0} \right)^2 a_k^\dagger a_k + \frac{\Lambda}{L} \sum_{k_1, k_2=-\infty}^{\infty} a_{k_1}^\dagger a_{k_2} \\
 &\quad + \frac{g}{2L} \sum_{k_1, k_2, q=-\infty}^{\infty} a_{k_1}^\dagger a_{k_2}^\dagger a_{k_1-q} a_{k_2+q} \varepsilon
 \end{aligned} \tag{3.14}$$

Here we are interested in two kinds of states. The first one is a NOON state which is given by:

$$|\Psi\rangle = \frac{1}{\sqrt{2}} (|N, 0\rangle_{0,1} + |0, N\rangle_{0,1}), \tag{3.15}$$

where the index shows the number of atoms occupying the particular mode and the subindex specifies the mode. And the second state is a superposi-

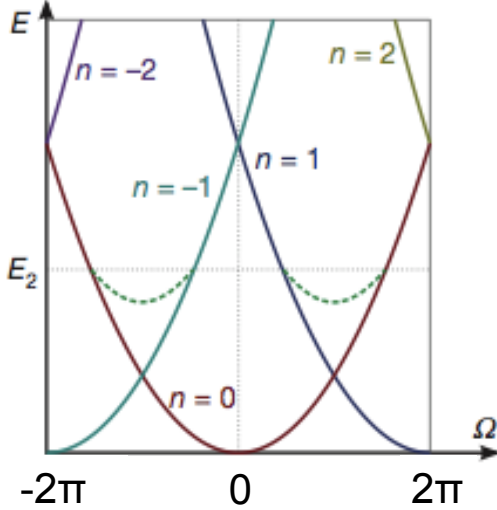


Figure 3.2: Single-particle energy level structure as a function of rotational phase Ω . It is clearly seen, that for the values $\Omega = (2j + 1)\pi$ spectrum is doubly-degenerate. Taken from [19].

tion state of total angular momentum states 0 and N, and it reads as:

$$|\Psi\rangle = \frac{1}{\sqrt{2}}(|0\rangle \pm |N\rangle) \quad (3.16)$$

First we consider the case when $g = 0$ and Λ is small. In this case, single-particle energies (which are proportional to the $(n - \Omega / 2\pi)^2$, where n is an angular momentum) are given by the families of intersecting parabolas as is demonstrated in Fig.3.2. At $\Omega = \pi$, the momentum states of 0 and \hbar are degenerate (this degeneracy is removed by a finite barrier) and the ground state at the degeneracy point($\Omega = \pi$) is given by:

$$|\Psi\rangle_G = \frac{1}{\sqrt{2^N N!}}(a_0 + a_1)^N|vac\rangle = \frac{1}{\sqrt{2^N}} \sum_{r=0}^N \sqrt{\frac{N!}{(N-r)!r!}}|N-r, r\rangle_{0,1} \quad (3.17)$$

All the states of the form $|N-r, r\rangle_{0,1}$ are degenerate ($N+1$ fold degeneracy), however this degeneracy is removed by the interaction term H_I of the Hamiltonian.

3.6. Theoretical analysis of macroscopic superposition states in the AQUID

Let us now consider the limit of small g and small Λ . In order to get a simple understanding of the lifting of the degeneracy, let us apply a simple first order perturbation theory. We write down the matrix element $_{0,1}\langle N - r, r | H_I | N - r, r \rangle_{0,1} = \frac{g}{2L}(N(N-1) + 2r(N-r))$. It is clearly seen, that only the states $|N, 0\rangle_{0,1}$ and $|0, N\rangle_{0,1}$ remain degenerate. The barrier term H_B couples these terms in the higher order of the perturbation theory. We comment that H_B is the only term in the Hamiltonian which couples terms with different total angular momentum. As it was shown in [57] the NOON states can be achieved only under satisfying the set of conditions $\Lambda\sqrt{N}/L \ll gN/2L \ll E_0$ and the energy gap(the difference between the first excited state and the ground state of the many-body Hamiltonian) is given by:

$$\Delta E = \frac{\Lambda^N}{g^{N-1}} \frac{2}{L} \frac{N}{(N-1)!} \quad (3.18)$$

from this expression we see that the energy gap decreases faster than exponentially with the number of particles. This makes creation of the NOON states with high particle numbers quite challenging experimentally.

Now we consider the limit of $g \rightarrow \infty$. As it is well known in this regime particles undergo so-called fermionization and start to behave like spinless fermions. In this limit the two mode representation in momentum space is not valid however it can be shown that ground state and first excited states are given by Eq. (3.16). The energy gap is given by:

$$\Delta E \approx \frac{\Lambda}{L} \quad (3.19)$$

we remark that this kind of dependence of the energy gap is favorable since it does not depend on the number of particles. In order to quantify the quality of superposition states with total angular momentum K_1 and K_2 , respectively, we introduce a quantity Q , which is given by:

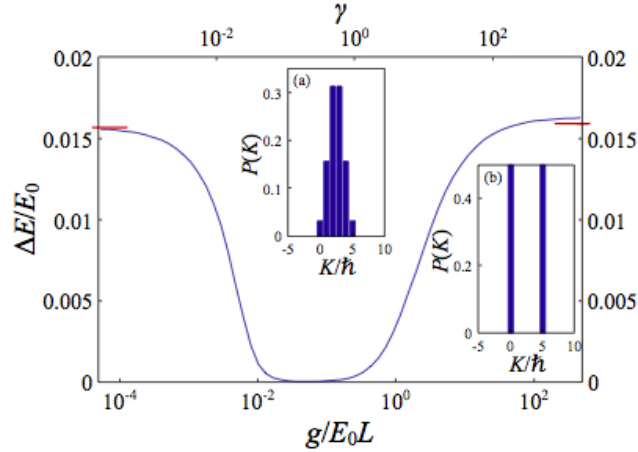


Figure 3.3: Energy gap ΔE as a function of the interaction strength obtained with exact diagonalization of the truncated momentum Hilbert space keeping $r = 20$ modes. Here $\Omega = \pi$, $N = 5$ and $\Lambda/L = 0.008E_0$. The upper horizontal axis shows Lieb-Liniger parameter $\gamma = 2g\pi^2/E_0LN$. The inset plots show total angular momentum distribution function $P(K)$ for non-interacting and strongly interacting systems. Taken from [57].

$$Q = 4P(K_1)P(K_2) \quad (3.20)$$

Q varies between 0 and 1. If $Q = 1$ it means that system is in the equal superposition of two angular momentum states. Insets of Fig.3.3 show total angular momentum distribution function in the non-interacting and strongly interacting limit. $P(K)$ is binomial and binary,respectively, for non-interacting and strongly interacting systems. It is clearly seen, that the Tonks-Girardeau limit is a good candidate for creating superposition states given by Eq. (3.16). It is more interesting to compare quality factors and robustness for NOON and total angular momentum superposition states. As it is seen from Fig3.4, around $g \approx 0.1E_0L$ a high quality NOON state is formed. But robustness of this state against single particle loss is very small as it is expected for a NOON state. However the same figure demonstrates that in the limit of strong interaction high quality su-

3.6. Theoretical analysis of macroscopic superposition states in the AQUID

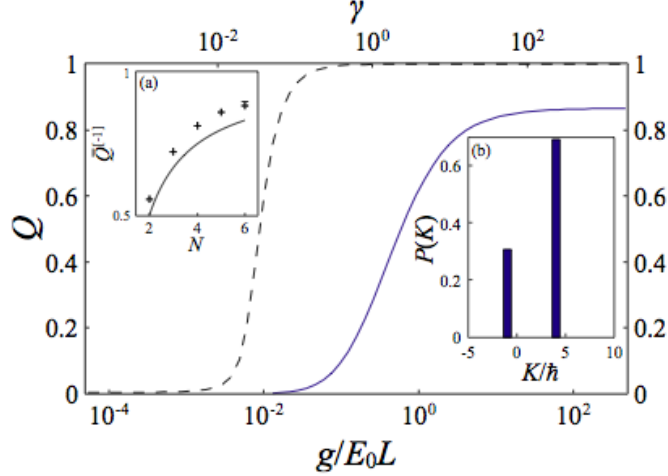


Figure 3.4: The quality of superposition before (Q -the dashed line) and after ($Q^{[-1]}$ -the solid line) removal of a single particle. Here parameters are the same as in Fig.3.3. a) $Q^{[-1]}$ in the Tonks-Girardeau limit as a function of the number of particles b) Total angular momentum distribution function after the removal of one particle with angular momentum \hbar . Taken from [57].

perposition states given by Eq. (3.16)are formed and they have very high robustness against single particle loss. The Hamiltonian given by Eq. (3.11) has been modeled with a one dimensional ring lattice [58] which has a localized impurity in one of the lattice sites. The Hamiltonian of this lattice model is given by Eq. (3.8). Since at low fillings the particles feel only the quadratic part of the dispersion, the results of the ring lattice system should coincide with the results of the one dimensional ring in the limit of low filling($N/L \ll 1$). Most interestingly in Ref. [58] it was demonstrated that even in the Tonks limit the energy gap gets exponentially suppressed once one considers Gaussian barriers with finite width. For a barrier with Gaussian potential($\Lambda_j \propto \Lambda e^{-d^2 j^2 / 2\xi^2}$) of half-width ξ the energy gap in the limit of weak barrier is given by:

$$\Delta = 2 \frac{\Lambda}{L} \exp \left[\frac{-2\pi^2 \xi^2 N^2}{d^2 M^2} \right] \quad (3.21)$$

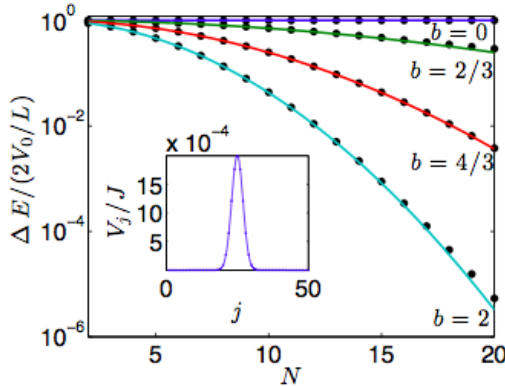


Figure 3.5: Supresion of the energy gap ΔE for the Gaussian barrier with finite width. Here $L = 50$ and $b = \xi/d$. Taken from [58].

Here Λ is the height of the barrier and M is number of lattice sites. As is seen from Fig.3.5, the energy gap is decreasing quite fast even for such a small number of particles as ≈ 20 . In agreement with [57] the energy gap is independent of the number of particles in the limit $\xi \rightarrow 0$ (See Fig.3.5). The physical reason for the exponential suppression of the gap is the following: in order to couple angular momentum states of the superposition given by Eq. (3.16) one needs to transfer large amount of momentum(the barrier term of Hamiltonian is the only term that couples states with different total angular momentum). However, if the barrier has a Gaussian profile then its Fourier image has a Gaussian distribution as well, which causes an exponential suppression for the coupling of different angular momentum states. This in turn recovers exponential suppression of the gap in the Tonks limit.

We comment that site dependent character of the barrier should be taken into account if the barrier spreads over several lattice sites. However if the barrier potential can be localized over one lattice spacing, then barrier can be considered as single site barrier and the energy has the favorable scaling(it scales as in the limit $\xi \rightarrow 0$). Moreover, as it has been demonstrated

3.6. Theoretical analysis of macroscopic superposition states in the AQUID

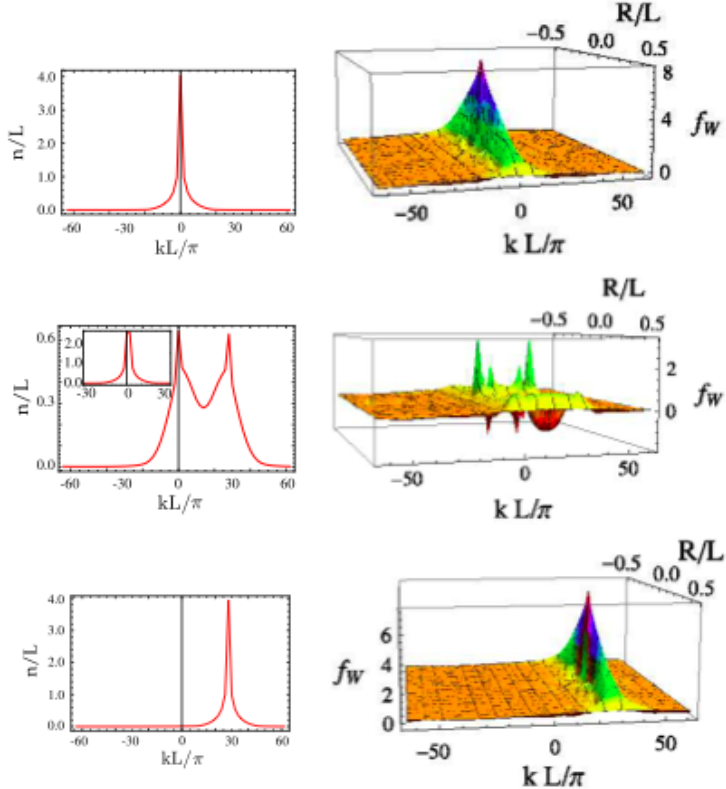


Figure 3.6: The momentum distribution and Wigner functions at $t/t_0 = 0, 2.46$ and 4.92 . Here $t_0 = mL^2/\pi\hbar$, $N = 9$ and $v = 14\hbar\pi/mL$. In the inset of the second figure $v = 14\hbar\pi/mL$. Taken from [59].

in Ref. [87], a square barrier with height $1/l$ and width l of the order of one tenth of the circumference does not fundamentally change the system's properties, i.e the particles' wave vectors are only slightly modified. For weak barriers, no difference between the two types of barriers was observed.

So far the generation of superposition states is based on the adiabatic change of the "external flux". In Ref.[59], a sudden quench with a delta type barrier is discussed for the Tonks gas confined in a one dimensional ring trap. It is shown that the out-of-equilibrium drive generates new type of superposition states which are superpositions of two Fermi spheres rather then superposition of microscopically occupied single momentum

states. The full analytical solution of the problem is obtained and important quantities like the momentum distribution $n(k, t)$ and Wigner function $f_W(x, k, t)$ are evaluated. These functions are defined with help of the one-body density matrix $\rho(x, y, t)$ in the following way:

$$n(k, t) = \int dx \int dy e^{ik(x-y)} \rho_1(x, y, t) \quad (3.22)$$

$$f_W(x, k, t) = \int dr e^{ikr} \rho_1(x + r/2, x - r/2, t) \quad (3.23)$$

Fig.3.6 demonstrates how these quantities change depending on the steering time. On the second figure it is easy to observe the formation of a superposition state of two Fermi spheres. We comment that negative values of the Wigner function for this case evidences the quantum nature of this kind of superposition state.

3.7 Summary

We introduced the 1D bosonic systems mainly for describing two different systems: ring lattice/homogeneous ring systems which are pierced by "magnetic flux" and host weak link/delta barrier.

The Bose-Hubbard(BH) model plays a central role for the current thesis since it captures well(under some additional assumptions) the dynamics of cold bosonic systems trapped in lattice potentials [80]. After introducing the BH model and qualitatively discussing superfluid-Mott transition, we also have introduced the system of two coupled rings which is governed by the two-leg ladder BH Hamiltonian, where each of the homogeneous ring lattices is pierced by a different "magnetic flux". To study the system of a homogeneous ring which hosts a delta-barrier impurity in the limit of intermediate to strong interactions, we exploited the Luttinger liquid

3.7. Summary

theory, a low-energy hydrodynamic formulation for the systems with linear dispersion relation. We introduced the Gross-Pitaevskii equation, which is a mean-field approach suitable for studying the limit of weak interactions and high fillings.

Finally, we also reviewed different theoretical proposals for generating many-body superposition states. We introduced theoretical results for the energy gap of the many-body Hamiltonian for the different kinds of superposition states. The quality of superposition states and their robustness regarding single-particle loss were reviewed as well.

CHAPTER 4

Realization of qubits with ring optical lattices

4.1 Introduction

A qubit is a two state quantum system that can be coherently manipulated, coupled to its neighbours, and measured. Several qubit physical implementations have been proposed in the last decade, all of them presenting specific virtues and bottlenecks at different levels[26, 2, 88, 89, 90, 91]. In neutral cold atoms proposals the qubit is encoded into well isolated internal atomic states. This allows long coherence times (up to minutes), precise state readout and, in principle, scalable quantum registers. However, individual qubit (atom) addressing is a delicate point[92, 93]. Qubits based on Josephson junctions allow fast gate operations (order of nanoseconds) and make use of the precision reached by lithography techniques[94]. The decoherence, however, is fast in these systems and it is experimentally challenging to reduce it (see for details Chapter1). Here we aim at combining the advantages of cold atom and Josephson junction based implementations. The basic idea is to use the persistent currents flowing through ring shaped optical lattices[35, 57, 95, 58, 60] to realize a cold atom analogue of the superconducting flux qubit. Our implementation combines the low decoherence rates of of neutral cold atoms systems, overcoming single

Chapter 4. Realization of qubits with ring optical lattices

site addressing, with the robustness of topologically protected solid state Josephson flux qubits. Characteristic fluctuations in the magnetic fields affecting Josephson junction based flux qubits are expected to be minimized employing neutral atoms as flux carriers.

It has been demonstrated theoretically that two opposite flowing currents in the AQUID can, indeed, define an effective two-level system, that is, the cold-atom analog of the rf-SQUID [96, 54]. The potential constriction breaks the Galilean invariance and splits the qubit levels that otherwise would be perfectly degenerate at half-flux quantum. In this context, it is of vital importance for the qubit dynamics that a good energy resolution of the two levels could be achieved in realistic physical situations (while keeping the qubit well separated from the rest of the many-body spectrum). In order to achieve this aim, we examine the dependence of the qubit energy gap on the bosonic density, the interaction strength, and the barrier depth.

In this chapter we focus on ring-shaped confinements with a *lattice modulation* and a *potential constriction*. This set-up, that can be realized following different routes (see, e.g., Ref. [54]), presents several added features for the design of an AQUID.

First of all, assuming that the bosons occupy only the lowest Bloch band¹, the ring lattice helps in controlling the current. For instance, because of the one-dimensional dynamics, the vortex formation rate along the flow is negligible. Secondly, it helps to localize the barrier effect to a point-like scale with respect to lattice spacing, which should in turn yield a favorable scaling of the qubit gap with the bosonic density [58]. Moreover, it provides an easy route to realize interacting ring-ring architectures [35,

¹ This condition is especially feasible nowadays, because the gap between the lowest Bloch bands can be magnified, by playing with the shape of the wells, a feature that is straightforward to implement realizing the ring lattice with SLM devices. The influence of the other Bloch bands has been analyzed in [97].

4.1. Introduction

[54]².

This issue has been considered so far only in some limiting cases, e.g. for particular types of superposition states or in the infinitely strong interacting regime [57, 58]. On the theoretical side, we perform a systematic study on the quality of the qubit in the cold-atom ring lattice: in particular, we characterize the energy structure at the degeneracy point at half-flux quantum, and study how it is possible to observe experimentally the superposition of the current flows. By employing a combination of analytical and numerical techniques that allows us to cover all the relevant physical regimes of system sizes, filling, barrier and interaction strengths, we show that: *i*) the gap ΔE_1 between the states of the effective two-level system scales as a power law with the system size; *ii*) at a mesoscopic scale, a qubit is well-defined, with ΔE_1 displaying a favorable dependence in a wide range of system parameters. Based on our analysis, we provide protocols to initialize and address the qubit. Read-out of the qubit can be done with help of TOF measurement and is discussed, in more detail, in Chapters 2 and 5.

This chapter is organized as follows. In Section 4.2 we present the physical system of interacting bosons on a 1D ring lattice with a potential constriction, and the effective two-level system giving rise to the AQUID. By combining different theoretical and numerical methods we show that effective two-level system appears both for high and low fillings. In Section 4.3 the energy spectrum of the system and its scaling with a system size, filling, and interaction is analyzed. We show that in the limit of the low filling and weak barrier strength Luttinger liquid results are in good

²Experimentally, the ring lattice are arranged along a laser confinement with cylindrical symmetry, with a ‘pancake’ structure. The inter-ring tunneling, however can be made negligible with different approaches (for example suitably focusing the laser beams). See also Ref. [55].

agreement with DMRG simulations. Finally, we draw our conclusions in Section 4.4.

It is worth noting that in Section 4.3 DMRG/MPS results have been obtained by Davide Rossini and Mateo Rizzi and some exact results in the limits of non-interacting and Tonks-Girardeau regimes have been derived by Marco Comminoti.

4.2 The physical system

We consider a system of N interacting bosons at zero temperature, loaded into a 1D ring-shaped optical lattice of M sites. The discrete rotational symmetry of the lattice ring is broken by the presence of a localized potential on one lattice site, which gives rise to a weak link. The ring is pierced by an artificial (dimensionless) magnetic flux Ω , which can be experimentally induced for neutral atoms as a Coriolis flux by rotating the lattice at constant velocity [41, 14], or as a synthetic gauge flux by imparting a geometric phase directly to the atoms via suitably designed laser fields [48, 84, 47].

The Hamiltonian of the ring lattice with a weak link (which is introduced in Section 3.2.1) under a study is given by Eq. (3.8). In the thermodynamic limit, the BH model for $\Lambda_j = 0 \forall j$ displays a superfluid to Mott-insulator transition for commensurate fillings N/M , and at a critical value of the ratio U/t of interaction-to-tunnel energy. The phase boundaries of the transition are expected to be affected by the magnetic flux through an overall rescaling $t/U \rightarrow (t/U) \cos(\Omega/M)$ [98]. The potential barrier considered here is localized on a single site j_0 , i.e., $\Lambda_j = \Lambda \delta_{j,j_0}$ with $\delta_{i,j}$ being the Kronecker delta. As we will discuss in Section 4.3.2, we find

4.2. The physical system

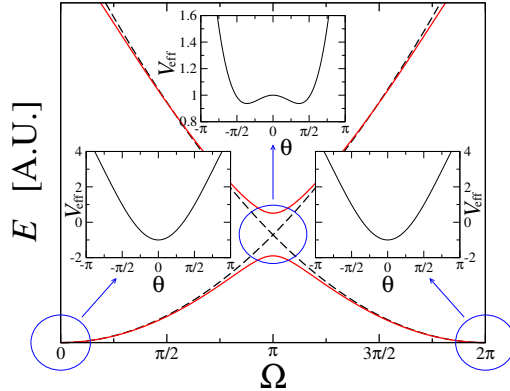


Figure 4.1: Main panel: sketch of the qubit energy splitting, due to the barrier Λ , for the two lowest-lying energy states in the many-body spectrum of model (3.8). Black dashed lines denote the ground-state energy in the absence of the barrier, as a function of the flux Ω . Switching on the barrier opens a gap at the frustration point $\Omega = \pi$ (continuous red lines). The three insets show the qualitative form of the effective potential at $\Omega = 0, \pi, 2\pi$. Note the characteristic double-well shape forming at $\Omega = \pi$. The qubit, or effective two-level system, corresponds to the two lowest energy levels of this potential. In this figure the energies are plotted in arbitrary units.

a superfluid-insulator transition even if the ring is interrupted by a weak link, although the phenomenon is here a crossover, the ring being of finite size.

In this work, specific regimes of the system described by Eq. (3.8) will be captured analytically via the Tonks-Girardeau (TG) mapping (hard-core limit of infinite repulsions), and the mean-field Gross-Pitaevskii (GP) approximation (weak interactions and large fillings). To cover all the interaction regimes, numerical analysis will be also pursued, through truncated and exact diagonalization (ED) schemes and density-matrix renormalization-group (DMRG) methods. Details on these techniques are given in the Appendix D.

4.2.1 Identification of the qubit: effective two-level system

The Hamiltonian (3.8) is manifestly periodic in Ω with period 2π . Therefore, we can restrict our study to the first rotational Brillouin zone, (actually to half of it, i.e., $\Omega \in [0, \pi]$, due to the further symmetry $\Omega \leftrightarrow -\Omega$). In the absence of a barrier, the system is also rotationally invariant and therefore the particle-particle interaction energy does not depend on Ω . The many-body ground-state energy, as a function of Ω , is therefore given by a set of parabolas each corresponding to a well defined angular momentum state, shifted with respect to each other by a Galilean transformation and intersecting at the frustration points $\Omega_j = (2j + 1)\pi$ [99, 100]. The presence of a finite barrier, $\Lambda > 0$, breaks the axial rotational symmetry and couples different angular momenta states, thus lifting the degeneracy at Ω_j by an amount ΔE_1 , see Fig. 4.1. The larger Λ , the larger is ΔE_1 , corresponding to the width of the gap separating the first two bands. Provided other excitations are energetically far enough from the two competing ground-states, this will identify the two-level system defining the desired qubit and its working point.

Below, we discuss this issue with two different approaches: first, exploiting the mapping of the BH model to the quantum phase model, neglecting the fluctuations of the amplitude of the superfluid order parameter; this approach can capture, in particular, the regime of a large filling per lattice site [23, 81]. Then, via numerical calculation of the ground and first three excited energy levels of the BH model Eq. (3.8), we cover the case of lattice rings with a low filling.

4.2. The physical system

Quantum phase model. In the regime of filling much larger than one, the number fluctuations on each site can be neglected and the behavior of the system is governed by the quantum phase model [23, 81]. Here we are considering the model introduced in the section 3.2.1. The Hamiltonian of the system is given by Eq.3.7. We assume that the density of the superfluid is large enough to neglect the fluctuation of the number of atoms in each well. In this regime we can assume that the system dynamics is characterized by the phases of the superfluid order parameter ϕ_i 's, described by the quantum phase model [23] with Josephson coupling $J_i \sim \langle n \rangle t_i$ ($\langle n \rangle$ is the average number of bosons in each well). The magnetic flux Φ can be gauged away everywhere but at the site $(N - 1)$ -th [101]. Accordingly, the phase difference along nearest neighbour sites can be considered small in the 'bulk' and the harmonic approximation can be applied. The partition function can be written as a path integral: $Z = \int \mathcal{D}[\phi] e^{-S[\phi]}$, where the $S[\phi]$ is the Euclidean action. Adapting from the approach pursued by Rastelli et al. [102], all the phases ϕ_i except $\theta \doteq \phi_{N-1} - \phi_0$ can be integrated out (the integrals are Gaussian). The effective action reads (a detailed derivation is given in the Appendix B.2)

$$S_{eff} = \int_0^\beta d\tau \left[\frac{1}{2U} \dot{\theta}^2 + \frac{J}{2(N-1)} (\theta - \Phi)^2 - J' \cos(\theta) \right] - \frac{J}{2U(N-1)} \int d\tau d\tau' \theta(\tau) G(\tau - \tau') \theta(\tau') \quad (4.1)$$

with the potential $U(\theta) \doteq \frac{J}{N-1} (\theta - \Phi)^2 - J' \cos(\theta)$. For large $(N - 1)J'/J$ and moderate N , $U(\theta)$ defines a two-level system as it is demonstrated in Fig.4.2. The degeneracy point is $\Phi = \pi$: The two states are provided by the symmetric and antisymmetric combination of counter-circulating currents corresponding to the two minima of $U(\theta)$. We observe

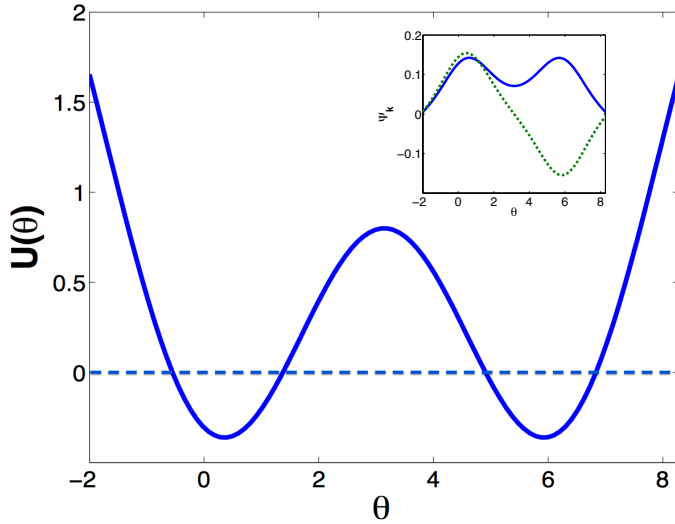


Figure 4.2: The double-well potential providing the single-ring-qubit for $[J'(N - 1)/J] = 16$ and $\Phi = \pi$. The inset shows symmetric ground state(solid line) and the first antisymmetric excited(dotted line) state wave functions of the double-well potential.

that breaking the Galilean invariance of the system provides an independent parameter J' facilitating the control of the potential landscape. The interaction between θ and the (harmonic) bulk degrees of freedom provides the non local term with $G(\tau) = \sum_{l=0}^{\infty} Y(\omega_l) e^{i\omega_l \tau}$, ω_l being Matsubara frequencies and $Y(\omega_l) = \omega_l^2 \sum_{k=1}^{(N-2)/2} \frac{1 + \cos[2\pi k/(N-1)]}{2JU(1 - \cos[2\pi k/(N-1)]) + \omega_l^2}$. The external bath vanishes in the thermodynamic limit and the effective action reduces to the Caldeira-Leggett one [102]. Finally it is worth noting that the case of a single junction needs a specific approach but it can be demonstrated to be consistent with Eq.(4.1). The result is that a single ring optical lattice with an impurity is described by the following effective Lagrangian (see Eq. (4.1)):

$$L = \frac{1}{2U} \dot{\theta}^2 + \frac{J}{N-1} (\theta - \Phi)^2 - J' \cos \theta \quad (4.2)$$

4.2. The physical system

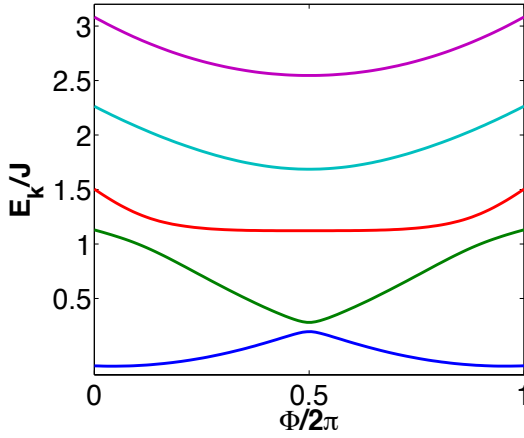


Figure 4.3: First five energy levels of the double-well potential as a function of the "flux". Here $U = 2$ and $[J'(N - 1)/J] = 16$.

Then we introduce the canonical momentum P in a usual way:

$$P = \frac{\partial L}{\partial \dot{\theta}} = \frac{1}{U} \dot{\theta} \quad (4.3)$$

After performing a Legendre transformation we get the following Hamiltonian:

$$H = J' \left[\frac{P^2}{2\mu} + \frac{J}{J'(N - 1)} (\theta - \Phi)^2 - \cos \theta \right], \quad (4.4)$$

where $\mu = J'/U$ is an effective mass of the collective particle. The quantization is performed by the usual transformation $P \rightarrow -id/d\theta$. For $\delta = \frac{J'(N-1)}{2J} > 1$ the effective potential in Eq. (4.4) can be reduced to a double well, as pictorially illustrated in Fig.4.2; for $\Phi = \pi$, the two lowest levels of such a double well are symmetric and antisymmetric superpositions of the states in the left and right wells respectively, as it is demonstrated in the inset of Fig.4.2. We find also the energy spectrum by numerically solving the Schrodinger equation with the finite difference method. As it is seen from the left panel of Fig.4.3 a two-level system is obtained around

Chapter 4. Realization of qubits with ring optical lattices

the frustration point. The effective Hamiltonian can be written as:

$$H \simeq \varepsilon \sigma_z \quad (4.5)$$

and the lowest two states are $|\psi_g\rangle = (0, 1)^T$ and $|\psi_e\rangle = (1, 0)^T$. An estimate for the gap energy can be found employing the WKB approximation [103](see for details Appendix C.3) :

$$\varepsilon \simeq \frac{2\sqrt{UJ'}}{\pi} \sqrt{\left(1 - \frac{1}{\delta}\right)} e^{-6\sqrt{J'/U}(1-1/\delta)^{3/2}}, \quad (4.6)$$

where $\delta > 1$. From this formula we can see that the limit of weak barrier and from intermediate to strong interactions is most favourable regime to obtain a finite gap between the two energy levels of the double level potential [95, 104, 60, 105]. We also note that the gap energy splitting can be controlled by the height of the impurity barrier.

Bose-Hubbard model. Here we study the low-lying spectrum of the BH model (3.8) by a numerical analysis, performed in the dilute limit (low filling regime). This is complementary to the quantum phase model, in that we take into account the effect of the number fluctuations, and hence of the amplitude of the superfluid order parameter, on the lattice sites. In Fig. 4.4 we show the ED results for $M = 16$ and $N = 4$. The top-left panel shows how large interactions and moderate barrier strengths cooperate to define a doublet of energy levels at $\Omega = \pi$, well separated in energy with respect to the higher excited states; weaker interactions and larger barrier strengths, in contrast, do not allow for a clear definition of a two-level system (top-right panel). We observe that for increasing Λ , as expected, the

4.2. The physical system

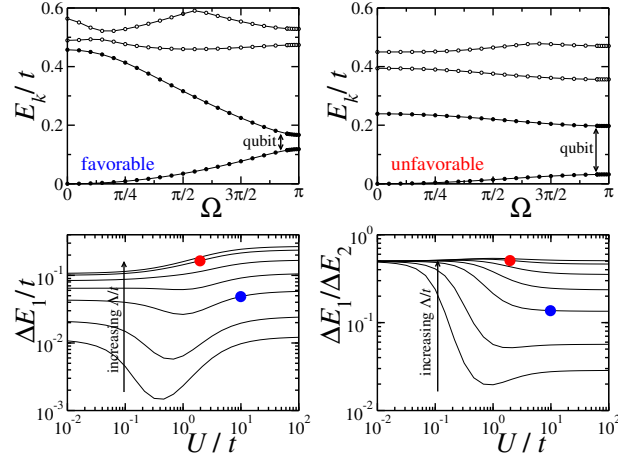


Figure 4.4: Low-energy spectrum of the BH model for various values of the interaction and the barrier strength at fixed size $M = 16$ and filling $N/M = 1/4$. Upper panels: the four lowest energy levels as a function of Ω , for $U/t = 10$, $\Lambda/t = 0.5$ (left) and $U/t = 2$, $\Lambda = 5$ (right). Lower panels: behavior of ΔE_1 and $\Delta E_1/\Delta E_2$ as a function of U , for different values of Λ/t (curves from bottom to top: $\Lambda/t = 0.1, 0.2, 0.5, 1, 2, 5, 10$).

gap increases and the bands become flatter, thus weakening the dependence of the energy on Ω . The lower two panels display a complete analysis of the behavior of the spectral gap and its distance to the next excited level at $\Omega = \pi$ as a function of interactions and barrier strength, allowing us to identify the parameter regime for the existence of an effective two-level system. We notice in particular that weakly interacting gases cannot give rise to a sensible qubit within this approach, since one cannot isolate two levels out of the many-body spectrum with the sole tuning of the barrier strength, while this is possible for larger interaction strengths U .

Using the above results, we conclude that the low-energy spectrum of the system (3.8) may define a qubit over a broad range of lattice filling values. It is vital for the manipulation of the qubit, though, to explore its quality. This implies in particular to study the dependence of ΔE_1 on the system size and on the interaction strength, as will be considered in the next Section 4.3. We will also analyze the nature of the qubit states; this

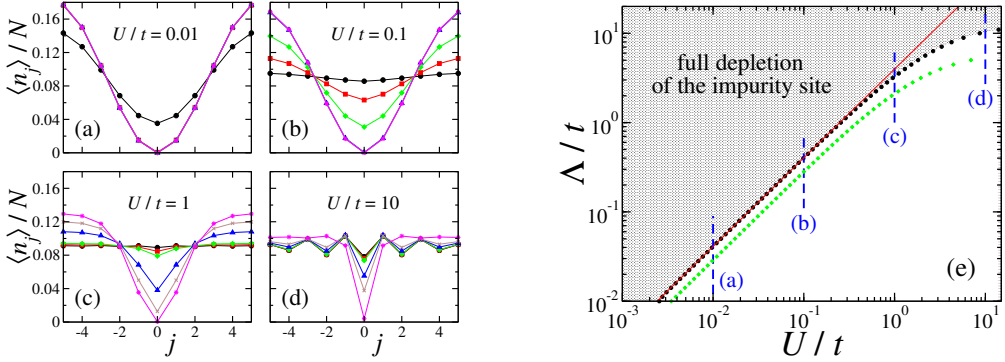


Figure 4.5: Panels a-d): spatially-resolved density profiles $\langle n_j \rangle / N$ at $\Omega = \pi$, along a ring with $M = 11$ sites and $N = 5$ particles, for different interaction regimes. The various data sets correspond to different values of the barrier strength: $\Lambda/t = 0.01$ (black circles), 0.05 (red squares), 0.1 (green diamonds), 0.5 (blue triangles), 1 (brown crosses), 5 (orange stars). Panel e): critical value Λ_c as a function of U discriminating the parameters region in which the boson density per particle at the barrier position is less than the threshold value $\varepsilon = 10^{-3}$ (black circles refer to $N/M = 5/11$, green diamonds are for $N/M = 4/16$). Vertical dashed lines denote the cuts analyzed in the different left panels, for the data set $N/M = 5/11$, while the straight red line is a power-law fit $(\Lambda/t)_c \propto (U/t)^{0.99374}$.

will be the subject of Section 5.2.

4.2.2 Density profiles

Before presenting our results concerning the quality of the qubit, we first focus on the density profiles of the gas close to the qubit working point, $\Omega = \pi$.

An evident effect of the barrier is a suppression of the particle density in its immediate proximity; depending on the ring size, the whole density profile along the ring may well be affected. The interplay between the interaction strength U and the barrier intensity Λ implies different behaviors [86], as exemplified in Fig. 4.5 (panels a-d) for relatively small rings. The depth of the density depression increases monotonically with Λ (inside each panel), while its width decreases with increasing U (see the different

4.3. Energy gap of the two-level current-flow system

panels) since the density can be suppressed at the impurity site at the expense of multiple occupancy of the other sites; the latter effect implies a non trivial dependence of the healing length on interaction strength. At strong repulsive interactions we also observe small Friedel-like oscillations of the density, which are a consequence of the peculiar strong correlations of 1D bosons that make their response to impurities similar to fermions.

We note that a sufficiently large barrier (at fixed U) makes the density profile vanish, thus effectively disconnecting the ring (panels a-d of Fig. 4.5). The barrier strength required to disconnect the ring depends on the interaction strength. Panel e) of Fig. 4.5 shows the result of a thorough analysis of the transition line in the Λ - U plane: for a wide range of interaction strengths, the critical barrier height Λ_c displays a nearly perfect linear behavior with U . The prefactor turns out to be nearly proportional to the filling.

4.3 Energy gap of the two-level current-flow system

In this section we study in detail the spectroscopy of the qubit. We will analyze how the energy gaps ΔE_1 , ΔE_2 between the ground and, respectively, the first-excited / second-excited energy levels of the many-body Hamiltonian (3.8) depend on the system size and on the filling, for different Λ and U . We find that the qubit is well resolved in the mesoscopic regime of intermediate ring sizes, and that it is at best separated from the higher energy levels of the many-body spectrum in the regime of strong interactions and weak barrier.

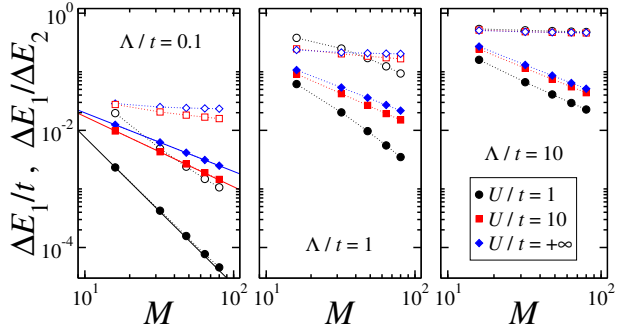


Figure 4.6: Finite-size scaling of the qubit gap ΔE_1 in units of t (filled symbols) and of the ratio between the gaps $\Delta E_1/\Delta E_2$ (empty symbols), at fixed density $N/M = 1/4$. Different colors stand for three values of interaction U/t , as specified in the legend. The various panels are for a fixed barrier $\Lambda/t = 0.1$ (a), 1 (b), 10 (c). Straight lines in the left panel correspond to the power-law behavior predicted by the Luttinger-liquid analysis in the small-barrier limit (5.7), for the values of the Luttinger parameter $K|_{U=\infty} = 1.00$, $K|_{U=10} = 1.20$ and $K|_{U=1} = 2.52$.

4.3.1 Scaling with the system size

In Fig. 4.6 we show both the qubit gap ΔE_1 and the separation of the two levels from the rest of the spectrum in terms of $\Delta E_1/\Delta E_2$, as obtained by DMRG simulations at constant filling $N/L = 1/4$ (see D.3). The three panels correspond to different barrier intensities, from very weak to very high; each panel containing the three curves at varying interactions from moderate to hard-core. A clear power-law decay of ΔE_1 is found in all the regimes; the exponents depend on the interplay between the barrier and interaction strengths.

In the small-barrier limit, we can work out the observed scaling law of the gap analytically resorting to the Luttinger-liquid effective field theory (see, e.g., Ref. [86]). Indeed we obtain that the quantum fluctuations of the density renormalize the barrier strength according to $\Lambda_{\text{eff}} \sim \Lambda(d/L)^K$, where d is a short distance cut-off of the low-energy theory, $L = aM$ is the system size, a being the lattice spacing, and K is the Luttinger

4.3. Energy gap of the two-level current-flow system

parameter [86]. This yields the scaling of the gap with M as,

$$\Delta E_1 \sim \nu \Lambda_{\text{eff}} \sim M^{-K}, \quad (4.7)$$

in agreement with the result found in Ref. [106] for a single impurity potential. As illustrated in panel a) of Fig. 4.6, we find a very good agreement between the numerical data and the power-law behavior dictated by the Luttinger parameter obtained via the Bethe-Ansatz solution of the continuous model (a Lieb-Liniger gas [107]), suitable in the dilute limit of the BH model ³. For stronger barriers, interestingly, we observe in Fig. 4.6(b-c) that the gap scales again as a power-law beyond the regime of validity of the analytical predictions. We also notice that the scaling of the gap is closely related to the scaling of the persistent currents flowing along the ring [109], which is determined by the shape of the ground state energy band.

By looking at the separation of the effective two-level system from the rest of the spectrum (dashed lines in Fig. 4.6), we can then start to identify an ideal regime of size, interaction and barrier for a realistic operational realization of the qubit. At low barrier intensity $\Lambda/t = 0.1$ (panel a), indeed, a mesoscopic lattice of few tens of sites filled with mildly interacting bosons appears to be the best choice, since it would allow for a qubit gap of some $10^{-3}t$, while this being only a $\simeq 10^{-2}$ fraction of the second excitation energy. Rings that are too large in size would improve the definition of the two-level system, yet at the price of too small a resolution of the qubit levels for practical addressing. When the barrier becomes stronger, the size dependence of $\Delta E_1/\Delta E_2$ becomes less and less important, with

³We have checked as well (not shown) that the same values for K , within numerical precision, are extracted from the fit of the decay of the first-order correlation function with the functional form predicted in [108] for the finite-size system.

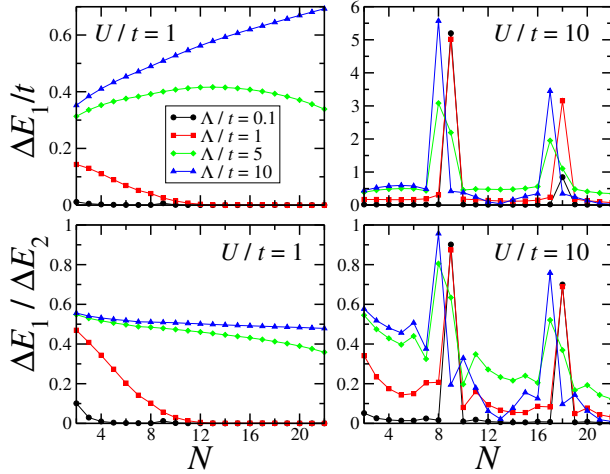


Figure 4.7: Energy gap ΔE_1 in units of t and the ratio $\Delta E_1/\Delta E_2$ for $M = 9$ lattice sites, at $\Omega = \pi$. We consider the interaction strengths $U/t = 1$ (left) and 10 (right). In each plot the various curves stand for $\Lambda/t = 0.1$ (black circles), 1 (red squares), 5 (green diamonds) and 10 (blue triangles). We use an ED technique where, for $N/M > 1$, we allowed a truncation in the maximum occupation per site equal to 6 particles.

its absolute value increasing more and more (i.e., the qubit gets less and less isolated). Still, at intermediate barrier strengths $\Lambda/t = 1$ (panel b), a nicely addressable pair of levels with splitting of some $10^{-2}t$, and a relative separation from the spectrum of order $10^{-1}t$, can be obtained in a mesoscopic lattice of $M \simeq 16$ sites with relatively weak interactions $U = t$. Conversely, if the barrier is strong enough to effectively cut the ring, the low lying levels of the many-body spectrum get almost equally spaced and therefore the qubit definition is poor.

4.3.2 Dependence of the qubit energy spectrum on the filling factor in mesoscopic rings

We concentrate next on the mesoscopic regime of few lattice sites, where, according to our scaling analysis at fixed small filling, the qubit enjoys simultaneously a clear definition with respect to the other excited states

4.3. Energy gap of the two-level current-flow system

and a good energy resolution.

In Figs. 4.7 and 4.8 we present our results for the gap ΔE_1 and ΔE_2 as a function of the filling at fixed system size, studying its dependence on the barrier and on the interaction strength. The top panels of Fig. 4.7 present the data for fixed interaction strength ($U/t = 1$ and $U/t = 10$, respectively) with the curves representing barrier strengths from weak to strong. At small U (top-left), we observe a smooth dependence of ΔE_1 on the boson filling, as expected in the superfluid regime of the Hamiltonian (3.8), of which the small ring is reminiscent. The increase of the barrier strength has two effects: first, at fixed filling, it increases the gap since it enhances the effect of the breaking of the rotational invariance and therefore lifts the degeneracy at half-flux. In addition, it changes the dependence of the gap on the filling from being monotonically decreasing to monotonically increasing, passing through a crossover situation. Since the healing length scales as $\xi \propto 1/\sqrt{\nu U}$, at small barrier strengths, a weakly interacting Bose gas screens the barrier, effectively reducing its height as the density is increased. On the other hand, for a large barrier, the system is effectively in the tunnel limit, and the situation is reversed. The barrier strength is effectively enhanced, since the tunnel energy required to move one particle from one side of the barrier to the other increases if the number of particles or the interaction strength are increased (in order to accommodate the tunnelling particle, the other particles have to readjust their configuration).

At large U (top-right) in Fig. 4.7, ΔE_1 displays a more complex dependence on the filling, with pronounced peaks at particle numbers commensurate (or quasi) with the size, related to the presence of Mott lobes in the phase diagram of Hamiltonian (3.8) [110]. For weak barrier, indeed, the peaks appear at integer values of N/M , while for very strong potential

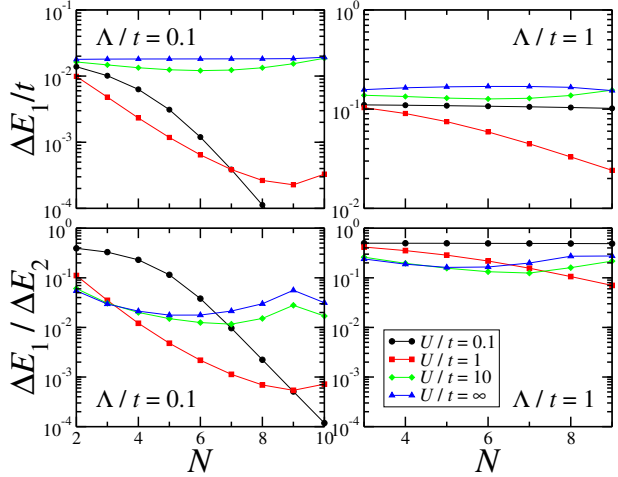


Figure 4.8: Same as in Fig. 4.7, but for $M = 11$ lattice sites and for fixed barrier strength $\Lambda/t = 0.1$ (left), 1 (right). The different curves are for $U/t = 0.1$ (black circles), 1 (red squares), 10 (green diamonds) and ∞ (blue triangles).

constrictions the density is suppressed on one site: the system is close to a lattice with $M - 1$ sites and peaks are consequently shifted. At intermediate barrier strengths we can observe a transient between the two regimes and broader peaks appear. Considering the very small system size, this effect arises because the presence of the healing length affects the whole bosonic density profile of the ring.

The top panels of Fig. 4.8 present data for fixed barrier strength ($\Lambda = 0.1$ and $\Lambda = 1$, respectively) with the curves representing interaction strengths from extremely weak to infinite values. First, we can clearly see the non monotonic dependence of the gap on U , which was illustrated in Fig. 4.4, to hold at all fillings in both panels. Secondly, we notice that the dependence of ΔE_1 on N drastically changes increasing the interaction strength, displaying different regimes: quickly decreasing, non monotonic and almost constant. The rapid decrease of the energy gap at weak interactions can be understood (through a perturbative argument) in terms of level mixing of single-particle energies, which increases with the num-

4.3. Energy gap of the two-level current-flow system

ber of bosons involved [111]. In the opposite regime of hard core bosons, the energy gap is of the same order as that of the non-interacting Fermi gas. This can be readily understood in terms of the TG Bose-Fermi mapping: indeed, in a non-interacting Fermi gas the energy gap is given by $\Delta E_1 = (\sum_{j=1}^{N-1} \varepsilon_j + \varepsilon_{N+1}) - \sum_{j=1}^N \varepsilon_j$, where ε_j are the single-particle energies. In particular, for a small barrier, using perturbation theory, one obtains that the single-particle energy gaps $\varepsilon_{j+1} - \varepsilon_j$ are identical for all the avoided level crossings, hence the gap ΔE_1 is independent of the filling.

The lower panels of Figs. 4.7 and 4.8 display the ratio $\Delta E_1/\Delta E_2$. This allows us to identify the low-barrier, intermediate-to-large interaction regime at arbitrary filling as the most favorable for the qubit. Indeed, depending on the interaction strength, a too large barrier yields an unfavorable situation similar to the one depicted in the top-right panel of Fig. 4.4, where $\Delta E_2 \sim \Delta E_1$. It is interesting to notice that these unfavorable cases correspond to values of barrier and interaction strength in the right panel of Fig. 4.5 where the ring is effectively disconnected. This allows us to identify the ratio Λ/U as a useful parameter to define the quality of the qubit in terms of its energy resolution: the most advantageous parameter regime for the qubit corresponds to the lower half-plane in Fig. 4.5 (e), below the critical line.

In summary, this analysis shows that a particularly favorable regime for the energy resolution of the qubit is the Tonks-Girardeau and small-barrier limit, where the system has a well defined gap, independent of the particle number and well separated from the remaining part of the many-body spectrum. However, for the realization of a tunable-gap qubit, the limits of weak interaction with low filling and intermediate interaction with high filling can be useful.

Chapter 4. Realization of qubits with ring optical lattices

We close this section providing the order of magnitude for the gaps discussed above. For a ^{87}Rb gas in a mesoscopic ring-shaped deep optical lattice of $\sim 50\mu\text{m}$ circumference and 10 lattice wells, the hopping energy is of the order of $t \sim 0.5\text{kHz}$. This yields a typical energy scale for the gap of tens to few hundreds of Hz, depending on the choice of barrier strength, well within the range of experimental accessibility.

4.4 Conclusions

In this chapter we studied a system of bosonic atoms loaded in a 1D ring-shaped optical lattice potential with a localized barrier on a given site of the lattice. Besides its possible exploitation in quantum technology, the system provides a paradigmatic arena to study the interplay between quantum fluctuations, interactions and the role of the barrier potential.

At first we studied the limit of high filling per lattice site, where the quantum phase model is applicable. In this limit, the number fluctuations of particles in each lattice well are negligible. We demonstrated that with help of the path integral representation of the partition function, it is possible to obtain the low energy effective action (after integrating out all the phase slips except the one across the weak link), which takes the form of quantum particle in a double well potential. By the numerical study of the one-body Schrödinger equation we demonstrated that for the intermediate interactions the system can be effectively considered as a qubit. Moreover, by the numerical study(mostly exact diagonalization) of the Bose-Hubbard model, we provided direct evidence that the qubit dynamics can be achieved beyond the pure superfluid phase dynamics conditions (described by the quantum phase model). We quantified the scaling of the gaps ΔE_1 and ΔE_2 with system size. Our results indicate that ΔE_1 is appreciable for

4.4. Conclusions

small and mesoscopic systems and that it is suppressed in the thermodynamic limit (Fig. 5.5), decaying as a power law with system size. Then we considered ring sizes ranging from few lattice sites ($10 - 20$) to several tens of sites (100) and we studied scaling of the energy gaps with the number of particles.

CHAPTER 5

Coherent superposition of current flows in the AQUID

5.1 Introduction

In this chapter we focus on the superposition states of current flows in AQUID. We assess the detectability of the latter through the study of the momentum distribution. In the first part of this chapter, we focus on the state readout of different macroscopic superposition states and methods introduced in this section can also be applied for the qubit(which has been introduced in a previous chapter) state readout. To achieve the goal we combine analytical and numerical approaches to study TOF images as function of barrier strength, interaction and filling.

In a quantum fluid confined on a toroidal geometry, the persistent current phenomenon is the periodic particle-current response to the flux of an applied $U(1)$ gauge potential. This is a manifestation of the Aharonov-Bohm effect at the many-body level, indicating that the phase coherence length of the fluid extends to the whole system. Persistent currents were first observed in electronic systems subjected to a magnetic field, such as bulk superconductors [112, 113, 114], and more recently also in normal resistive metal rings [115, 116, 117, 118]. However, the first convincing experimental observation was reported in 2009 in Ref. [118], where an array

Chapter 5. Coherent superposition of current flows in the AQUID

of rings was integrated into the end of a cantilever and the shift in the cantilever resonant frequency was mapped to the amplitude of the persistent current in the single ring.

In a recent work, an interacting one-dimensional (1D) Bose gas confined in a ring trap subjected to an artificial $U(1)$ gauge potential [86] has been thoroughly studied. There, it was analyzed how the persistent current amplitude depends, at fixed ring length L , on the barrier height and on the interaction strength, finding an optimal regime at intermediate interaction strength, where the current amplitude is maximal, due to the interplay between classical screening and quantum fluctuations. In the second part of this Chapter, we focus on the mesoscopic nature of the persistent current, which vanishes for macroscopic system sizes (i.e., $L \rightarrow \infty$).

This chapter is outlined as follows. In Section 5.2 we show how the state of the AQUID can be read out through TOF expansion images of the gas. We also study in detail the signatures of superposition states in TOF type of experiments. In Section 5.3 we consider the models for persistent currents induced by an artificial gauge field applied to interacting ultra-cold bosonic atoms in a tight ring trap. Using both analytical and numerical methods, we study the scaling of the persistent current amplitude with the size of the ring. In the strongly interacting regime we find a power-law scaling, in good agreement with the predictions of the Luttinger-liquid theory. In Section 5.3.1 by exploring all interaction regimes we find that the scaling is optimal, i.e. the current amplitude decreases slower with the system size, at intermediate interactions. We summarize and discuss our results in Section 5.4. Technicalities on the employed methods and further details are provided in the Appendices A and D.

For the sake of clarity, it is worth noting that while the author of this

5.2. Momentum distributions

thesis was involved in suggesting with Prof. Amico(also the author made preliminary calculations with the exact diagonalization method which were used as a benchmark for DMRG simulations) the project regarding the scaling of persistent currents most of the analytical results in Section 5.3 were obtained by Marco Cominotti and DMRG simulations were performed by Davide Rossini and Mateo Rizzi. In Section 5.2 exact diagonalization results have been obtained by the author of the thesis.

5.2 Momentum distributions

The momentum distribution is experimentally accessible in cold atoms experiments via TOF expansion measurements, by averaging over many repeated TOF realizations [3, 30], and is employed to get information about the current circulation along the ring [119, 120, 121]. It is defined as the Fourier transform with respect to the relative coordinate of the one-body density matrix $\rho_{(1)}(\mathbf{x}, \mathbf{x}') = \langle \hat{\psi}^\dagger(\mathbf{x}) \hat{\psi}(\mathbf{x}') \rangle$:

$$n(\mathbf{k}) = \int d\mathbf{x} \int d\mathbf{x}' \langle \hat{\psi}^\dagger(\mathbf{x}) \hat{\psi}(\mathbf{x}') \rangle e^{i\mathbf{k}\cdot(\mathbf{x}-\mathbf{x}')}, \quad (5.1)$$

where \mathbf{x} and \mathbf{x}' denote the position of two points along the ring's circumference. Although, in general, \mathbf{k} is a three dimensional wave vector, here we restrict the treatment to consider a TOF picture along the symmetry axis of the ring, and therefore two dimensional \mathbf{k} 's. To adapt Eq. (5.1) to our lattice system, we use $\hat{\psi}(\mathbf{x}) = \sum_{j=1}^M w_j(\mathbf{x}) \hat{b}_j$, where $w_j(\mathbf{x}) = w(\mathbf{x} - \mathbf{x}_j)$ is the Wannier function localized on the j -th lattice site, and \mathbf{x}_j denotes the position of the j -th lattice site. Thereby, Eq. (5.1) can be recast into

$$n(\mathbf{k}) = |\tilde{w}(\mathbf{k})|^2 \sum_{l,j=1}^M e^{i\mathbf{k}\cdot(\mathbf{x}_l - \mathbf{x}_j)} \langle \hat{b}_l^\dagger \hat{b}_j \rangle, \quad (5.2)$$

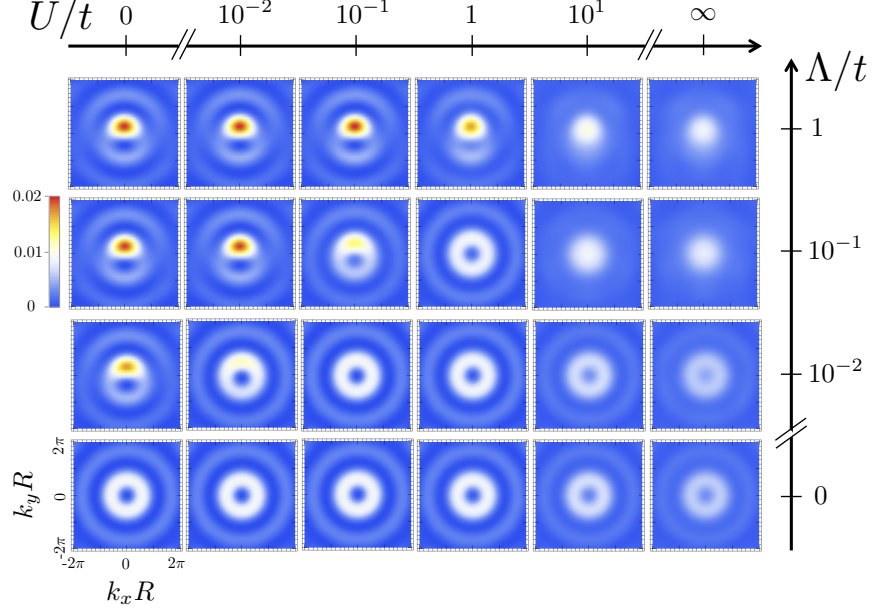


Figure 5.1: Ground state momentum distribution (TOF) close to the degeneracy point: $\Omega = \Omega^+ = \pi + \varepsilon$ (hereafter we fix $\varepsilon = 10^{-3}$). For $\Omega = \Omega^+$, the ground state corresponds to a symmetric superposition of the flow states with zero and one quanta of circulation. The superposition depends on the interplay between U and Λ : lines $\Lambda/t = 0, 0.01, 0.1, 1$; columns $U/t = 0, 0.01, 0.1, 1, 10, \infty$. For the filling value, $N/M = 5/11$, used in these graphs, larger values of Λ yield TOF images very close to those for $\Lambda/t = 1$. The results were obtained with exact diagonalization.

where $\tilde{w}(\mathbf{k})$ is the Fourier transform of the Wannier function.

To avoid effects of the proximity of the superfluid-insulator transition, in the following analysis we focus on incommensurate fillings (see Section 4.3.2 for a more detailed discussion).

In absence of the barrier $\Lambda = 0$, the system has no circulation for $\Omega < \pi$ and one quantum of circulation for $\Omega > \pi$, while at the frustration point $\Omega = \pi$, it is a perfectly balanced superposition of the two states. As a consequence, the momentum distribution is peaked at $\mathbf{k} = 0$ for $\Omega < \pi$ and is ring-shaped for $\Omega > \pi$, as discussed in Appendix C.1. At $\Omega = \pi$, instead, it displays an interference of the two situations, reflecting the coherent superposition of the two states (see Appendix C.2). When $\Lambda \neq 0$,

5.2. Momentum distributions

the superposition state occurs for a wide range of Ω , thereby displaying interference effects as shown in Fig. 5.1. The relative weight of the two-quanta-of-circulation components in the superposition strongly depends on Ω , Λ , and U . In particular, at the frustration point the superposition is perfectly balanced, independently of Λ and U . Away from the frustration points, the relative weights tend to the unperturbed ones carrying zero or one quantum of angular momentum. This phenomenon occurs over a distance in $\Omega - \pi$ that depends on Λ : the smaller is Λ , the faster the unperturbed weights are recovered. For this reason, in Figs. 5.1 and 5.3, we slightly off-set Ω from the frustration point (the weights of the circulating states are not equal, yet close enough to ensure that both angular momentum states contribute significantly to the superposition). For $\Omega > \pi$, the component carrying one quantum of angular momentum has a larger weight in the superposition, making the effect of the barrier and its screening easily detectable in the TOF image; the opposite situation occurs for $\Omega < \pi$. The TOF results shown in Fig. 5.1 and 5.3 quantitatively depend on the choice of Ω , but the screening effect of the barrier and the detectability of the superposition are only weakly affected.

To understand the TOF results of Fig. 5.1, it is instructive to consider first the case without interactions, $U = 0$, that is analytically accessible. The corresponding momentum distribution close the frustration point and for a weak barrier reads (see Eq. (C.4) in Appendix C.2 for the derivation)

$$\begin{aligned} n(\mathbf{k}) = & \sin^2(\varphi/2) J_n^2(|\mathbf{k}|R) + \cos^2(\varphi/2) J_{n+1}^2(|\mathbf{k}|R) \\ & + \sin(\varphi) \cos(\gamma_{\mathbf{k}}) J_n(|\mathbf{k}|R) J_{n+1}(|\mathbf{k}|R), \end{aligned} \quad (5.3)$$

where the Bessel functions J_n correspond to states with angular momentum n , and $\gamma_{\mathbf{k}}$ is the angle along the ring; the parameter φ is a function of the

flux and the barrier strength (see Eq. (C.3) in Appendix C.2). Eq. (5.3) shows that the TOF images allow one to visualize the superposition between states with different angular momenta: the functions J_0 and J_1 interfere, giving rise to *a peak at zero \mathbf{k} and a fringe with ring-shaped symmetry*. The detectability of this feature increases with the barrier strength Λ . Note that the angular position of the peak in momentum space depends on the position of the barrier in real space along the ring; it would be affected by a phase shift between the two states of well-defined angular momentum.

The superposition state for small U can be analyzed in a similar way. We note in Fig. 5.1 that, for sufficiently weak interactions, an angular modulation of the ring-shaped momentum distribution arises. A stronger barrier makes the angular asymmetry increasing, while the interaction strength, by screening the barrier, leads to the opposite phenomenon.

Upon increasing the interaction strength from intermediate to very large, we observe a smearing of the modulated ring shape TOF images. This is an effect of increased quantum fluctuations, which leads, for strong barrier strengths, to a single maximum centred at non-zero \mathbf{k} values.

The very different TOF images between the regimes of weak and strong interactions can be understood by recalling the different nature of the superposition state in the various interaction regimes [57, 58]. For instance, at zero or very weak interactions, within the GP regime, the many-body state is a coherent state of single particle superpositions. Increasing the interaction strength to the intermediate regime the superposition is described by the so-called NOON state $|N, 0\rangle + |0, N\rangle$, i.e., a macroscopic superposition of states where all bosons occupy either the state with zero angular momentum or the one carrying one quantum of angular momentum. For increasing interactions this many-body entangled state matches

5.2. Momentum distributions

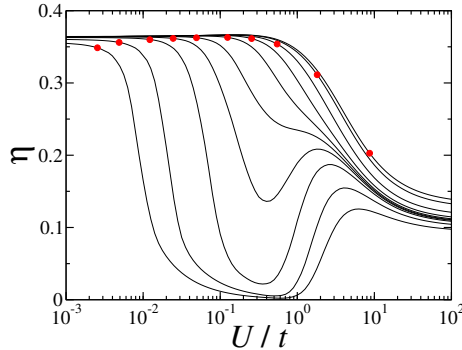


Figure 5.2: Averaged contrast η vs interaction strength U/t for different values of the barrier strength (curves from left to right: $\Lambda/t = 0.01, 0.02, 0.05, 0.1, 0.2, 0.5, 1, 2, 5, 10$). The red circles denote the value of $\eta(U_c/t)$, for each value of Λ/t , where U_c/t has been defined from the analysis of Fig. 4.5.

the known macroscopic superposition of Fermi spheres at very large interactions [58, 59].

For all regimes of interactions, we notice that the TOF images become independent of the barrier above a critical value of the barrier strength, which agrees well with the critical value Λ_c for disconnecting the ring, as identified in Fig. 4.5. Globally, we observe that good-quality TOF images allowing one to easily identify the superposition of current states as a modulated ring structure are found for a ratio Λ/U in the vicinity or above the critical line of Fig. 4.5(e).

To quantify the detectability of the superposition state in the momentum distribution for different barrier and interaction strengths, we define the averaged contrast between the momentum distribution with and without the barrier

$$\eta = \frac{\int d\mathbf{k} |n_{\Lambda \neq 0}(\mathbf{k}) - n_{\Lambda=0}(\mathbf{k})|}{\int d\mathbf{k} n_{\Lambda \neq 0}(\mathbf{k}) + n_{\Lambda=0}(\mathbf{k})}, \quad (5.4)$$

reflecting the modification in the integrated momentum distribution due to superposition of states induced by the barrier. We find that η is non-monotonic upon increasing the interactions between the particles while

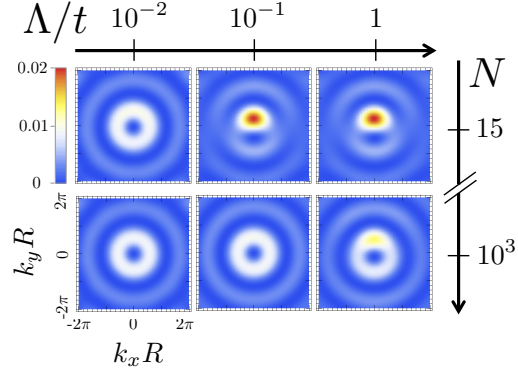


Figure 5.3: Ground state momentum distribution (TOF) close to the degeneracy point: $\Omega = \Omega^+ = \pi + \varepsilon$ for $U/t = 10^{-2}$, $M = 11$ and $N = 15, 10^3$ (obtained from truncated ED and GP respectively). The TOF pictures are qualitatively similar to the ones in Fig. 5.1, but the features of the superposition appear at larger values of Λ , compared to the case at lower filling.

keeping the barrier strength fixed—Fig. 5.2. This is an effect of the non-monotonic screening of the barrier as a function of interaction strength, first predicted in Ref. [86] through the study of the persistent-current amplitude.

Finally, we comment on the expected behavior for a system with filling larger than one. In Fig. 5.3 we show the TOF images for larger fillings, ranging from values of N/M close to one, obtained with truncated ED, to fillings much larger than one, obtained solving the GP Eq. (3.13). In both cases we note that the TOF images are qualitatively the same as the ones shown in Fig. 5.1, and therefore our analysis is relevant also for systems with larger number of particles, like the ones employed in the experiments so far. We notice that, at higher filling, a larger barrier strength is needed, with respect to the lower filling case, to produce the same superposition and to observe the same TOF.

5.3. Optimal scaling of persistent currents for the AQUID

5.3 Optimal scaling of persistent currents for the AQUID

Here we study the model introduced in Section 3.3. The corresponding Hamiltonian reads:

$$\mathcal{H} = E_0 \sum_{j=1}^N \left[\left(-i \frac{\partial}{\partial \theta_j} - \Omega \right)^2 + \frac{L}{2\pi a} \Lambda \delta(\theta_j) + \frac{N\gamma}{2\pi} \sum_{l=1}^N \delta(\theta_l - \theta_j) \right], \quad (5.5)$$

where we adopted the zero-point single particle kinetic energy $E_0 = 2\pi^2 \hbar^2 / mL^2$ as natural energy unit. Here a is a length unit which will be specified below, and $\gamma = mg/\hbar^2 n$ is the dimensionless interaction parameter, with g the contact interaction coupling. The spatially-averaged particle current $I(\Omega)$ has been obtained, at zero temperature and in the stationary regime, from the ground-state energy $E(\Omega)$ via the thermodynamic relation [122].

$$I(\Omega) = -(1/2\pi\hbar) \partial E(\Omega) / \partial \Omega \quad (5.6)$$

In the absence of the barrier and for any interaction strength, the ground-state energy of the Hamiltonian (5.5) is a series of parabolas, $E(J, \Omega) = NE_0(\Omega - J)^2 + E_{\text{int}}$, where E_{int} is the Ω -independent interaction energy, corresponding to states of well-defined angular momentum and circulation J , periodically shifted by a Galilean transformation in Ω with period 1 [123], and intersecting at the frustration points $\Omega_j = (2j + 1)/2$. The corresponding persistent current is a perfect sawtooth of amplitude $I_0 = NE_0/\pi\hbar = 2\pi\hbar n/mL$ [124, 100]. We notice that the amplitude of the persistent current vanishes in the thermodynamic limit ($N \rightarrow \infty, L \rightarrow \infty$, at fixed $n = N/L$), as is well known [118, 125].

In the presence of a barrier that breaks the rotational symmetry, a

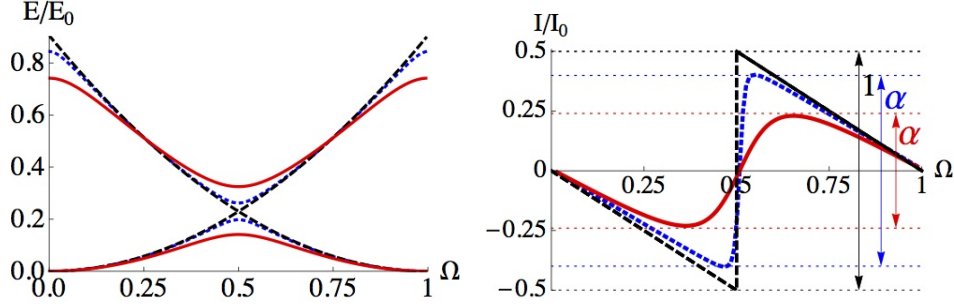


Figure 5.4: Energy spectrum and persistent current in the first rotational Brillouin zone, in the TG limit, for density $n = 0.25/a$, and zero barrier (black dashed line), barrier strength $\Lambda = 0.1$ (blue dashed line), and $\Lambda = 1$ (red solid line).

gap opens in the many-body energy spectrum at the frustration points, mixing states that differ by one quantum of circulation. The corresponding persistent current is smeared, with a shape depending on barrier and interaction strengths [126, 86]. In Fig. 5.4 we show an example of the energy spectrum and of the corresponding particle current as function of the flux Ω . In the following, we study the scaling of the current amplitude $\alpha = (I_{\max} - I_{\min})/I_0 = 2I_{\max}/I_0$ with the system size, keeping fixed the density n , in the presence of barrier and interactions.

In order to solve the many-body problem associated with the Hamiltonian (5.5) in all the regimes of interaction γ and barrier strength Λ we have resorted to a combination of numerical and analytical, exact and approximate, techniques, for which more details are given in Appendices A and D. At arbitrary barrier strength and for intermediate-to-strong interactions we have adopted a numerical technique based on the density matrix renormalization group (DMRG)(see Appendix D.3), in which space has been discretized in M lattice sites of spacing $a = L/M$, that we take as a length unit. Numerical simulations have been done by mapping the Hamiltonian given by Eq. (5.5) onto the 1D Bose-Hubbard(BH) model: $H_{BH} = \sum_{i=1}^M [-t(e^{-i\frac{2\pi}{M}\Omega} b_j^\dagger b_{j+1} + H.c.) + (U/2)n_j(n_j - 1) + \Lambda\delta_{j,1}n_j]$, which

5.3. Optimal scaling of persistent currents for the AQUID

in the limit of high number of lattice sites resembles a homogeneous ring system. The BH model parameters are linked to the continuum model ones by the following relations: $\hbar/2m = ta^2$, and $\gamma = UM/2tN$.

In the two opposite limiting cases of non interacting (NI) and infinitely interacting Tonks-Girardeau (TG) gas, the many-body problem reduces to a single-particle one and is therefore solved exactly(see Appendix A.3). At weak interactions the bosonic fluid is described within a mean-field approximation via the Gross-Pitaevskii (GP) equation(see Section 3.5). Its ground state is a dark soliton pinned at the position of the barrier [86].

Finally, in order to give a theoretical interpretation to the numerical results at strong interaction, we use the Luttinger liquid (LL) theory. We treat perturbatively the barrier contribution to the Hamiltonian, in the two opposite cases of small and large barrier strength(see for details Appendix A.4.1). For small barrier strength we obtain the persistent current $I(\Omega) = -I_0 \delta\Omega(1 - \pi/\sqrt{(2\pi\delta\Omega)^2 + (\Lambda_{\text{eff}}L/2\pi a)^2})$, where $\delta\Omega = \Omega - 1/2$, $\Lambda_{\text{eff}} = \Lambda(d/L)^K$ is the effective barrier strength renormalized by the density quantum fluctuations and d is the short-distance cutoff of the LL theory.

The amplitude of the current is then given by $\alpha = 1 - (3/2)(\Lambda_{\text{eff}}L/2\pi^2 a)^{2/3}$, and hence we obtain the scaling

$$1 - \alpha \sim L^{(2/3)(1-K)}. \quad (5.7)$$

In the opposite regime of large barrier strength, we obtain the persistent current $I(\Omega) = -(2t_{\text{eff}}n/\hbar)\sin(2\pi\Omega)$, where $t_{\text{eff}} = t(d/L)^{1/K}$ is the effective tunneling amplitude across the barrier, renormalized by the quantum fluctuations of the phase(see Appendix A.4.1). The tunneling amplitude t across the barrier, which is small in the large-barrier limit, is related to the barrier strength via $t/L \sim (\hbar\omega_c)^{1+K} (L/a\Lambda)^K$, with cut-off energy

$\hbar\omega_c \sim NE_0 \sim nL^{-1}$. Therefore the current amplitude for large barrier scales as

$$\alpha \sim L^{1-1/K}. \quad (5.8)$$

In the next section, we will compare the predictions of Eqs. (5.7) and (5.8) with the numerical data, showing that they display a good agreement.

5.3.1 Scaling of persistent currents with a system size

In Fig. 5.5 we show the scaling of the persistent current amplitude α with the system size, at fixed density $n = 0.25/a$, for various values of barrier and interaction strengths. We observe that for all values of the barrier the

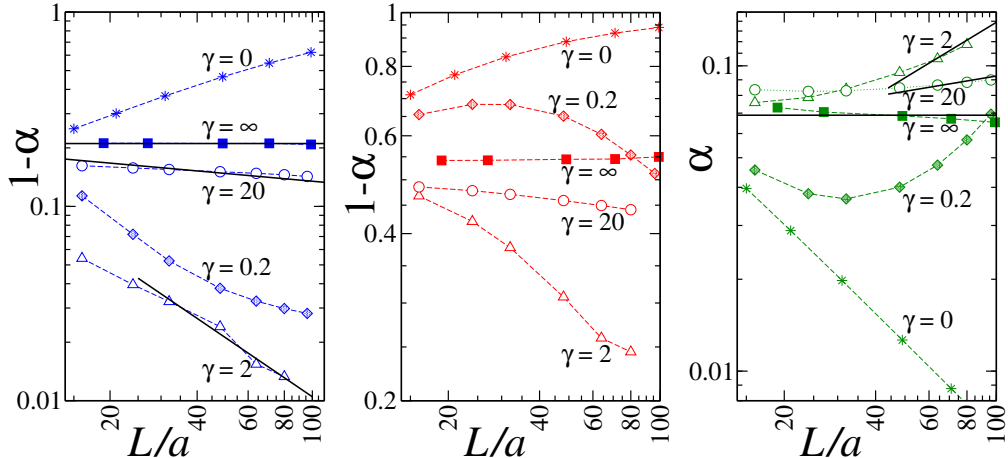


Figure 5.5: Log-Log plots of the persistent current amplitude scaling versus system size L/a , at fixed density $n = 0.25/a$ at various values of the interactions $\gamma = \infty$ (TG (■)), 20 (DMRG (○)), 2 (DMRG (△)), 0.2 (GP (◊)), 0 (NI (*)). For weak barrier strength $\Lambda = 0.1$ (blue) and 1 (red), we plot $1 - \alpha$, with faster decaying curves being more favorable for the current, while for large barrier strength $\Lambda = 10$ (green) we more conveniently show α , with reverted meaning of the scaling behavior. The solid black lines show the predictions of the LL, Eq. (5.7) for weak barrier (first panel) and (5.8) for strong barrier (third panel), with LL parameter $K|_{\gamma=\infty} = 1.00$, $K|_{\gamma=20} \simeq 1.20$ and $K|_{\gamma=2} \simeq 2.52$, as extracted from the asymptotic expansions of $K(\gamma)$ [108].

5.3. Optimal scaling of persistent currents for the AQUID

scaling strongly depends on the interaction strength. In the NI regime the scaling is unfavorable, because increasing the system size makes the current amplitude vanish even faster than nL^{-1} , the overall scaling factor encoded in the current unit I_0 . At increasing interactions, we observe instead that the scaling gets more favorable, because the decay of the current amplitude with the system size is, in part, compensated by many-body effects. In particular, we observe that there is an optimal regime, at intermediate interactions ($\gamma \simeq 2$), for which the scaling is the most favorable, in all the regimes of barrier height. In the first and third panels of Fig. 5.5 we notice that, at large enough interactions, the current amplitude obtained numerically scales as a power law, in good agreement with the Luttinger-liquid expressions (5.7) and (5.8) respectively.

The presence of an optimal regime can be understood in terms of screening of the barrier. In the semi-classical GP regime, this is determined by the healing length $\xi = \hbar/\sqrt{2mgn}$, which gets smaller and smaller while increasing the interactions. This means that the barrier gets more and more invisible to the fluid, and we can observe a gain in the scaling rate. At stronger interaction, beyond the regime of applicability of the GP equation, quantum fluctuations become crucial, especially in a 1D system, as can be understood from the LL description. Density fluctuations, which screen the barrier as well, are stronger at intermediate interactions ($K \gg 1$) and get suppressed at larger ones ($K \sim 1$), where phase fluctuations, which spoil the coherence, dominate [86, 108]. Furthermore, their contribution in either sense grows with the system size, as one can see from the expressions of U_{eff} and t_{eff} given in section 5.3.

5.4 Conclusions and Discussion

In this chapter we considered a system of bosonic atoms loaded in a ring-shaped 1D optical lattice potential, hosting a localized barrier on a given site of the lattice. For the mesoscopic rings, we demonstrated that the coherent superposition of forward and backward scattering of the particles through the barrier site, is indeed detectable through time-of-flight expansion. For fixed values of the filling parameter, the detectability of the superposition depends on the relative size between barrier and interaction strengths: the barrier makes the detectability increasing, while the interaction strength which screens the barrier, leads to the opposite phenomenon, yielding a non monotonic behavior of the detectability and averaged contrast. By increasing the filling parameter for fixed U and Λ , the screening of the barrier is enhanced, and therefore the barrier is less effective in creating the coherent superposition of flows. This regime is characterized by fermionic effects due to strong correlations. In particular, we note a good detectability of the superposition state with a simultaneous presence of density modulations along the ring. We conclude that: i) the superposition state is detectable in the momentum distribution of the bosonic gas, which is measurable via time-of-flight (TOF) expansion, and ii) the momentum distribution exhibits a subtle interplay between barrier strength and interaction.

Persistent currents are a mesoscopic phenomenon: their amplitude vanishes in the thermodynamic limit. We have studied the scaling of the persistent currents with a system size for the case of cold atoms which are confined on a ring, which hosts a localized delta-barrier. We have studied this system by combining numerical and analytical methods. We obtained the expressions for the current amplitude (in the limits of weak and strong

5.4. Conclusions and Discussion

barriers) with perturbative approach and showed that current amplitude displays power law scaling with system size. We comment, that Luttinger liquid results for the amplitude of a current are in a good agreement with DMRG simulations.

CHAPTER 6

Interacting AQUIDs and quantum gates

6.1 Introduction

In this chapter we will be dealing with coupled ring condensates. Ring shaped optical lattices, in particular, allow us to engineer textbook periodic boundary conditions in many body systems, and pave the way for exploiting the currents in the lattices as 'degrees of freedom' for new quantum devices. Aside from other applications[127], neutral currents in ring-shaped optical potentials are natural candidates to provide a realization of a Josephson junction flux qubit analog [64, 65]. This would exploit the best features of the superconducting flux qubits together with the typically low decoherence time of the cold atom based qubits. In Chapter 4 it was shown that the program can be indeed realized, constructing the qubit with bosons loaded in single ring lattice interrupted by a weak link. In this chapter, in contrast, we study two different devices.

At first, we study a specific device comprising two *homogeneous* ring-shaped potential with ring-ring coupling. This setup is introduced in Section 2.7.1. In view of the possible 'scalability' of the system, we provide a feasible way to construct a ring-ring interaction, mimicking the inductive coupling in the devices based on charged currents (like the previously men-

Chapter 6. Interacting AQUIDs and quantum gates

tioned SQUID-based devices). Indeed, in our specific setup, the coupling can be tuned with simple operations. The trapping potential is loaded with bosonic atoms, thus realizing a Bose-Hubbard ladder. We demonstrate that the imaginary-time dynamics of the phase difference across the two weakly coupled rings is controlled by double-well potential. Therefore, the system of two homogenous tunnel-coupled rings indeed defines a qubit. This is evidenced by the numerical study of the effective Hamiltonian which is obtained after integrating out the microscopic degrees of freedom(phase differences). The real time dynamics is studied within mean field two-mode Gross-Pitaevskii equations. For the analysis, we benefit from Ref. [128, 33, 34]. We demonstrate that the system is characterized by Macroscopic Quantum Self-Trapping(MQST)[129, 33, 34, 31], the atomic analog of the solid state polaronic non-linear self-localization phenomenon due to the strong electron-lattice interaction[130, 128]. In contrast to the polaron case, the nonlinearity of the Bose-Einstein condensate self trapping arises from the many-particle interactions.

Secondly, we study the experimental setup introduced in Section 2.7.2. This device can be relevant for driving qubit-qubit interactions, which is in turn important for realizing qubit gates. To achieve the goal we study the system of two coupled AQUIDs in the limit of weak interaction and we derive an effective action(which we obtain after integrating out all the phase slips except the ones over the weak links), in the limit of quantum phase model. It turns out, that one-and two- qubit gates are feasible in this regime(under an additional assumption that rings are weakly interacting) and thus the set of universal qubit gates can be implemented.

The chapter is outlined as follows. In Section 6.2, we describe how the phase differences along the wells of the two rings can be integrated out in the

6.2. Two-rings-qubit

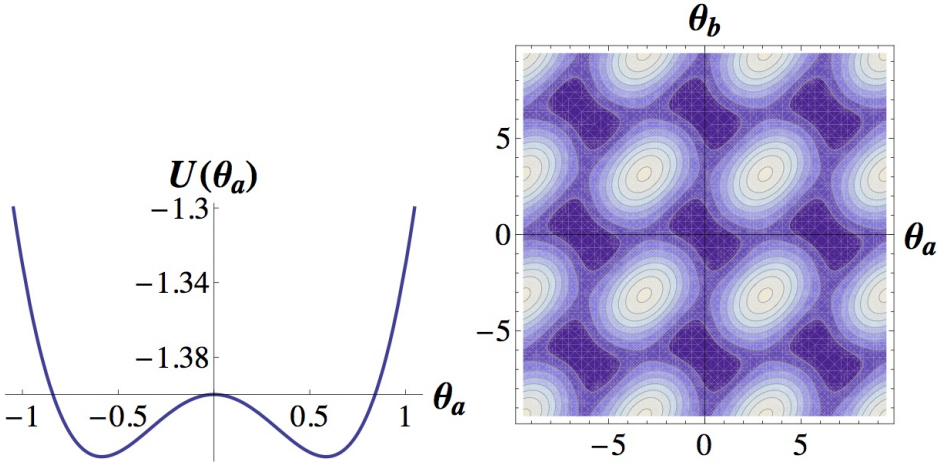


Figure 6.1: Left panel: The double well for $\theta_a = -\theta_b$. The parameters are $E'_J/E_J = 0.8$ and $\Phi_a - \Phi_b = \pi$. Right panel: The effective potential landscape.

imaginary time action, leading to an effective qubit dynamics for the phase difference across the two rings. In Section 6.3, we investigate the real-time dynamics for two coupled ring-shaped optical lattices based on two coupled Gross-Pitaevskii equations, and describe the various possible regimes. In Section 6.4, regions of oscillations with MQST and phase space diagrams are detailed for the different values of the relevant physical parameters. In Section 6.5 we elaborate in more detail how to realize qubit gates with coupled AQUID devices. Finally, we draw our conclusions in Section 6.6.

6.2 Two-rings-qubit

We consider bosonic atoms loaded in two coupled identical *homogeneous* rings as it is shown on Fig.2.13. We will prove that such a system effectively provides a qubit-dynamics (alternatively to the one-ring qubit implementation discussed above). The system is described by the Bose-Hubbard ladder and the Hamiltonian of the system is given by Eq. 3.9. We observe that along each ring the phase slips imply twisted boundary conditions and

Chapter 6. Interacting AQUIDs and quantum gates

therefore they can be localized to a specific site, say the $N - 1$ -th. As it is demonstrated in Appendix B.3, the effective action reads

$$S_{eff} = \int_0^\beta d\tau \left[\frac{1}{2U} \sum_{\alpha=a,b} \dot{\theta}_\alpha^2 + U(\theta_a, \theta_b) \right] - \frac{J}{2U(N-1)} \sum_{\alpha=a,b} \int d\tau d\tau' \theta_\alpha(\tau) G_\alpha(\tau - \tau') \theta_\alpha(\tau') \quad (6.1)$$

where each $G_\alpha(\tau)$ is given by the expression found above for the case of a single ring. In this case the phase dynamics is provided by the potential

$$U(\theta_a, \theta_b) \doteq \sum_{\alpha=a,b} \left[\frac{J}{2(N-1)} (\theta_\alpha - \Phi_\alpha)^2 - J \cos(\theta_\alpha) \right] - \tilde{J} \cos[\theta_a - \theta_b - \frac{N-2}{N}(\Phi_a - \Phi_b)] . \quad (6.2)$$

with $\tilde{J} = \langle n \rangle g$ [55]. We observe that, for large N , the potential $U(\theta_a, \theta_b)$ provides that effective phase dynamics of Josephson junctions flux qubits realized by Mooij *et al.* (large N 's corresponds to large geometrical inductance of flux qubit devices) [131]. In there, the landscape was thoroughly analysed. The qubit is made with superpositions of the two states $|\theta_1\rangle$ and $|\theta_2\rangle$ corresponding to the minima of $U(\theta_a, \theta_b)$. At the degeneracy point $\Phi_b - \Phi_a = \pi$, the effective potential takes form of a double-well, as it is demonstrated in the left panel of Fig.6.1. As it is seen from the Fig.6.2, two-level system is achieved at the frustration point. We comment that the ratio \tilde{J}/J controls the relative size of the energy barriers between minima intra- and minima inter-'unit cells' of the (θ_a, θ_b) phase space(right panel of Fig.6.1), and therefore is important for designing the qubit. In our system \tilde{J}/J can be fine tuned with the scheme shown in Fig.2.13.

6.3. Real time dynamics: Two coupled Gross-Pitaevskii equations

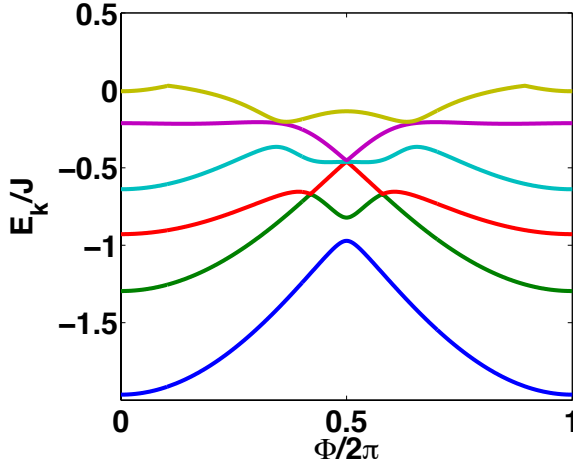


Figure 6.2: Numerically obtained first six energy levels of the Hamiltonian provided by the effective action in Eq.(6.2) as a function of $\Phi = \Phi_a - \Phi_b$. Here $U=0.5$, $\tilde{J}/J = 0.8$.

6.3 Real time dynamics: Two coupled Gross-Pitaevskii equations

Having established that the two tunnel-coupled homogeneous rings, indeed, define a two level system, in this section we study its real-time dynamics by analyzing the dynamics of the number and phase imbalance of two Bose-condensates confined in the ring shaped potential. For this goal, we assume that the system is described by a Bose-Hubbard ladder Eqs.(3.10), is in a superfluid regime, with negligible quantum fluctuations. The order parameters can be defined as the expectation values of boson operators in the Heisenberg picture:

$$\varphi_{a,i}(s) = \langle a_i(s) \rangle, \varphi_{b,i}(s) = \langle b_i(s) \rangle \quad (6.3)$$

implying that the Heisenberg equations for the operators a_i and b_i are simplified into the Gross-Pitaevskii equations for the corresponding expec-

Chapter 6. Interacting AQUIDs and quantum gates

tation values:

$$\begin{aligned} i\hbar \frac{\partial \varphi_{a,i}}{\partial s} = & -t(e^{i\Phi_a/N}\varphi_{a,i+1} + e^{-i\Phi_a/N}\varphi_{a,i-1}) \\ & + U|\varphi_{a,i}|^2\varphi_{a,i} - \mu_a\varphi_{a,i} - g\varphi_{b,i} \end{aligned} \quad (6.4)$$

$$\begin{aligned} i\hbar \frac{\partial \varphi_{b,i}}{\partial s} = & -t(e^{i\Phi_b/N}\varphi_{b,i+1} + e^{-i\Phi_b/N}\varphi_{b,i-1}) \\ & + U|\varphi_{b,i}|^2\varphi_{b,i} - \mu_b\varphi_{b,i} - g\varphi_{a,i} \end{aligned} \quad (6.5)$$

We assume that $\varphi_{a,i+1} - \varphi_{a,i} = \frac{\varphi_a(s)}{\sqrt{N}}$ and $\varphi_{b,i+1} - \varphi_{b,i} = \frac{\varphi_b(s)}{\sqrt{N}}$ for all $i, j = 0, \dots, N$, where N is a total number of ring-lattice sites. From Eqs.(6.4) and (6.5) we obtain

$$\begin{aligned} i\hbar \frac{\partial \varphi_a}{\partial s} = & -2t \cos(\Phi_a/N)\varphi_a + \frac{U}{N}|\varphi_a|^2\varphi_a \\ & - \mu_a\varphi_a - g\varphi_b \end{aligned} \quad (6.6)$$

$$\begin{aligned} i\hbar \frac{\partial \varphi_b}{\partial s} = & -2t \cos(\Phi_b/N)\varphi_b + \frac{U}{N}|\varphi_b|^2\varphi_b \\ & - \mu_b\varphi_b - g\varphi_a \end{aligned} \quad (6.7)$$

Employing the standard phase-number representation: $\varphi_{a,b} = \sqrt{N_{a,b}}e^{i\theta_{a,b}}$, two pairs of equations are obtained for imaginary and real parts:

$$\begin{aligned} \hbar \frac{\partial N_a}{\partial s} = & -2g\sqrt{N_a N_b} \sin(\theta_b - \theta_a) \\ \hbar \frac{\partial N_b}{\partial s} = & 2g\sqrt{N_a N_b} \sin(\theta_b - \theta_a) \end{aligned} \quad (6.8)$$

6.3. Real time dynamics: Two coupled Gross-Pitaevskii equations

$$\begin{aligned}\hbar \frac{\partial \theta_a}{\partial s} &= -2t \cos \Phi_a/N - \frac{UN_a}{N} + \mu_a + g \sqrt{\frac{N_b}{N_a}} \cos(\theta_b - \theta_a) \\ \hbar \frac{\partial \theta_b}{\partial s} &= -2t \cos \Phi_b/N - \frac{UN_b}{N} + \mu_b + g \sqrt{\frac{N_a}{N_b}} \cos(\theta_b - \theta_a)\end{aligned}\tag{6.9}$$

From Eqs.(6.8) it follows that $\frac{\partial N_a}{\partial s} + \frac{\partial N_b}{\partial s} = 0$, reflecting the conservation of the total bosonic number $N_T = N_a + N_b$. From equations (6.8) and (6.9) we get

$$\frac{\partial Z}{\partial \tilde{s}} = -\sqrt{1 - Z^2} \sin \Theta \tag{6.10}$$

$$\frac{\partial \Theta}{\partial \tilde{s}} = \Delta + \lambda \rho Z + \frac{Z}{\sqrt{1 - Z^2}} \cos \Theta \tag{6.11}$$

where we introduced new variables: the dimensionless time $2gs/\hbar \rightarrow \tilde{s}$, the population imbalance $Z(\tilde{s}) = (N_b - N_a)/(N_a + N_b)$ and the phase difference between the two condensates $\Theta(\tilde{s}) = \theta_a - \theta_b$. It is convenient to describe the system with a new set of parameters: an external driving force $\Delta = (2t(\cos \Phi_a/N - \cos \Phi_b/N) + \mu_b - \mu_a)/2g$, the effective scattering wavelength $\lambda = U/2g$ and the total bosonic density $\rho = N_T/N$. The exact solutions of Eqs.(6.10) and (6.11) in terms of elliptic functions[33] can be adapted to our case and it is detailed in the Appendix B.4. As it has been noticed in [33] that equations can be derived as Hamilton equations with

$$H(Z(\tilde{s}), \Theta(\tilde{s})) = \frac{\lambda \rho Z^2}{2} + \Delta Z - \sqrt{1 - Z^2} \cos \Theta, \tag{6.12}$$

by considering Z and Θ as conjugate variables. Since the energy of the system is conserved, $H(Z(\tilde{s}), \Theta(\tilde{s})) = H(Z(0), \Theta(0)) = H_0$.

The dynamics can be visualized with the help of the mechanical system provided by a rotator of length of $\sqrt{1 - Z^2}$ driven by the external force Δ . In this picture, Z is considered to be an angular momentum of the

rotator and $\lambda\rho$ its moment of inertia. For $\Delta = 0$, the dynamics of the rotator depends on the value of initial angular momentum $Z(0)$. For small initial kinetic energy $\frac{\lambda\rho Z(0)^2}{2}$, the rotator makes small oscillations and its trajectory is an open curve, thus $\langle Z \rangle = 0$. For the critical value Z_c the rotator reaches the equilibrium vertical position corresponding to $\phi = \pi$. For $Z_0 > Z_c$ the rotator performs revolutions around the fixed point with $\Delta\theta = 2\pi$ and $\langle Z \rangle = 0$. In the case of non vanishing Δ , the dynamics of the rotator depends on $Z(0)$ and the external force Δ . Because of Δ , the system oscillates around a shifted equilibrium value (which leads to an asymmetry in the system) and $\langle Z \rangle \neq 0$ for all the cases.

Below, we discuss the different regimes for population imbalance emerging from Eqs.(6.10) and (6.11) depending on the values of parameters $\lambda\rho$ and Z_0 (see Appendix B.4 for technical details). For each physical regime we further discuss the solution for both cases of vanishing and non vanishing Δ .

6.3.1 Population imbalance and oscillation frequencies in the limit $\lambda\rho = 0$

I-A $\Delta = 0$. – For noninteracting atoms, the solution of Eqs.(6.10) and (6.11) is

$$Z(\tilde{s}) = \sqrt{1 - H_0^2} \sin(\tilde{s} + \tilde{s}_0) \quad (6.13)$$

where $\tilde{s}_0 = \arcsin \frac{Z_0}{\sqrt{1-H_0^2}}$ and $H_0 = -\sqrt{1-Z_0^2} \cos \Theta_0$ is an initial energy of the system. Eq.(6.13) describes sinusoidal Rabi oscillations between the two traps with frequency $\omega_0 = 2g$. These oscillations are equivalent to single atom dynamics, rather than a Josephson-effect arising from the interacting superfluid condensate.

II-A $\Delta \neq 0$. – Depending on the value of the determinant $D = 1 -$

6.3. Real time dynamics: Two coupled Gross-Pitaevskii equations

$H_0^2/(\Delta^2 + 1)$ of the equation $f(Z) = -(\Delta^2 + 1)Z^2 + 2H_0\Delta Z + 1 - H_0^2$, the population imbalance is either oscillating around a non-zero average, reflecting the MQST phenomenon, or staying constant in time. A numerical analysis shows that $D \geq 0$. Therefore, there are two different sub-cases. When $D = 0$ (which can be satisfied only if $\sin \Theta_0 = 0$), the population imbalance stays constant and takes on the value

$$Z = Z_0 = -\frac{\Delta}{\sqrt{1 + \Delta^2}} = \text{const} \quad (6.14)$$

For this value of the initial population imbalance, $\Theta = \text{const}$. In the case when $D > 0$, the subsequent expression for $Z(t)$ is obtained:

$$Z(\tilde{s}) = B - \frac{C}{A} \sin [a(\tilde{s} - \tilde{s}_0)], \quad (6.15)$$

where $\tilde{s}_0 = \frac{1}{A} \arcsin [\frac{A}{C}(Z_0 - B)]$, $A = \sqrt{1 + \Delta^2}$, $B = \frac{\Delta H_0}{A^2}$ and $C = \sqrt{1 - \frac{H_0^2}{A^2}}$. As it is seen from Eq.(6.15), the system is oscillating about a non-zero average value B with frequency

$$\omega = \omega_0 \sqrt{1 + \Delta^2} \quad (6.16)$$

All the regimes discussed for this case are displayed in Fig.6.3.

6.3.2 Population imbalance and oscillation frequencies in the limit $\lambda\rho \ll 1$

I-B $\Delta = 0$.– The qualitative behavior of the dynamics for this subcase depends on the elliptic modulus k which is given by Eq.(B.40). For $\lambda\rho \ll 1$

$$k = Z(0)\lambda\rho\left(1 - \frac{\lambda\rho}{2}\sqrt{1 - Z(0)^2}\right) \quad (6.17)$$

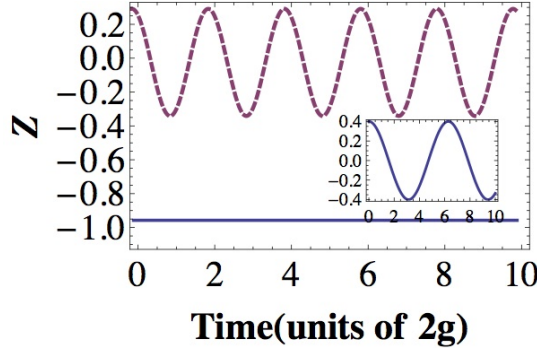


Figure 6.3: (Color online). The population imbalance in two coupled rings for the case $\lambda\rho = 0$. Solid and dashed lines correspond to the cases $D = 0$ and $D > 0$ accordingly in the regime of non-zero Δ . An inset shows behavior of $Z(\tilde{s})$ for vanishing Δ . Here $\lambda\rho = 0$, $\Delta = 2$, $\Theta_0 = 0$ implying that $\omega \simeq 3.16\omega_0$.

So $k \sim 0$ and therefore $Z(t)$ displays only one regime given by:

$$\begin{aligned} Z(\tilde{s}) &\simeq Z(0)(\cos \omega(\tilde{s} - \tilde{s}_0)) \\ &+ \frac{k}{4}(\omega(\tilde{s} - \tilde{s}_0) - \sin 2\omega(\tilde{s} - \tilde{s}_0)) \sin \omega(\tilde{s} - \tilde{s}_0) \end{aligned} \quad (6.18)$$

where $\omega \simeq 2g(1 + \frac{\lambda}{2}\rho\sqrt{1 - Z(0)^2})$ and \tilde{s}_0 fixes the initial condition. Therefore, in this regime the population imbalance is characterized by almost sinusoidal oscillations about zero average— see the inset of Fig.6.4.

II-B $\Delta \neq 0$.— In this case behavior of $Z(t)$ is governed by determinant δ of the cubic equation Eq.(B.47). There are two different regimes depending on the initial value of the population imbalance which are given by the value of δ . All the regimes can be discussed by expressing the Weierstrass function in Eq.(B.43) using Jacobian elliptic functions. In the limit of $\delta = 0$, the population imbalance takes form

$$Z(\tilde{s}) = Z(0) + \frac{f'[Z(0)]/4}{-c + 3c[\sin(-\sqrt{3c}\frac{\lambda\rho}{2}\tilde{s})]^{-2} - f''[Z(0)]/24} \quad (6.19)$$

6.3. Real time dynamics: Two coupled Gross-Pitaevskii equations

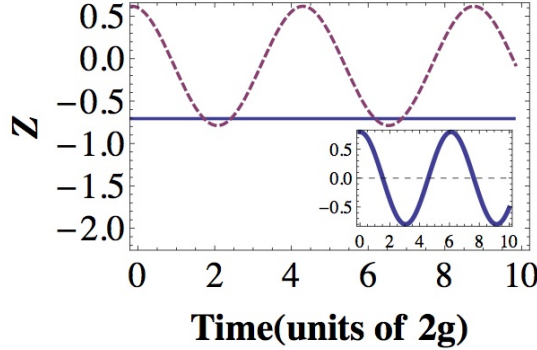


Figure 6.4: The population imbalance in two coupled rings for the case $\lambda\rho \ll 1$. Solid and dashed lines correspond to the cases $\delta = 0$ and $\delta < 0$ accordingly in the regime of non-zero Δ . An inset shows behavior of $Z(\tilde{s})$ for the vanishing Δ . Here $\lambda\rho = 0.1$, $\Theta_0 = 0$ and $\Delta = 1$.

For the parameters discussed here, $f'[Z(0)] \sim 10^{-14}$; so the population imbalance stays constant for the same reason as for the subcase $D = 0$ of the previous section. In the limit of $\delta < 0$, the population imbalance takes the form

$$Z(\tilde{s}) = Z(0) + \frac{f'[Z(0)]/4}{e_2 + H_2 \frac{1+\cos(\lambda\rho\sqrt{H_2}\tilde{s})}{1-\cos(\lambda\rho\sqrt{H_2}\tilde{s})} - f''[Z(0)]/24} \quad (6.20)$$

where e_2, H_2 are defined in the Appendix B.4. Eq.(6.20) is correct when $1/2 - 3e_2/4H_2 \simeq 0$ (for the parameters considered in the article $m \simeq 10^{-7}$). As one can see from this formula, the population imbalance is oscillating about non-zero average (MQST regime) with frequency given by

$$\omega = 2g \left(\sqrt{1 + \Delta^2} + \frac{(Z(0)\Delta - \sqrt{1 - Z(0)^2})(2\Delta^2 - 1)}{2(1 + \Delta^2)^{3/2}} \lambda\rho \right) \quad (6.21)$$

This two regimes are shown in Fig.6.4.

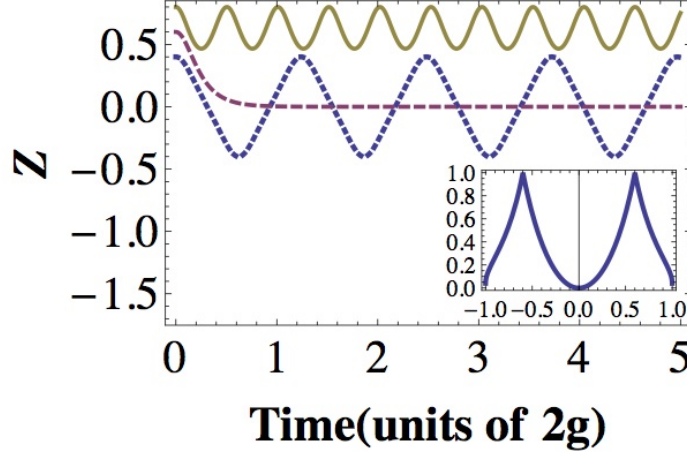


Figure 6.5: The population imbalance in two coupled rings for the intermediate value of $\lambda\rho$ and $\Delta = 0$. Dotted line,dashed line and solid line respectively correspond to the cases $k < 1$, $k = 1$, $k > 1$. Inset shows dependence of the elliptic modulus \tilde{k} ($\tilde{k} = k$, for $k < 1$; 1 for $k = 1$ and $1/k$, for $k > 1$) from the value of Z_0 . Here $\lambda\rho = 10$, $\Theta_0 = 0$.

6.3.3 Population imbalance and oscillation frequencies for the intermediate values of $\lambda\rho$

I-C $\Delta = 0$ – The population imbalance can be expressed in terms of Jacobi functions 'cn' and 'dn' (Eq.(B.39)) and behavior of the solutions (which is summarized on Fig.6.5) is governed by elliptic modulus k (Eq.(B.40)).

II-C $\Delta \neq 0$ – The population imbalance can be written in terms of Weierstrass elliptic function (Eq.(B.43)). The behavior of the solutions is governed by the determinant δ (Eq.(B.47)) of the characteristic cubic equation. The dynamics for this subcase is given by Fig.6.6. In both cases oscillation periods can be expressed in terms of elliptic integral of the first kind (Eqs.(B.42) and (B.52)). When $\delta = 0$ oscillations are exponentially suppressed or there are sinusoidal oscillations depending on the relative sign between $g2$ and $g3$ (Eqs.(B.48) and (B.49)). Because it is possible to express the Weierstrass function through Jacobian functions 'sn' and 'cn' (Eqs.(B.50) and (B.51)) we conclude that in general the population

6.3. Real time dynamics: Two coupled Gross-Pitaevskii equations

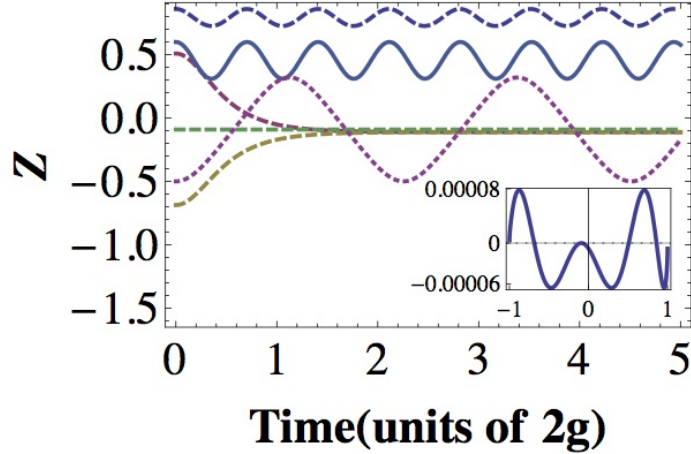


Figure 6.6: The population imbalance in two coupled rings for the intermediate value of $\lambda\rho$ and $\Delta = 1$. Dotted line, dashed line and solid line respectively correspond to the cases $\delta < 0, \delta = 0, \delta > 0$. Inset shows dependence of determinant δ of characteristic cubic equation from the value of Z_0 . Here $\lambda\rho = 10, \Theta_0 = 0$

imbalance can be written in terms of Jacobian functions.

6.3.4 Population imbalance and oscillation frequencies for $\lambda\rho \rightarrow \infty$

In analogy to a non-rigid pendulum, it is expected that in this regime, no oscillations occur and the population imbalance stays constant: the parameter $\lambda\rho$ is playing the role of the moment of inertia and when it is very big it is not possible to force the pendulum to rotate by providing it with finite amount of angular momentum (which is Z_0) or by acting on it with finite driving force Δ . It is also possible to arrive at this conclusion from the analytical solutions shown in Appendix B.4.

I-D $\Delta = 0-$ We see that $k \rightarrow \infty$ and $Z(\tilde{s}) = Cdn[(C\lambda\rho/k(\tilde{s} - \tilde{s}_0), 0) = Z_0 = const]$.

II-D $\Delta \neq 0-$ In this case $\delta = 0$ and the solution is given by Eq.(B.49).

But because in this limit $f'(Z_1) \rightarrow 0$ and $Z_1 = Z_0$ we conclude that $Z(\tilde{s}) = Z_0 = \text{const.}$

6.4 MQST and phase space diagrams

In this section, it is shown how it is possible to find the values of the population imbalance which takes the system and the regions of MQST depending on Z_0 . The phase diagrams in $\Theta/\pi, Z(\tilde{s})$ space for the cases of zero and non-zero values of the Δ are introduced as well.

As it is seen from Eq.(B.37), if the characteristic quartic equation (which is given by Eq.(B.38)) $f(Z) < 0$, then the time takes imaginary values. So we conclude that allowed regions of $Z(\tilde{s})$ are given by the condition

$$f(Z) \geq 0, \quad (6.22)$$

Eq.(B.36), derived from the Gross-Pitaevskii Eqs.(6.10) and (6.11), can be written as an equation of motion of a classical particle with a coordinate Z , potential energy $U(Z)$ and total energy E :

$$\dot{Z}^2(\tilde{s}) + U(Z) = E, \quad (6.23)$$

where the first term is playing the role of kinetic energy. The second term and the total energy are given by:

$$\begin{aligned} U(Z) &= Z^2 \left(\frac{(\lambda\rho)^2 Z^2}{4} + 1 + \Delta^2 - H_0\lambda\rho \right) + Z(\lambda\rho\Delta Z^2 - 2H_0\Delta) \\ E &= \dot{Z}^2(0) + U(Z(0)) = 1 - H_0^2 \end{aligned} \quad (6.24)$$

Within the classical mechanics analogy, $f(Z)$ plays the role of $E - U$. The motion of the particle lies within the regions of the classical turning points

6.4. MQST and phase space diagrams

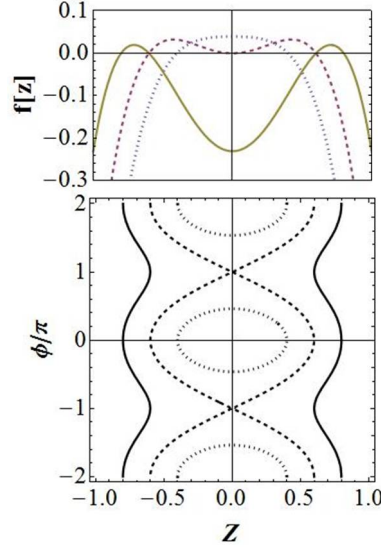


Figure 6.7: Dependence of the characteristic function $f(Z)$ on population imbalance (top) and phase space diagram (bottom) for the case $\Delta = 0$. Oscillations can occur only in the regions where $f(Z) \geq 0$. Dotted, dashed and solid lines respectively correspond to the values $Z_0 = 0.4, 0.6, 0.8$ (for these values $k < 1$, $k = 1$ and $k > 1$ respectively). Here $\Theta_0 = 0$ and $\lambda\rho = 10$.

in which the total energy equals the potential energy. So Eq.(6.22) has a simple physical meaning: that a classical particle can only move in the regions where total energy is equal or bigger than potential energy. From the upper graphs of the Figs.6.7 and 6.8, one can see that when all values of parameters are fixed, and we start to change the value of Z_0 then the function $f(Z)$ changes from parabolic to double-well. When $\Delta = 0$ then for the parabolic potential, $Z(\tilde{s})$ oscillates about an average of zero value, and when $Z(0) > Z_c$ ($Z_c = 0.6$ in our case), the particle is forced to oscillate about a non-zero average in one of the two wells as it is seen from Fig.6.7 which is evidence of the MQST. Indeed such phenomenon occurs in the system for $Z(0) > Z_c$, where

$$Z_c = \pm \sqrt{\frac{2}{\lambda\rho} - \frac{1 + \cos 2\Theta_0}{(\lambda\rho)^2} + \frac{(1 + \cos 2\Theta_0)(\cos 2\Theta_0 + 2(\lambda\rho - 1)^2 - 1)}{(\lambda\rho)^2}} \quad (6.25)$$

which reduces to

$$Z_c = \pm 2 \frac{\sqrt{\lambda\rho - 1}}{\lambda\rho} \quad (6.26)$$

for $\sin \Theta_0 = 0$. For $Z_0 = Z_c$, the particle moves from Z_0 to the point $Z = 0$ where it stays for an infinite time because at this point $f'(Z) = 0$ which means there is no force acting on the particle($U'(Z) = 0$).

When $\Delta \neq 0$, all the regimes are the same but with the difference that the external force Δ breaks the symmetry at the point $Z = 0$, with the following two consequences: (1): $Z(\tilde{s})$ is always oscillating about a non-zero average, and (2): for the critical value Z_c , the oscillations damp to the non-zero value of population imbalance, as one can see from Fig.6.8. So for all values of Z_0 (except the values for which $\delta = 0$) the effect of MQST occurs in the system. The lower graphs of Figs.6.7 and 6.8 display corresponding phase versus population imbalance. After expressing the phase using the population imbalance from Eq.(6.12), we get

$$\Theta = \arccos \left[\frac{H_0 - \frac{\lambda\rho Z^2}{2} - \Delta Z}{\sqrt{1 - Z^2}} \right] \quad (6.27)$$

From Fig.6.7 it is seen that when $Z < Z_c$, the phase diagram is a closed curve and the phase is oscillating about zero average value. At the critical point, the phase diagram starts to split into the two open curves and for $Z > Z_c$ it consists of two open curves and the phase takes any value in the interval $[-\infty, \infty]$. In the case when $\Delta \neq 0$ the phase diagram is changing depending on Z_0 in a similar way but with the difference that

6.5. Demonstration of the one- and two- qubit unitary gates

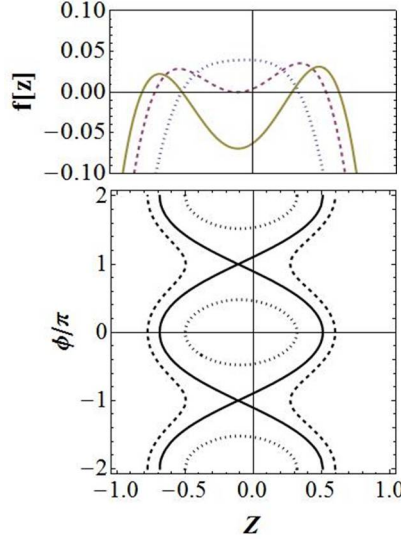


Figure 6.8: Dependence of the characteristic function $f(Z)$ on population imbalance (top) and phase space diagram (bottom) for the case $\Delta \neq 0$. Oscillations can occur only in the regions where $f(Z) \geq 0$. Dotted, dashed and solid lines respectively correspond to the values $Z_0 = -0.5, 0.509117, 0.6$ (for these values $\delta < 0, \delta = 0$ and $\delta > 0$ respectively). Here $\Theta_0 = 0$ and $\lambda\rho = 10$.

the external force Δ is breaking the symmetry about the origin of Z axis as demonstrated in Fig.6.8.

6.5 Demonstration of the one- and two- qubit unitary gates

The aim of this section is to show how the effective phase dynamics of optical ring-lattices with impurities allows the construction of one- and two-qubit gates - a necessity for a universal quantum computation. Here, we adapt results which were obtained by Solenov and Mozyrsky[132] for the case of homogeneous rings with impurities.

6.5.1 Single qubit gates

For the realization of single-qubit rotations, we consider the qubit system in the quantum phase limit(see Section 4.2.1) close to the symmetric double well configuration $\Phi \simeq \pi$. In the basis of the two level system discussed before, the Hamiltonian takes the form:

$$H \simeq \varepsilon \sigma_z + \frac{\Phi - \pi}{\delta} \langle \theta \rangle_{01} \sigma_x, \quad (6.28)$$

where $\langle \theta \rangle_{01}$ is the off-diagonal element of the phase-slip in the two-level system basis. It is easy to show that spin flip, Hadamard and phase gates can be realized by this Hamiltonian. For example, a phase gate can be realized by evolving the state through the unitary transformation $U_z(\beta)$ (tuning the second term of Eq.(6.28) to zero by adjusting the imprinted flux)

$$U_z(\beta) = \exp(i\varepsilon\tau\sigma_z) = \begin{pmatrix} e^{i\varepsilon\tau} & 0 \\ 0 & e^{-i\varepsilon\tau} \end{pmatrix}. \quad (6.29)$$

After tuning the gap energy close to zero (adjusting the barrier height of the impurity), we can realize the following rotation

$$U_x(\beta) = \exp(i\alpha\tau\sigma_x) = \begin{pmatrix} \cos \alpha & i \sin \alpha \\ i \sin \alpha & \cos \alpha \end{pmatrix} \quad (6.30)$$

where $\alpha = \frac{\Phi - \pi}{\delta} \langle \theta \rangle_{01} \tau$. When $\alpha = \pi/2$ and $\alpha = \pi/4$ the NOT and Hadamard gates are respectively realized. It is important to notice that one qubit rotations around z and x axis are enough to implement any single qubit rotations [133].

6.5. Demonstration of the one- and two-qubit unitary gates

6.5.2 Two-qubit coupling and gates

The effective dynamics for two coupled qubits, each realized as a single ring with a localized impurity (as in Fig.2.15), in the limit of the quantum phase model is governed by the Lagrangian (the derivation is very similar to the effective dynamics of double-ring setup introduced in Appendix B.3):

$$\begin{aligned} L = & \sum_{\alpha=a,b} \frac{1}{2U} \dot{\theta}_\alpha^2 + \left[\frac{J}{2(N-1)} (\theta_\alpha - \Phi_\alpha)^2 - J' \cos(\theta_\alpha) \right] \\ & - \tilde{J}'' \cos[\theta_a - \theta_b - \frac{N-2}{N}(\Phi_a - \Phi_b)] \end{aligned} \quad (6.31)$$

Where J'' is the Josephson tunnelling energy between the two rings. When $\Phi_a = \Phi_b = \Phi$ and $J'' \ll J'$ the last term reduces to $-J'' \frac{(\theta_a - \theta_b)^2}{2}$ and the Lagrangian takes the form

$$\begin{aligned} L = & J' \left[\sum_{\alpha=a,b} \frac{1}{2J'U} \dot{\theta}_\alpha^2 + \left[\frac{J}{2J'(N-1)} (\theta_\alpha - \Phi_\alpha)^2 - \cos(\theta_\alpha) \right] \right. \\ & \left. + \frac{J''}{J'} \frac{(\theta_a - \theta_b)^2}{2} \right]. \end{aligned} \quad (6.32)$$

By applying the same procedure as in the previous section, we obtain the following Hamiltonian in the eigen-basis of the two-level systems of rings a and b

$$H = H_a + H_b + \frac{J''}{J'} \sigma_x^1 \sigma_x^2 \langle \theta \rangle_{01}^2, \quad (6.33)$$

$$H_\alpha = \varepsilon \sigma_z^\alpha + \left(\frac{\Phi - \pi}{\delta} + \frac{J'' \pi}{J'} \right) \langle \theta \rangle_{01} \sigma_x^\alpha. \quad (6.34)$$

From these equations it follows that qubit-qubit interactions can be realized using our set-up. If we choose the tuning $\varepsilon \rightarrow 0$ and $\Phi \rightarrow \pi - \frac{\delta J'' \pi}{J'}$ the

Chapter 6. Interacting AQUIDs and quantum gates

natural representation of a $(SWAP)^\alpha$ gate[134] can be obtained:

$$U(\tau) = \exp\left[-i\frac{J''}{J'}\sigma_x^1\sigma_x^2\tau\right], \quad (6.35)$$

where $\alpha = \frac{\tau J''}{J'}$. We comment that $\sigma_x^1\sigma_x^2$ is a two-qubit entangling gate. As it is shown in Ref. [133], any two-qubit entangling gate combined with arbitrary single-qubit rotations realizes a set of universal quantum gates.

It is instructive to make rough estimates for one- and two-qubit gate times to get an idea about the qubit quality factor(which is a number of single qubit rotations that can be implemented before the qubit decoheres). As it was estimated at the end of Section 4, the tunneling matrix element $J \simeq 500Hz$ and the typical energy scale for the qubit gap $\nu_{01} \simeq 100Hz$. Taking a tenth of a lifetime of the persistent current(τ) as a rough estimate for the qubit decoherence time(T) we have $T = 0.1\tau \simeq 10sec$. These set of parameters yield the following estimates for the one-(T_1) and two qubit(T_2) gates times and for the quality factor(Q): $T_1 = \pi/0.1J \simeq 100ms$, $T_2 = \pi/\nu_{01} \simeq 10ms$ and $Q = \pi\nu_{01}T \simeq 10^3$. It is also interesting to compare our quality factor with the quality factor of current solid state devices which is of the order of 10^6 . This comparison shows that superconducting Josephson junction devices are better (by a factor of 10^3) for implementing quantum computation tasks, however AQUID devices have much longer(by a factor of 10^5) coherence times which makes them suitable as long time memory devices.

6.6 Conclusions

In this chapter, we studied the experimental setup, provided in Fig.2.13, which allows us to tune the tunneling in an experimentally feasible way.

6.6. Conclusions

The system is governed by a Bose-Hubbard two-leg ladder Hamiltonian, pierced by a synthetic magnetic field, effectively twisting the boundary conditions of the two rings. In the weak ring-ring coupling regime, the microscopic degrees of freedom (the phase slips between adjacent wells along the rings) are integrated out, leading to an effective action of a two-level system for the ring-ring phase slip. This implies that such a physical system provides indeed a qubit, analogous to the specific flux qubit built with superconductor Josephson junctions [64].

The real time evolution of population imbalance and phase difference between the two flowing condensates has been analyzed via two coupled Gross-Pitaevskii equations obtained from the Bose-Hubbard ladder in the mean-field equations. The dynamics has been thoroughly analyzed in the different regimes depending on the values of the *s*-wave scattering, tunneling rate, synthetic 'magnetic fluxes' and initial population imbalances ($\lambda\rho,g,\Delta$ and Z_0 respectively). It is clear from our analysis how the macroscopic quantum self trapping occurs in our system. Moreover, it is shown that population imbalance takes values only in classically allowed regions of oscillation. It would be relevant to describe our system including the quantum fluctuations around the mean field solution[135, 136].

We also considered an actual implementation of the AQUID devices for quantum computation. To this end, we demonstrate that one- and two-qubit gates can be implemented in the limit of quantum phase model. We demonstrate that in this limit for the case of weak interaction between the rings a $\sigma_x^1\sigma_x^2$ two qubit gate is achieved. This gate combined with single qubit rotations gives a universal set of gates for a quantum computation. We note, that one- and two-qubit gates can be realized with our quantum device by tuning the barrier height, interaction strength, and the

Chapter 6. Interacting AQUIDs and quantum gates

intensity of the laser suitably.

CHAPTER 7

Conclusions and Outlook

In this thesis, we have studied rf-SQUIDs constructed with neutral atomic currents flowing in ring-shaped optical lattice potentials interrupted by a single weak link: the Atomtronics Quantum Interference Device (AQUID). The effective quantum dynamics of the system is proved to be that one of a two-level system. We studied the characterization of the qubit by analyzing the scaling properties (both with the number of particles and system size) of the energy gap between the many-body ground and excited states. Our results indicate that the qubit is well resolved (in energy) for small and mesoscopic rings. The spatial scale of the rings radii would be in the range of 5 to 20 microns. The ring-ring interaction can be realized with the device described in Chapter 2. We study the dynamics of the physical system of two Bose-Einstein condensates, flowing in ring-shaped optical potentials, and mutually interacting through tunnel coupling. For such a ladder system we performed a thorough analysis of the real time dynamics in different parameters regimes.

Clearly, such systems may be relevant for quantum computation purposes. Accordingly, the AQUID would be the elementary “transistor”, the qubit. The set-up we devised (in Chapter 2) can be exploited to create two-qubit gates (see Chapter 6). The initialization of our qubit can be accomplished, for example, by imparting rotation through light-induced torque from Laguerre-Gauss (LG) beams carrying an optical angular mo-

Chapter 7. Conclusions and Outlook

mentum. Stacks of $n \sim 10$ homogeneous ring lattices with tunable distance and stacks of AQUIDs have been realized experimentally (in the lab coordinated by R. Dumke) with Spatial Light Modulators (SLM). Such configurations are realized by making use of the cylindrical symmetry of Laguerre-Gaussian beams and exploiting the flexibility (in terms of generating light fields of different spatial shapes) provided by the SLM devices. Stack of qubits can be realized following very similar protocols.

Indeed, similar goals were carried out by realizing the AQUID with homogeneous condensates (i.e. without lattice modulation). We remark that the lattice confinement brings important added values with respect to that realization. First of all, the gap between the two levels of the qubit displays a more feasible dependence with the number of atoms in the system compared with the case of homogeneous rings with a delta barrier. This is ultimately due to the fact that the barrier can be localized on a lattice spacing spatial scale; thereby the k-mixing—that is the key feature to have a well defined two level system—is not suppressed (as, in contrast, happens for homogeneous condensates with a realistic barrier [58]). Our scaling analysis allows us to identify the mesoscopic regime as the most suited for the realization of the AQUID(see Fig. 5.5). As a second positive feature, the lattice provides a platform for qubit-qubit interaction. These two features, we believe, could ultimately facilitate the exploitation of the device in future atomtronic integrated circuits.

We studied possible readout through absorption image techniques. Particular attention has been devoted to macroscopic superposition of circulation states. For our mesoscopic AQUID, we demonstrated that the coherent superposition of forward and backward scattering of the particles through the barrier site, is indeed detectable through the time-of-flight expansion.

This is strong a posteriori evidence that the effective physics of a two-level-system is encoded into the system. Our study indicates that the qubit dynamics is detectable for a wide range of system parameters. We have identified the ratio local- interaction /depth-of-the-weak-link, U/Λ , as an important parameter for the study of the behavior of the qubit both in terms of its definition with respect to the rest of the many-body spectrum (the qubit turns out to be best defined below the critical line in Fig. 4.5(e)) and its detectability in TOF images (the contrast is found to be best defined around or above the same critical line).

We have also studied the scaling of the persistent currents with system size for the case of one-dimensional interacting bosons which are confined in a ring which contains a localized barrier modeled as a delta function. We have found that the scaling depends on the interaction strength, and that the persistent current amplitude decreases slower at intermediate interactions than at very large or very small ones. This non-monotonic effect is due to the combination of the effects of interaction and quantum fluctuations. Our result is important in view of the forthcoming experimental realizations, where the best regime for observing the largest possible current signal should be found from the trade-off between realizable small system size and interaction strength.

Decoherence, of course, is an important issue for our proposal that remains to be studied. We comment, however, that measurements of the decay dynamics of a rotating condensate in an optical ring trap show that the quantized flow states have remarkably long lifetimes, of the order of tens of seconds even for high angular momentum ($l = 10$) [20]. Phase slips (the dominant mechanism of decoherence), condensate fragmentation and collective excitations which would ultimately destroy the topologically

Chapter 7. Conclusions and Outlook

protected quantum state are found to be strongly suppressed below a critical flow velocity. Although atom loss in the rotating condensate does not destroy the state, it can lead to a slow decrease in the robustness of the superfluid where the occurrence of phase slips becomes more likely [74, 137]. We believe that the decoherence rates could be controlled within the current experimental know- how of the field.

The Atomtronics' positive trend crucially relies on the recent progress achieved in the optics microfabrication field. Thereby, central issues, of the cold atoms system, like scalability, reconfigurability, and stability can be feasibly addressed. In many current and envisaged investigations, there is a need to push for further miniaturization of the circuits. The current lower limit is generically imposed by the diffraction limit of the employed optics. Going to the sub-micron, although challenging, might be accessible in the near future. At this spatial scales, mesoscopic quantum effects could be traced out. The scalability of multiple-ring structures will be certainly fostered by tailoring optical potentials beyond the Laguerre-Gauss type (f.i. employing Bessel-Gauss laser beams).

A central issue for Atomtronics integrated circuits, is the minimization of the operating time on the circuit and the communication among different circuital parts (i.e. AQUID-AQUID communication). Currently, typical time rates are in the millisecond range, but a thorough analysis of the parameters controlling time rates is still missing.

Bibliography

- [1] Jonathan P Dowling and Gerard J Milburn. Quantum technology: the second quantum revolution. *Philosophical Transactions of the Royal Society of London. Series A: Mathematical, Physical and Engineering Sciences*, 361(1809):1655–1674, 2003.
- [2] Immanuel Bloch. Quantum coherence and entanglement with ultracold atoms in optical lattices. *Nature*, 453(7198):1016–1022, 2008.
- [3] Immanuel Bloch, Jean Dalibard, and Wilhelm Zwerger. Many-body physics with ultracold gases. *Reviews of Modern Physics*, 80(3):885, 2008.
- [4] Maciej Lewenstein, Anna Sanpera, Veronica Ahufinger, Bogdan Damski, Aditi Sen, and Ujjwal Sen. Ultracold atomic gases in optical lattices: mimicking condensed matter physics and beyond. *Advances in Physics*, 56(2):243–379, 2007.
- [5] Maciej Lewenstein, Anna Sanpera, and Verònica Ahufinger. *Ultracold Atoms in Optical Lattices: Simulating quantum many-body systems*. Oxford University Press, 2012.
- [6] Richard Phillips Feynman and Albert Roach Hibbs. *Quantum mechanics and path integrals*. McGraw-Hill, 1965.
- [7] BT Seaman, M Krämer, DZ Anderson, and MJ Holland. Atomtronics: Ultracold-atom analogs of electronic devices. *Physical Review A*, 75(2):023615, 2007.
- [8] Albert Benseny, Sonia Fernández-Vidal, Joan Bagudà, Ramón Corbalán, Antonio Picón, Luis Roso, Gerhard Birkl, and Jordi Mompart. Atomtronics with holes: coherent transport of an empty site in a triple-well potential. *Physical Review A*, 82(1):013604, 2010.
- [9] R Dumke, M Volk, T Müther, FBJ Buchkremer, G Birkl, and W Ertmer. Micro-optical realization of arrays of selectively addressable dipole traps: a scalable configuration for quantum computation with atomic qubits. *Physical review letters*, 89(9):097903, 2002.
- [10] G Birkl, FBJ Buchkremer, R Dumke, and W Ertmer. Atom optics with microfabricated optical elements. *Optics Communications*, 191(1):67–81, 2001.
- [11] Malte Schlosser, Sascha Tichelmann, Jens Kruse, and Gerhard Birkl. Scalable architecture for quantum information processing with atoms in optical micro-structures. *Quantum Information Processing*, 10(6):907–924, 2011.
- [12] G Birkl, FBJ Buchkremer, R Dumke, and W Ertmer. Atom optics with microfabricated optical elements. *Optics Communications*, 191(1):67–81, 2001.

Bibliography

- [13] RA Pepino, J Cooper, DZ Anderson, and MJ Holland. Atomtronic circuits of diodes and transistors. *Physical review letters*, 103(14):140405, 2009.
- [14] KC Wright, RB Blakestad, CJ Lobb, WD Phillips, and GK Campbell. Driving phase slips in a superfluid atom circuit with a rotating weak link. *Physical review letters*, 110(2):025302, 2013.
- [15] Jean-Philippe Brantut, Charles Grenier, Jakob Meineke, David Stadler, Sebastian Krinner, Corinna Kollath, Tilman Esslinger, and Antoine Georges. A thermoelectric heat engine with ultracold atoms. *Science*, 342(6159):713–715, 2013.
- [16] BE Sherlock, M Gildemeister, E Owen, E Nugent, and CJ Foot. Time-averaged adiabatic ring potential for ultracold atoms. *Physical Review A*, 83(4):043408, 2011.
- [17] Kevin Henderson, Changhyun Ryu, Calum MacCormick, and MG Boshier. Experimental demonstration of painting arbitrary and dynamic potentials for bose-einstein condensates. *New Journal of Physics*, 11(4):043030, 2009.
- [18] A Ramanathan, KC Wright, SR Muniz, M Zelan, WT Hill III, CJ Lobb, Kristian Helmerson, WD Phillips, and GK Campbell. Superflow in a toroidal bose-einstein condensate: an atom circuit with a tunable weak link. *Physical review letters*, 106(13):130401, 2011.
- [19] Stephen Eckel, Jeffrey G Lee, Fred Jendrzejewski, Noel Murray, Charles W Clark, Christopher J Lobb, William D Phillips, Mark Edwards, and Gretchen K Campbell. Hysteresis in a quantized superfluid/atomtronic/’circuit. *Nature*, 506(7487):200–203, 2014.
- [20] Stuart Moulder, Scott Beattie, Robert P Smith, Naaman Tammuz, and Zoran Hadzibabic. Quantized supercurrent decay in an annular bose-einstein condensate. *Physical Review A*, 86(1):013629, 2012.
- [21] Michael Tinkham. *Introduction to superconductivity*. Courier Dover Publications, 2012.
- [22] John Clarke and Alex I Braginski. *The SQUID handbook*. Wiley Online Library, 2006.
- [23] Rosario Fazio and Herre Van Der Zant. Quantum phase transitions and vortex dynamics in superconducting networks. *Physics Reports*, 355(4):235–334, 2001.
- [24] Yuriy Makhlin, Gerd Schön, and Alexander Shnirman. Quantum-state engineering with josephson-junction devices. *Reviews of modern physics*, 73(2):357, 2001.
- [25] MB Weissman. 1 f noise and other slow, nonexponential kinetics in condensed matter. *Reviews of modern physics*, 60(2):537, 1988.
- [26] John Clarke and Frank K Wilhelm. Superconducting quantum bits. *Nature*, 453(7198):1031–1042, 2008.

Bibliography

- [27] Immanuel Bloch, Jean Dalibard, and Sylvain Nascimbène. Quantum simulations with ultracold quantum gases. *Nature Physics*, 8(4):267–276, 2012.
- [28] Waseem S Bakr, Jonathon I Gillen, Amy Peng, Simon Fölling, and Markus Greiner. A quantum gas microscope for detecting single atoms in a hubbard-regime optical lattice. *Nature*, 462(7269):74–77, 2009.
- [29] Christof Weitenberg, Manuel Endres, Jacob F Sherson, Marc Cheneau, Peter Schauß, Takeshi Fukuhara, Immanuel Bloch, and Stefan Kuhr. Single-spin addressing in an atomic mott insulator. *Nature*, 471(7338):319–324, 2011.
- [30] Franco Dalfovo, Stefano Giorgini, Lev P Pitaevskii, and Sandro Stringari. Theory of bose-einstein condensation in trapped gases. *Reviews of Modern Physics*, 71(3):463, 1999.
- [31] Michael Albiez, Rudolf Gati, Jonas Fölling, Stefan Hunsmann, Matteo Cristiani, and Markus K Oberthaler. Direct observation of tunneling and nonlinear self-trapping in a single bosonic josephson junction. *Physical review letters*, 95(1):010402, 2005.
- [32] S Levy, E Lahoud, I Shomroni, and J Steinhauer. The ac and dc josephson effects in a bose-einstein condensate. *Nature*, 449(7162):579–583, 2007.
- [33] Srikanth Raghavan, Augusto Smerzi, Stefano Fantoni, and SR Shenoy. Coherent oscillations between two weakly coupled bose-einstein condensates: Josephson effects, π oscillations, and macroscopic quantum self-trapping. *Physical Review A*, 59(1):620, 1999.
- [34] Augusto Smerzi, Stefano Fantoni, Stefano Giovanazzi, and SR Shenoy. Quantum coherent atomic tunneling between two trapped bose-einstein condensates. *Physical Review Letters*, 79(25):4950, 1997.
- [35] Luigi Amico, Andreas Osterloh, and Francesco Cataliotti. Quantum many particle systems in ring-shaped optical lattices. *Physical review letters*, 95(6):063201, 2005.
- [36] Sonja Franke-Arnold, Jonathan Leach, Miles J Padgett, Vassilis E Lembessis, Demos Ellinas, Amanda J Wright, John M Girkin, P Ohberg, and Aidan S Arnold. Optical ferris wheel for ultracold atoms. *Optics Express*, 15(14):8619–8625, 2007.
- [37] Olivier Morizot, Yves Colombe, Vincent Lorent, Hélène Perrin, and Barry M Garraway. Ring trap for ultracold atoms. *Physical Review A*, 74(2):023617, 2006.
- [38] C Ryu, PW Blackburn, AA Blinova, and MG Boshier. Experimental realization of josephson junctions for an atom squid. *Physical review letters*, 111(20):205301, 2013.

Bibliography

- [39] S Eckel, F Jendrzejewski, A Kumar, CJ Lobb, and GK Campbell. Interferometric measurement of the current-phase relationship of a superfluid weak link. *Physical Review X*, 4(3):031052, 2014.
- [40] Nigel R Cooper. Rapidly rotating atomic gases. *Advances in Physics*, 57(6):539–616, 2008.
- [41] Alexander L Fetter. Rotating trapped bose-einstein condensates. *Reviews of Modern Physics*, 81(2):647, 2009.
- [42] KW Madison, F Chevy, W Wohlleben, and J Dalibard. Vortex formation in a stirred bose-einstein condensate. *Physical Review Letters*, 84(5):806, 2000.
- [43] JR Abo-Shaeer, C Raman, JM Vogels, and Wolfgang Ketterle. Observation of vortex lattices in bose-einstein condensates. *Science*, 292(5516):476–479, 2001.
- [44] Kishore T Kapale and Jonathan P Dowling. Vortex phase qubit: Generating arbitrary, counterrotating, coherent superpositions in bose-einstein condensates via optical angular momentum beams. *Physical review letters*, 95(17):173601, 2005.
- [45] Johannes FS Brachmann, Waseem S Bakr, Jonathon Gillen, Amy Peng, and Markus Greiner. Inducing vortices in a bose-einstein condensate using holographically produced light beams. *Optics express*, 19(14):12984–12991, 2011.
- [46] MF Andersen, C Ryu, Pierre Cladé, Vasant Natarajan, A Vaziri, Kristian Helmerson, and WD Phillips. Quantized rotation of atoms from photons with orbital angular momentum. *Physical review letters*, 97(17):170406, 2006.
- [47] Jean Dalibard, Fabrice Gerbier, Gediminas Juzeliūnas, and Patrik Öhberg. Colloquium: Artificial gauge potentials for neutral atoms. *Reviews of Modern Physics*, 83(4):1523, 2011.
- [48] Michael V Berry. Quantal phase factors accompanying adiabatic changes. *Proceedings of the Royal Society of London. A. Mathematical and Physical Sciences*, 392(1802):45–57, 1984.
- [49] AG Aronov and Yu B Lyanda-Geller. Spin-orbit berry phase in conducting rings. *Physical review letters*, 70(3):343, 1993.
- [50] R Dum and M Olshanii. Gauge structures in atom-laser interaction: Bloch oscillations in a dark lattice. *Physical review letters*, 76(11):1788, 1996.
- [51] Michael Fleischhauer, Atac Imamoglu, and Jonathan P Marangos. Electromagnetically induced transparency: Optics in coherent media. *Reviews of modern physics*, 77(2):633, 2005.

Bibliography

- [52] Leonardo Fallani, Chiara Fort, Jessica Lye, and Massimo Inguscio. Bose-einstein condensate in an optical lattice with tunable spacing: transport and static properties. *Optics express*, 13(11):4303–4313, 2005.
- [53] R Scheunemann, FS Cataliotti, TW Hänsch, and M Weitz. Resolving and addressing atoms in individual sites of a co 2-laser optical lattice. *Physical Review A*, 62(5):051801, 2000.
- [54] Luigi Amico, Davit Aghamalyan, Filip Auksztol, Herbert Crepaz, Rainer Dumke, and Leong Chuan Kwek. Superfluid qubit systems with ring shaped optical lattices. *Scientific reports*, 4, 2014.
- [55] Davit Aghamalyan, Luigi Amico, and Leong Chuan Kwek. Effective dynamics of cold atoms flowing in two ring-shaped optical potentials with tunable tunneling. *Physical Review A*, 88(6):063627, 2013.
- [56] D. W. Hallwood, K. Burnett, and J. Dunningham. The barriers to producing multiparticle superposition states in rotating bose-einstein condensates. *Journal of Modern Optics*, 54(13-15):2129–2148, 2007.
- [57] David W Hallwood, Thomas Ernst, and Joachim Brand. Robust mesoscopic superposition of strongly correlated ultracold atoms. *Physical Review A*, 82(6):063623, 2010.
- [58] Andreas Nunnenkamp, Ana Maria Rey, and Keith Burnett. Superposition states of ultracold bosons in rotating rings with a realistic potential barrier. *Physical Review A*, 84(5):053604, 2011.
- [59] C Schenke, A Minguzzi, and FWJ Hekking. Nonadiabatic creation of macroscopic superpositions with strongly correlated one-dimensional bosons in a ring trap. *Physical Review A*, 84(5):053636, 2011.
- [60] David W Hallwood, Thomas Ernst, and Joachim Brand. Robust mesoscopic superposition of strongly correlated ultracold atoms. *Physical Review A*, 82(6):063623, 2010.
- [61] S Peil, James V Porto, B Laburthe Tolra, JM Obrecht, BE King, M Subbotin, SL Rolston, and WD Phillips. Patterned loading of a bose-einstein condensate into an optical lattice. *Physical Review A*, 67(5):051603, 2003.
- [62] Bo Tan, Narayanswamy R Sivakumar, and Krishnan Venkatakrishnan. Direct grating writing using femtosecond laser interference fringes formed at the focal point. *Journal of Optics A: Pure and Applied Optics*, 7(4):169, 2005.
- [63] TC Li, H Kelkar, D Medellin, and MG Raizen. Real-time control of the periodicity of a standing wave: an optical accordion. *Optics express*, 16(8):5465–5470, 2008.
- [64] JE Mooij, TP Orlando, L Levitov, Lin Tian, Caspar H Van der Wal, and Seth Lloyd. Josephson persistent-current qubit. *Science*, 285(5430):1036–1039, 1999.

Bibliography

- [65] E Paladino, YM Galperin, G Falci, and BL Altshuler. 1/f noise: Implications for solid-state quantum information. *Reviews of Modern Physics*, 86(2):361, 2014.
- [66] C Ryu, MF Andersen, P Cladé, Vasant Natarajan, Kristian Helmersson, and WD Phillips. Observation of persistent flow of a bose-einstein condensate in a toroidal trap. *Physical review letters*, 99(26):260401, 2007.
- [67] EM Wright, J Arlt, and K Dholakia. Toroidal optical dipole traps for atomic bose-einstein condensates using laguerre-gaussian beams. *Physical Review A*, 63(1):013608, 2000.
- [68] David McGloin, G Spalding, H Melville, Wilson Sibbett, and Kishan Dholakia. Applications of spatial light modulators in atom optics. *Optics Express*, 11(2):158–166, 2003.
- [69] Matthew Pasienski and Brian DeMarco. A high-accuracy algorithm for designing arbitrary holographic atom traps. *Optics express*, 16(3):2176–2190, 2008.
- [70] Alexander L Gaunt and Zoran Hadzibabic. Robust digital holography for ultracold atom trapping. *Scientific reports*, 2, 2012.
- [71] Emmanuel Courtade, Olivier Houde, Jean-François Clément, Philippe Verkerk, and Daniel Hennequin. Dark optical lattice of ring traps for cold atoms. *Physical Review A*, 74(3):031403, 2006.
- [72] Les Allen, Marco W Beijersbergen, RJC Spreeuw, and JP Woerdman. Orbital angular momentum of light and the transformation of laguerre-gaussian laser modes. *Physical Review A*, 45(11):8185, 1992.
- [73] KC Wright, LS Leslie, and NP Bigelow. Raman coupling of zeeman sublevels in an alkali-metal bose-einstein condensate. *Physical Review A*, 78(5):053412, 2008.
- [74] Stuart Moulder, Scott Beattie, Robert P Smith, Naaman Tammuz, and Zoran Hadzibabic. Quantized supercurrent decay in an annular bose-einstein condensate. *Physical Review A*, 86(1):013629, 2012.
- [75] C Ryu, PW Blackburn, AA Blinova, and MG Boshier. Experimental realization of josephson junctions for an atom squid. *Physical review letters*, 111(20):205301, 2013.
- [76] Stefano Giovanazzi, Augusto Smerzi, and Stefano Fantoni. Josephson effects in dilute bose-einstein condensates. *Physical review letters*, 84(20):4521, 2000.
- [77] K Volke-Sepulveda, V Garcés-Chávez, S Chávez-Cerda, J Arlt, and K Dholakia. Orbital angular momentum of a high-order bessel light beam. *Journal of Optics B: Quantum and Semiclassical Optics*, 4(2):S82, 2002.
- [78] K Bongs, S Burger, S Dettmer, D Hellweg, J Arlt, W Ertmer, and K Sengstock. Waveguide for bose einstein condensates. *Physical Review A*, 63(3):031602, 2001.

Bibliography

- [79] Aidan S Arnold. Extending dark optical trapping geometries. *Optics letters*, 37(13):2505–2507, 2012.
- [80] Dieter Jaksch, Ch Bruder, Juan Ignacio Cirac, Crispin W Gardiner, and Peter Zöller. Cold bosonic atoms in optical lattices. *Physical Review Letters*, 81(15):3108, 1998.
- [81] Luigi Amico and Vittorio Penna. Dynamical mean field theory of the bose-hubbard model. *Phys. Rev. Lett.*, 80:2189–2192, Mar 1998.
- [82] Ghassan George Batrouni and Richard T Scalettar. World-line quantum monte carlo algorithm for a one-dimensional bose model. *Physical Review B*, 46(14):9051, 1992.
- [83] JK Freericks and H Monien. Phase diagram of the bose-hubbard model. *EPL (Europhysics Letters)*, 26(7):545, 1994.
- [84] Y-J Lin, Rob L Compton, K Jimenez-Garcia, James V Porto, and Ian B Spielman. Synthetic magnetic fields for ultracold neutral atoms. *Nature*, 462(7273):628–632, 2009.
- [85] FDM Haldane. Effective harmonic-fluid approach to low-energy properties of one-dimensional quantum fluids. *Physical Review Letters*, 47(25):1840, 1981.
- [86] Marco Cominotti, Davide Rossini, Matteo Rizzi, Frank Hekking, and Anna Minguzzi. Optimal persistent currents for interacting bosons on a ring with a gauge field. *Physical review letters*, 113(2):025301, 2014.
- [87] Christoph Schenke. *Bosons de Tonks et Girardeau dans un anneau à une dimension*. PhD thesis, Université de Grenoble, 2012.
- [88] Mark Saffman, TG Walker, and Klaus Mølmer. Quantum information with rydberg atoms. *Reviews of Modern Physics*, 82(3):2313, 2010.
- [89] Rainer Blatt and David Wineland. Entangled states of trapped atomic ions. *Nature*, 453(7198):1008–1015, 2008.
- [90] Lieven MK Vandersypen, Matthias Steffen, Gregory Breyta, Costantino S Yannoni, Mark H Sherwood, and Isaac L Chuang. Experimental realization of shor’s quantum factoring algorithm using nuclear magnetic resonance. *Nature*, 414(6866):883–887, 2001.
- [91] JR Petta, Alexander Comstock Johnson, JM Taylor, EA Laird, A Yacoby, Mikhail D Lukin, CM Marcus, MP Hanson, and AC Gossard. Coherent manipulation of coupled electron spins in semiconductor quantum dots. *Science*, 309(5744):2180–2184, 2005.
- [92] Waseem S Bakr, Amy Peng, M Eric Tai, Ruichao Ma, Jonathan Simon, Jonathon I Gillen, Simon Foelling, Lode Pollet, and Markus Greiner. Probing the superfluid–to–mott insulator transition at the single-atom level. *Science*, 329(5991):547–550, 2010.

Bibliography

- [93] Jacob F Sherson, Christof Weitenberg, Manuel Endres, Marc Cheneau, Immanuel Bloch, and Stefan Kuhr. Single-atom-resolved fluorescence imaging of an atomic mott insulator. *Nature*, 467(7311):68–72, 2010.
- [94] Erik Lucero, Rami Barends, Yu Chen, Julian Kelly, Matteo Mariantoni, Anthony Megrant, Peter OâMalley, Daniel Sank, Amit Vainsencher, James Wenner, et al. Computing prime factors with a josephson phase qubit quantum processor. *Nature Physics*, 8(10):719–723, 2012.
- [95] Andreas Nunnenkamp, Ana Maria Rey, and Keith Burnett. Generation of macroscopic superposition states in ring superlattices. *Physical Review A*, 77(2):023622, 2008.
- [96] Dmitry Solenov and Dmitry Mozyrsky. Macroscopic two-state systems in trapped atomic condensates. *Physical Review A*, 82(6):061601, 2010.
- [97] Hans Peter Büchler. Microscopic derivation of hubbard parameters for cold atomic gases. *Physical review letters*, 104(9):090402, 2010.
- [98] M Niemeyer, JK Freericks, and H Monien. Strong-coupling perturbation theory for the two-dimensional bose-hubbard model in a magnetic field. *Physical Review B*, 60(4):2357, 1999.
- [99] AJ Leggett. Granular nanoelectronics. *NATO ASI Ser. B, 251Plenum, New York*, page 297, 1991.
- [100] Daniel Loss. Parity effects in a luttinger liquid: Diamagnetic and paramagnetic ground states. *Physical review letters*, 69(2):343, 1992.
- [101] HJ Schulz and B Sriram Shastry. A new class of exactly solvable interacting fermion models in one dimension. *Physical review letters*, 80(9):1924, 1998.
- [102] Gianluca Rastelli, Ioan M Pop, and FWJ Hekking. Quantum phase slips in josephson junction rings. *Physical Review B*, 87(17):174513, 2013.
- [103] David Jeffrey Griffiths and Edward G Harris. *Introduction to quantum mechanics*, volume 2. Prentice Hall New Jersey, 1995.
- [104] Andreas Nunnenkamp and Ana Maria Rey. Macroscopic superposition states in rotating ring lattices. *Journal of Modern Optics*, 55(19-20):3339–3348, 2008.
- [105] David W Hallwood and Joachim Brand. Engineering mesoscopic superpositions of superfluid flow. *Physical Review A*, 84(4):043620, 2011.
- [106] Vladimir A Kashurnikov, Alexei I Podlivaev, Nikolai V Prokofâev, and Boris V Svistunov. Supercurrent states in one-dimensional finite-size rings. *Physical Review B*, 53(19):13091, 1996.

Bibliography

- [107] Elliott H Lieb and Werner Liniger. Exact analysis of an interacting bose gas. i. the general solution and the ground state. *Physical Review*, 130(4):1605, 1963.
- [108] MA Cazalilla. Bosonizing one-dimensional cold atomic gases. *Journal of Physics B: Atomic, Molecular and Optical Physics*, 37(7):S1, 2004.
- [109] Marco Cominotti, Matteo Rizzi, Davide Rossini, Davit Aghamalyan, Luigi Amico, Leon C Kwek, Frank Hekking, and Anna Minguzzi. Optimal scaling of persistent currents for interacting bosons on a ring. *arXiv preprint arXiv:1409.1835*, 2014.
- [110] Kalani Hettiarachchilage, Valéry G Rousseau, Ka-Ming Tam, Mark Jarrell, and Juana Moreno. Phase diagram of the bose-hubbard model on a ring-shaped lattice with tunable weak links. *Physical Review A*, 87(5):051607, 2013.
- [111] David W Hallwood, Keith Burnett, and Jacob Dunningham. The barriers to producing multiparticle superposition states in rotating bose-einstein condensates. *Journal of Modern Optics*, 54(13-15):2129–2148, 2007.
- [112] Bascom S Deaver and William M Fairbank. Experimental evidence for quantized flux in superconducting cyclinders. *Physical Review Letters*, 7(2):43–46, 1961.
- [113] N. Byers and C. N. Yang. Magnetic flux through a superconducting ring. *Physical Review Letters*, 7(46):50, 1961.
- [114] Lars Onsager. Magnetic flux through a superconducting ring. *Physical Review Letters*, 7(2):50, 1961.
- [115] LP Levy, G Dolan, J Dunsmuir, and H Bouchiat. Magnetization of mesoscopic copper rings: Evidence for persistent currents. *Physical review letters*, 64(17):2074, 1990.
- [116] D Mailly, C Chapelier, and A Benoit. Experimental observation of persistent currents in gaas-algaas single loop. *Physical review letters*, 70(13):2020, 1993.
- [117] Hendrik Bluhm, Nicholas C Koshnick, Julie A Bert, Martin E Huber, and Kathryn A Moler. Persistent currents in normal metal rings. *Physical review letters*, 102(13):136802, 2009.
- [118] AC Bleszynski-Jayich, WE Shanks, B Peaudecerf, E Ginossar, F Von Oppen, L Glazman, and JGE Harris. Persistent currents in normal metal rings. *Science*, 326(5950):272–275, 2009.
- [119] Dmitry Solenov and Dmitry Mozyrsky. Metastable states and macroscopic quantum tunneling in a cold-atom josephson ring. *Physical review letters*, 104(15):150405, 2010.
- [120] Stuart Moulder, Scott Beattie, Robert P Smith, Naaman Tammuz, and Zoran Hadzibabic. Quantized supercurrent decay in an annular bose-einstein condensate. *Physical Review A*, 86(1):013629, 2012.

Bibliography

- [121] Noel Murray, Michael Krygier, Mark Edwards, KC Wright, GK Campbell, and Charles W Clark. Probing the circulation of ring-shaped bose-einstein condensates. *Physical Review A*, 88(5):053615, 2013.
- [122] F Bloch. Josephson effect in a superconducting ring. *Physical Review B*, 2(1):109, 1970.
- [123] F Bloch. Superfluidity in a ring. *Physical Review A*, 7(6):2187, 1973.
- [124] AJ Leggett. Granular nanoelectronics. *NATO ASI Ser. B, 251 Plenum, New York*, page 297, 1991.
- [125] Eberhard K Riedel and Felix von Oppen. Mesoscopic persistent current in small rings. *Physical Review B*, 47(23):15449, 1993.
- [126] FWJ Hekking and LI Glazman. Quantum fluctuations in the equilibrium state of a thin superconducting loop. *Physical Review B*, 55(10):6551, 1997.
- [127] Alexey V Ponomarev, Sergey Denisov, and Peter Hänggi. Quantum machine using cold atoms. *Journal of Computational and Theoretical Nanoscience*, 7(11):2441–2447, 2010.
- [128] John D Andersen and VM Kenkre. Self-trapping and time evolution in some spatially extended quantum nonlinear systems: Exact solutions. *Physical Review B*, 47(17):11134, 1993.
- [129] GJ Milburn, J Corney, EM Wright, and DF Walls. Quantum dynamics of an atomic bose-einstein condensate in a double-well potential. *Physical Review A*, 55(6):4318, 1997.
- [130] LD Landau. 1/f noise: Implications for solid-state quantum information. *Z. Sowjetunion*, 3:664, 1933.
- [131] JE Mooij, TP Orlando, L Levitov, Lin Tian, Caspar H Van der Wal, and Seth Lloyd. Josephson persistent-current qubit. *Science*, 285(5430):1036–1039, 1999.
- [132] Dmitry Solenov and Dmitry Mozyrsky. Cold atom qubits. *Journal of Computational and Theoretical Nanoscience*, 8(3):481–489, 2011.
- [133] Michael A Nielsen and Isaac L Chuang. *Quantum computation and quantum information*. Cambridge university press, 2010.
- [134] Heng Fan, Vwani Roychowdhury, and Thomas Szkopek. Optimal two-qubit quantum circuits using exchange interactions. *Physical Review A*, 72(5):052323, 2005.
- [135] Aaron Reinhard, Jean-Félix Riou, Laura A Zundel, David S Weiss, Shuming Li, Ana Maria Rey, and Rafael Hipolito. Self-trapping in an array of coupled 1d bose gases. *Physical review letters*, 110(3):033001, 2013.

Bibliography

- [136] Shuming Li, Salvatore R Manmana, Ana Maria Rey, Rafael Hipolito, Aaron Reinhard, Jean-Félix Riou, Laura A Zundel, and David S Weiss. Self-trapping dynamics in a 2d optical lattice. *arXiv preprint arXiv:1305.4442*, 2013.
- [137] Romain Dubessy, Thomas Liennard, Paolo Pedri, and Hélène Perrin. Critical rotation of an annular superfluid bose-einstein condensate. *Physical Review A*, 86(1):011602, 2012.
- [138] Maxim Olshanii. Atomic scattering in the presence of an external confinement and a gas of impenetrable bosons. *Physical Review Letters*, 81(5):938, 1998.
- [139] Marvin Girardeau. Relationship between systems of impenetrable bosons and fermions in one dimension. *Journal of Mathematical Physics*, 1(6):516–523, 1960.
- [140] Andrew Lenard. Momentum distribution in the ground state of the one-dimensional system of impenetrable bosons. *Journal of Mathematical Physics*, 5(7):930–943, 1964.
- [141] A Minguzzi, P Vignolo, and MP Tosi. High-momentum tail in the tonks gas under harmonic confinement. *Physics Letters A*, 294(3):222–226, 2002.
- [142] Ulrich Weiss. Low-temperature conduction and dc current noise in a quantum wire with impurity. *Solid state communications*, 100(5):281–285, 1996.
- [143] Oliver Penrose and Lars Onsager. Bose-einstein condensation and liquid helium. *Physical Review*, 104(3):576, 1956.
- [144] PC Hohenberg. Existence of long-range order in one and two dimensions. *Physical Review*, 158(2):383, 1967.
- [145] L Pitaevskii and S Stringari. Uncertainty principle, quantum fluctuations, and broken symmetries. *Journal of low temperature physics*, 85(5-6):377–388, 1991.
- [146] Rosario Fazio and Herre Van Der Zant. Quantum phase transitions and vortex dynamics in superconducting networks. *Physics Reports*, 355(4):235–334, 2001.
- [147] AO Caldeira and AJ Leggett. Influence of dissipation on quantum tunneling in macroscopic systems. *Physical Review Letters*, 46(4):211, 1981.
- [148] Milton Abramowitz and Irene A Stegun. *Handbook of mathematical functions: with formulas, graphs, and mathematical tables*. Number 55. Courier Dover Publications, 1972.
- [149] Marcos Rigol and Alejandro Muramatsu. Ground-state properties of hard-core bosons confined on one-dimensional optical lattices. *Physical Review A*, 72(1):013604, 2005.

Bibliography

- [150] Luigi Amico and Vladimir Korepin. Universality of the one-dimensional bose gas with delta interaction. *Annals of Physics*, 314(2):496–507, 2004.
- [151] Belén Paredes, Artur Widera, Valentin Murg, Olaf Mandel, Simon Fölling, Ignacio Cirac, Gora V Shlyapnikov, Theodor W Hänsch, and Immanuel Bloch. Tonks–girardeau gas of ultracold atoms in an optical lattice. *Nature*, 429(6989):277–281, 2004.
- [152] Toshiya Kinoshita, Trevor Wenger, and David S Weiss. Observation of a one-dimensional tonks–girardeau gas. *Science*, 305(5687):1125–1128, 2004.
- [153] RM Noack and SR Manmana. Lectures on the physics of highly correlated electron systems ix: Ninth training course in the physics of correlated electron systems and high- t_c superconductors. In *AIP Conf. Proc*, number 789, page 93, 2005.
- [154] Holger Fehske, Ralf Schneider, and Alexander Weiße. *Computational many-particle physics*, volume 739. Springer, 2008.
- [155] JM Zhang and RX Dong. Exact diagonalization: the bose–hubbard model as an example. *European Journal of Physics*, 31(3):591, 2010.
- [156] Ulrich Schollwöck. The density-matrix renormalization group in the age of matrix product states. *Annals of Physics*, 326(1):96–192, 2011.
- [157] Frank Verstraete, Valentin Murg, and J Ignacio Cirac. Matrix product states, projected entangled pair states, and variational renormalization group methods for quantum spin systems. *Advances in Physics*, 57(2):143–224, 2008.
- [158] Frank Verstraete, Diego Porras, and J Ignacio Cirac. Density matrix renormalization group and periodic boundary conditions: a quantum information perspective. *Physical review letters*, 93(22):227205, 2004.
- [159] Peter Pippan, Steven R White, and Hans Gerd Evertz. Efficient matrix-product state method for periodic boundary conditions. *Physical Review B*, 81(8):081103, 2010.
- [160] M. Weyrauch and M. V. Rakov. Efficient mps algorithm for periodic boundary conditions and applications. *Ukr. J. Phys.*, 58(7):657–665, 2013.

APPENDIX A

Appendix

A.1 Quasi one dimensionality and 1D s-wave scattering length

In this section we discuss a realistic model of a harmonic potential $V = m\omega_{\perp}^2(x^2 + y^2)/2$, with a transverse trapping frequency ω_{\perp} , for trapping cold atoms which effectively can be described by a one dimensional model. For a harmonic confinement to be effectively 1D all the energies involved(thermal energy of gas, chemical potential) should be much smaller than the transverse excitation energy $\hbar\omega_{\perp}$. This model has been suggested by M.Olshani in Ref. [138], and in that paper an expression for a 1D scattering wavelength has been obtained. In order to consider scattering problem between two atoms which interact by Huang's pseudopotential we write down a Schrödinger equation for the system:

$$\left[\frac{p_z^2}{2\mu} + g\delta(\mathbf{r})\frac{\partial}{\partial r}(r.) + H_{\perp} \right] \Psi = E\Psi \quad (\text{A.1})$$

here $\mathbf{r} = \mathbf{r}_1 - \mathbf{r}_2$ is the relative coordinate and $\mu = m/2$ is the reduced mass of the particles involved in the scattering problem. The operator $\frac{\partial}{\partial r}(r.)$ is introduced to remove $1/r$ divergence of the scattered wave. The transverse

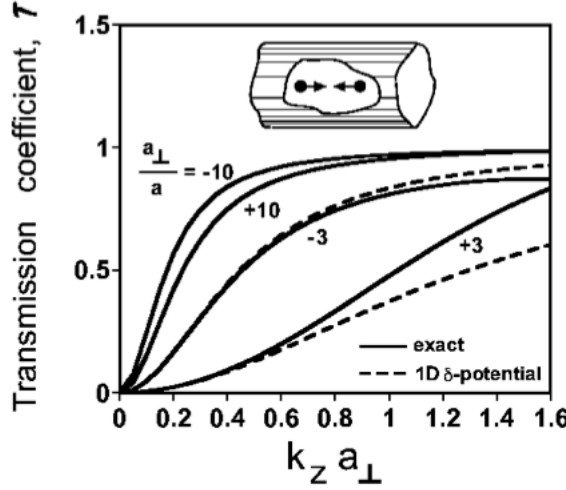


Figure A.1: Comparison of the transmission coefficient for the systems interacting with 1D and 3D delta potentials. For the value $a_{\perp} = \pm 10$ these two transmission coefficients almost coincide. Taken from Ref.[138].

2D harmonic oscillator Hamiltonian is given by:

$$H_{\perp} = \frac{p_x^2 + p_y^2}{2\mu} + \frac{\mu\omega_{\perp}^2(x^2 + y^2)}{2} \quad (\text{A.2})$$

Here two important assumptions should be made:

- 1) The incident wave $e^{ik_z z}\phi_{n=0, m_z=0}$ corresponds to the ground state of the transverse Hamiltonian,
- 2) $\hbar k_z^2/2\mu < 2\hbar\omega_{\perp}$.

Here m_z is an angular momentum with respect to the z-axis, and n related to the energy of the system by $E = \hbar\omega_{\perp}(n + 1)$, where n takes integer positive values and if its even(odd) then $m_z = 0, 2, \dots, n(1, 2, \dots, n)$. It is useful to introduce the width of the ground state wave function $a_{\perp} = \sqrt{\hbar/\mu\omega}$ for present calculations. The scattering wave function in the limit

A.1. Quasi one dimensionality and 1D s-wave scattering length

$|z| \rightarrow \infty$ is given by:

$$\Psi(z, \rho) = (e^{ik_z z} + A_{even} e^{ik_z |z|} + A_{odd} e^{ik_z |z|}) \phi_{0,0}(\rho) \quad (\text{A.3})$$

here $\rho = \sqrt{x^2 + y^2}$, and $A_{even, odd}$ are giving the scattering amplitudes for the odd and even waves. It is important to notice that the transverse state of the system(which is a ground state) remains unchanged during the whole process. It turns out, that analytic expressions for the scattering amplitudes can be found as it was shown in Ref. [138] they can be introduced as:

$$A_{even} = -\frac{1}{1 + ik_z a_{1D} - O((k_z a_\perp)^3)} \quad (\text{A.4})$$

Here a_{1D} is the 1D scattering length and it reads as follows:

$$a_{1D} = -\frac{a_\perp^2}{2a} \left[1 - C \frac{a}{a_\perp} \right] \quad (\text{A.5})$$

where $C \approx 1.4603$ and $A_{odd} = 0$.

Now let us consider fully one dimensional scattering problem, where particles interact with a 1D delta potential $U(z) = g_{1D} \delta(z)$, and scattering wave length is given by the a_{1D} . In that case the scattering amplitude of even waves(again $A_{odd} = 0$) reads as:

$$A_{even} = -\frac{1}{1 + ik_z a_{1D}} \quad (\text{A.6})$$

By comparing Eqs. (A.4) and (A.6) we conclude that in the limit $k_z a_\perp \ll 1$, the initial system can be described by the interaction potential $U(z) =$

$g_{1D}\delta(z)$, where g_{1D} is given by:

$$g_{1D} = \frac{g}{\pi a_\perp^2} \left[1 - C \frac{a}{a_\perp} \right]^{-1} \quad (\text{A.7})$$

and 1D scattering length is given by Eq. (A.5). In order to compare these two cases the transmission coefficient $T = |1 + A_{even} + A_{odd}|^2$ has been calculated, with help of Eqs. (A.4) and (A.6). This comparison is demonstrated on Fig.A.1. As we can see a very good agreement is achieved in the limit $k_z a_\perp \ll 1$. Moreover, even for intermediate value of $k_z a_\perp$ good agreement is evidenced for the values $a_\perp = \pm 10$.

We conclude that scattering of cold atoms trapped in cigar-shaped potentials can be well described with 1D delta potential when transverse degrees of freedom are frozen out.

A.2 Tonks-Girardeau gas

In the limit ($g \rightarrow \infty$)(impenetrable-boson limit) the system given by the Lieb-Liniger or the Bose-Hubbard model has an exact solution, which can be obtained by so-called Bose-Fermi mapping[139] or Jordan-Wigner transformation. The main idea is that due to an infinite delta-interaction potential the wave function should vanish upon the condition that two particles are at the same point in the space. Same condition holds for fermions, due to Pauli exclusion principle, Fermi wave functions vanish when two particles occupy the same quantum state. Taking into account this similarity, we conclude that there should be a mapping between the Fermi wave function Ψ^F (which is a solution of the same Schrödinger equation) and the bosonic

A.2. Tonks-Girardeau gas

wave function Ψ^B . This mapping is given by the following expression:

$$\Psi^B = A(x_1, x_2, \dots, x_n) \Psi^F \quad (\text{A.8})$$

where $A(x_1, x_2, \dots, x_n) = \prod_{j>l} \text{sgn}(x_j - x_l)$ is a mapping function, which ensures the Ψ^B is a bosonic wave function. Moreover, if Ψ^F satisfies to the periodic boundary conditions then Ψ^B will also satisfy to the same boundary conditions, under the assumption that the total number of particles is odd. Ansatz given by Eq. (A.8), allows to find a solutions of the bosonic system which is subject to an additional conditions:

$$\Psi(x_1, x_2, \dots, x_n) = 0 \quad \text{if } x_j = x_l, \quad 1 \leq j < l \leq n \quad (\text{A.9})$$

As it was noticed in [139] this correspondence relation simplifies for the ground state(this simplification happens due to the fact that generally Bose ground state is positive) and takes form:

$$\Psi_G^B = |\Psi_G^F| \quad (\text{A.10})$$

This condition is very useful for finding the solution of Lieb-Liniger model in the limit ($g \rightarrow \infty$). In this limit problem reduces to the following eigenvalue equations:

$$\sum_{i=1}^N -\frac{\hbar^2}{2m} \frac{\partial^2 \Psi^B}{\partial x_i^2} = E \Psi^B \quad (\text{A.11})$$

which are subject to an additional condition given be Eq. (A.9). For finding the ground-state solution of this problem it is enough to find a solution of free-fermion problem and then apply Eq. (A.10). The ground state of the free particle system is given by the Slauter determinant of N plane-

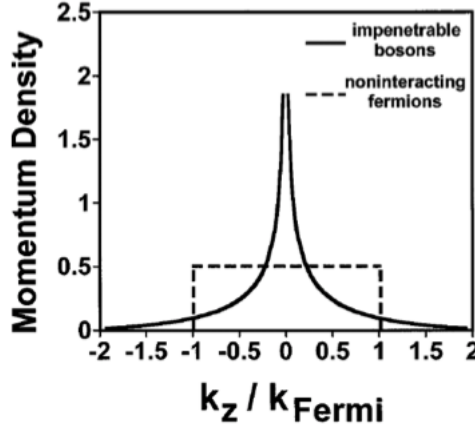


Figure A.2: Comparison of the momentum distributions for a Tonks-Girardeau gas and a free Fermi gas. Taken from [138]

waves of the form e^{ikx} . Momentum values k are determined from the periodic boundary conditions $k = 2\pi i/L$, where i is an integer in the interval $-0.5(N-1) \leq i \leq 0.5(N-1)$. For the periodic boundary conditions the final result reads as:

$$\Psi_G^B \propto \prod_{j>l} |\sin [\pi L^{-1}(x_j - x_l)]| \quad (\text{A.12})$$

where L is the circumference of the ring. The ground state energy can be obtained by filling the Fermi sphere:

$$E_G = \frac{\hbar^2}{2m} \sum_{i=1}^{1/2(n-1)} \frac{2\pi i^2}{L} = \frac{1}{6}(n - n^{-1}) \frac{\pi \hbar N}{m L^2} \quad (\text{A.13})$$

The density profiles and even the density correlation functions are the same for the Fermi gas and the Tonks-Girardeau gas. However, the momentum distributions for this gases are quite different. Momentum distribution $n(k)$

A.3. Exact solution in the limits of ideal and Tonks-Girardeu gas for the homogeneous ring with a delta-barrier

is defined in terms of one-body density matrix $\rho(x, y)$ in the following way:

$$\begin{aligned} n(k) &= \int \int dx dy e^{ik(x-y)} \rho(x, y) \\ \rho(x, y) &= \int \dots \int dx_2 \dots dx_N \Psi^B(x, x_2, \dots, x_N) \Psi^{B*}(y, x_2, \dots, x_N) \end{aligned} \quad (\text{A.14})$$

As it is seen from Fig. A.2, in the case of the hard-core bosons a zero momentum state is highly occupied however higher momentum tales also demonstrate non-zero occupation. Close to the zero momentum distribution behaves as $1/\sqrt{k}$ [140], and in the limit ($k \rightarrow \infty$) it scales as $1/k^4$ [141].

A.3 Exact solution in the limits of ideal and Tonks-Girardeu gas for the homogeneous ring with a delta-barrier

As it was previously demonstrated in Refs.[57, 86] the model introduced by Eq. (3.11) has exact solutions in the limits of ideal bose gas ($g = 0$) and Tonks-Girardeu gas($g \rightarrow \infty$). In both cases this is possible due to the fact that many body dynamics can be reduced to the single-particle dynamics. Let us consider the solution of many-body Schrödinger equation:

$$H\Psi(x_1, \dots, x_N) = E\Psi(x_1, \dots, x_N) \quad (\text{A.15})$$

for these cases. For a non interacting(NI) bosonic system a many-body ground state wave function is given by a product of N equal single-particle wave functions $\psi_0(x_i)$, and all of them are identical , since all the particles

Appendix A. Appendix

are occupying same state due to Bose statistics and in this case, it reads as:

$$\Psi_{NI}(x_1, \dots, x_N) = \prod_{i=1}^N \psi_0(x_i). \quad (\text{A.16})$$

For a Tonks-Girardeau(TG) gas the solution can be simply obtained by mapping a system on a system of non interacting spinless fermions as it was discussed in detail in Section A.2. In this case the corresponding many-body wave function is given by:

$$\Psi_{TG}(x_1, \dots, x_N) = \prod_{1 \leq j < l \leq N} \operatorname{sgn}(x_j - x_l) \det[\psi_k(x_i)]. \quad (\text{A.17})$$

The single-particle wave functions ψ_k can be obtained from the solution of a one-body Schrödinger equation:

$$\left[\frac{\hbar^2}{2m} \left(-i \frac{\partial}{\partial x_i} - \frac{2\pi\Omega}{L} \right)^2 + \Lambda\delta(x) \right] \psi_n = \varepsilon_n \psi_n, \quad (\text{A.18})$$

where functions ψ_n satisfy periodic boundary conditions. Here for simplicity we consider N to be an odd number. Ground state wave functions for the non-interacting and the impenetrable boson cases are given through single particle energies ε_n , by the following expressions: $E_{NI} = N\varepsilon_0$, $E_{TG} = \sum_{i=0}^{N-1} \varepsilon_i$.

Eq. (A.18) can be solved by looking for the solution in terms of plane waves:

$$\psi_n(x) = \begin{cases} \frac{1}{A_n} e^{-\Omega\pi} [e^{ik_n(x-L/2)} + B_n e^{-ik_n(x-L/2)}] & x \in [0, L/2) \\ \frac{1}{A_n} e^{-\Omega\pi} [e^{ik_n(x+L/2)} + B_n e^{-ik_n(x+L/2)}] & x \in [-L/2, 0) \end{cases}$$

A.4. Luttinger liquid theory

where B_n is a scattering amplitude from the delta-barrier. The normalization factor A_n (which is found by imposing $\int_{-L/2}^{L/2} |\psi_n|^2 = 1$) is given by $A_n = \sqrt{L(1 + A_n^2 + 2A_n \sin(k_n L)/k_n L)}$. The scattering amplitude $B_n = \frac{\sin(k_n L/2 + \Omega\pi)}{\sin(k_n L/2 - \Omega\pi)}$ and is found from the condition $\psi_n(0^+) = \psi_n(0^-)$, which means that scattering amplitudes from delta-barrier are equal due to the reflection symmetry. Wave vectors k_n can be found as a solution of the transcendental equation (which is obtained from that cusp condition $\partial_x \psi_n(0^+) - \partial_x \psi_n(0^-) = 2\lambda \psi_n(0)$):

$$k_n = \lambda \frac{\sin(k_n L)}{\cos(2\pi\Omega) - \cos(k_n L)}, \quad (\text{A.20})$$

where $\lambda = m\Lambda/\hbar^2$.

Corresponding energy values are given by $\varepsilon_n = \hbar^2 k_n^2 / 2m$. We conclude that in the limits of the non-interacting and the impenetrable boson cases the exact solutions can be obtained for the ground state energy of the system.

A.4 Luttinger liquid theory

As it is well known superfluids are well described by the phase and the density. Here the system is described by the bosonic field $\Psi^\dagger(x)$ which obey bosonic commutation relations and given by the following expression:

$$\Psi^\dagger(x) = \sqrt{\rho(x)} e^{-i\phi(x)}, \quad (\text{A.21})$$

where $\rho(x)$ and $\phi(x)$ are the operators of the density and the phase. As it was demonstrated by Haldane [85] the operators $\rho = \Psi^\dagger(x)\Psi(x)$ and $\Psi^\dagger(x)$

Appendix A. Appendix

have the following decompositions:

$$\begin{aligned}\rho(x) &= [\rho_0 + \Pi(x)] \sum_{m=-\infty}^{+\infty} e^{2mi\Theta(x)}, \\ \Psi^\dagger(x) &= A\sqrt{[\rho_0 + \Pi(x)]} \sum_{m=-\infty}^{+\infty} e^{2mi\Theta(x)} e^{-i\phi(x)},\end{aligned}\quad (\text{A.22})$$

where a slowly varying field $\partial_x \Theta(x) = \pi(\rho_0 + \Pi(x))$, and it has a property that at the position of the j -th particle x_j , $\Theta(x_j) = \pi j$. The ground state density of the system is given by $\rho_0 = N/L$ and A depends on the way in which delta function is defined, it can be found from the equation $\delta(x)^2 = A\delta(x)$. In the density decomposition the $m = 0$ term which is $\rho_0 + \Pi(x)$ describes long wavelength fluctuations, $m = \pm 1$ describe fluctuations with momentum $q \approx \pm 2\pi\rho_0$ and so on. We comment that in order to satisfy bosonic commutation relations the following condition should be imposed: $[\Pi(x), \phi(y)] = \delta(x-y)$, which means $\Pi(x)$ and $\phi(x)$ are conjugate variables. In the next step we are making use of the decompositions given by Eq.(A.23) in order to derive low-energy Hamiltonian for the bosons which interact with a point like potential. This Hamiltonian reads as:

$$H = \frac{\hbar^2}{2m} \int_0^L dx \nabla \Psi^\dagger(x) \nabla \Psi(x) + \frac{g}{2} \int_0^L dx \rho^2(x) \quad (\text{A.23})$$

In the lowest order $\nabla \Psi^\dagger(x) \nabla \Psi(x) \approx \rho_0 (\nabla \phi(x))^2$ and $\rho^2(x) = (\rho_0 + \Pi(x))^2$. After introducing a new parameter $\theta(x) = \Theta(x) - \pi\rho_0 x$, we arrive to the Luttinger liquid Hamiltonian, which is given by:

$$H_L = \frac{\hbar v_s}{2\pi} \int_0^L dx \left(K(\nabla \phi(x))^2 + \frac{1}{K} (\nabla \theta(x))^2 \right) \quad (\text{A.24})$$

where K is the Luttinger parameter and v_s is the sound velocity. It turns out that there are relations between Luttinger parameter and between the

A.4. Luttinger liquid theory

Lieb-Liniger parameter γ , as it was demonstrated by Cazalilla in Ref.[108]:

$$\begin{aligned} K(\gamma \gg 1) &= 1 + \frac{4}{\gamma^2} + O(\gamma^{-3}), \\ K(\gamma \ll 1) &= \frac{\pi}{\sqrt{\gamma}} \left(1 - \frac{\sqrt{\gamma}}{2\pi} \right). \end{aligned} \quad (\text{A.25})$$

For the system with periodic boundary conditions the expression for the one-body density matrix can be obtained with methods of conformal field theory [108], and the result reads as follows:

$$\langle \Psi^\dagger(x) \Psi(0) \rangle = \rho_0 \left[\frac{1}{\rho_0 d(x|L)} \right]^{\frac{1}{2K}} \left(b_0 + \sum_{m=1}^{+\infty} b_m \left[\frac{1}{\rho_0 d(x|L)} \right]^{2mK^2} \cos(2\pi m \rho_0 x) \right) \quad (\text{A.26})$$

in this expression the dimensionless parameters b_m are non-universal and they depend on the microscopic properties of the model and $d(x|L) = L|\sin \pi x/L|/\pi$ is so-called cord function. In the thermodynamic limit $L \rightarrow \infty$ the cord function takes form $|x|$. It turns out that the oscillatory terms in Eq.(A.26) become more important for small K , and for large K values they can be safely neglected. For large values of K , the one-body density matrix takes form:

$$\langle \Psi^\dagger(x) \Psi(x) \rangle \propto \left[\frac{1}{|x|} \right]^{\frac{1}{2K}} \quad (\text{A.27})$$

This result shows that even for the one dimensional systems there is a quasi off diagonal long range order for the case of weakly interacting mesoscopic systems.

A.4.1 The limits of weak and strong barrier for the homogeneous ring with a delta-barrier

It is possible to treat the system introduced in Section 3.3 perturbatively in the limits of weak and strong barriers [86].

In the weak barrier case the system satisfies periodic boundary conditions and we make mode expansion for the density and the phase fields:

$$\begin{aligned}\theta(x) &= \theta_0 + \frac{1}{2} \sum_{q \neq 0} \left| \frac{2\pi K}{qL} \right| [e^{iqx} b_q + e^{-iqx} b_q^\dagger], \\ \phi(x) &= \phi_0 + \frac{2\pi x}{L} (J - \Omega) + \frac{1}{2} \sum_{q \neq 0} \left| \frac{2\pi K}{qL} \right| \text{sgn}(q) [e^{iqx} b_q + e^{-iqx} b_q^\dagger],\end{aligned}\quad (\text{A.28})$$

where $q = 2\pi j/L$ with j being an integer number, J is the angular momentum and for the bosonic fields the following commutation relations are implied: $[b_q, b_{q'}^\dagger] = \delta_{q,q'}$, $[J, e^{-2i\theta_0}] = e^{-2i\theta_0}$. The last relation also implies that $e^{-2i\theta_0}|J\rangle = |J+1\rangle$, which means that $e^{-2i\theta_0}$ acts as a raising operator for the states with a given angular momentum J . By keeping only lowest harmonics in the density field expansion we arrive to the following expression for the barrier:

$$H_B \simeq 2\Lambda\rho_0 \cos(2\theta(0)) = \rho_0\Lambda \sum_J [|J-1\rangle\langle J| e^{2i\delta\theta(0)} + |J\rangle\langle J+1| e^{-2i\delta\theta(0)}] \quad (\text{A.29})$$

Then by using the mode expansions and averaging the total Hamiltonian over quantum fluctuations, we obtain the following effective Hamiltonian:

$$H_J = \rho_0\Lambda_{eff} \sum_J [|J+1\rangle\langle J| + |J\rangle\langle J+1|] \quad (\text{A.30})$$

The effective barrier strength Λ_{eff} is obtained after averaging over the density fluctuations $\Lambda_{eff} = \langle \Lambda^{\pm 2i\delta\theta(0)} \rangle = \Lambda(d/L)^K$, where d is a short-

A.4. Luttinger liquid theory

distance cutoff, which is of the order of interparticle distance. It can be shown that for the specific model given by Eq. (3.12) the short distance cutoff is given by $d = K/\rho_0$.

In the next step the degenerate perturbation theory is performed and the ground state energy per particle is obtained as:

$$E_G(\Omega)/N = E_0[(\Omega - J - 1/2)^2 - \sqrt{(\Omega - J - 1/2)^2 + \lambda_{eff}/4\pi^2}], \quad (\text{A.31})$$

with $E_0 = 2\pi^2\hbar^2/mL^2$, and $\lambda_{eff} = m\Lambda_{eff}L/\pi\hbar^2$.

In the strong barrier limit(which is equivalent to the weak tunnel limit) the system effectively satisfies to the open boundary conditions and the following mode expansion implies:

$$\begin{aligned} \theta(x) &= \theta_0 + i \sum_{q \neq 0} \left(\frac{\pi K}{qL} \right) \sin(qx)(b_q - b_q^\dagger), \\ \phi(x) &= \phi_0 + \sum_{q \neq 0} \left(\frac{\pi}{qLK} \right) \cos(qx)(b_q + b_q^\dagger), \end{aligned} \quad (\text{A.32})$$

where $q = \pi j/L$, with j integer. The angular momentum does not enter here since no circulation is allowed in this limit. After making similar manipulations as in a weak barrier case we obtain the following Ω -dependent part for the ground state energy per particle(note the similarity of this expression with the energy of single Josephson junction superconducting loop):

$$\begin{aligned} E_G(\Omega)/N &= -2(t/L)(\cos(\phi(L) - \phi(0) + 2\pi\Omega \cos 2\pi\Omega)) \\ &= -2(t/L)(d/L)^{1/K} \cos(2\pi\Omega) \end{aligned} \quad (\text{A.33})$$

An expression for the effective tunneling rate is obtained after averaging the

Hamiltonian over the phase fluctuations. We comment that the tunneling amplitude t can be obtained as a function of the barrier strength Λ by making use of the results introduced in Ref.[142]: $t/L = \Gamma(1+K)\Gamma(1+1/K)^K(\hbar\omega_c)^{1+K}(\Lambda/L)^{-K}$, where $\hbar\omega_c \sim NE_0$.

We summarize the results of this section by stating that with help of Luttinger liquid theory the Ω -dependent part of the ground state of the many-body bosonic system is obtained in the limits of weak and strong barriers.

A.5 Gross-Pitaevskii equation

Our starting point is the second-quantized Hamiltonian:

$$\begin{aligned}\hat{H} &= \int d\mathbf{x} \hat{\Psi}^\dagger(\mathbf{x}) \left(-\frac{\hbar^2}{2m} \nabla^2 + V_{ex}(\mathbf{x}) \right) \hat{\Psi}(\mathbf{x}) \\ &+ \frac{g}{2} \int d\mathbf{x} \hat{\Psi}^\dagger(\mathbf{x}) \hat{\Psi}^\dagger(\mathbf{x}) \hat{\Psi}(\mathbf{x}) \hat{\Psi}(\mathbf{x}),\end{aligned}\quad (\text{A.34})$$

where $V_{ex}(\mathbf{x})$ is the external trapping potential and the bosonic operators $\hat{\Psi}(\mathbf{x})$ obey to bosonic commutation relations. The main idea for a mean-field description of a dilute Bose gas was formulated by Bogoliubov. The key point consists in separating of the bosonic field operator in condensate fraction and the depletion out of the condensate for the system which has single-particle state which is macroscopically occupied. We introduce the field operator as a sum of its average value and the fluctuations around the mean value:

$$\hat{\Psi}(\mathbf{x}, t) = \Phi(\mathbf{x}, t) + \hat{\xi}(\mathbf{x}, t) \quad (\text{A.35})$$

A.5. Gross-Pitaevskii equation

here we are using the Heisenberg representation of the field operators. Here $\Phi(\mathbf{x}, t) = \langle \hat{\Psi}(\mathbf{x}, t) \rangle$, and similar to the Bogoliubov theory $|\Phi(\mathbf{x}, t)|^2 = n(\mathbf{x}, t)$. The function $\Phi(\mathbf{x}, t)$ has a meaning of the order parameter and its called wave function of the condensate. It is interesting to notice that Bose-Einstein condensation can be defined as a non vanishing long range order for the one-body density matrix $\rho_1(\mathbf{x}, \mathbf{y}) = \langle \hat{\Psi}^\dagger(\mathbf{x}, t) \hat{\Psi}(\mathbf{y}, t) \rangle$. It turns out that Eq. (A.35) implies the following condition: $\rho_1(\mathbf{x}, \mathbf{y}) = \Phi^*(\mathbf{x}, t) \Phi(\mathbf{y}, t) \rightarrow \text{const}$ when $|\mathbf{x} - \mathbf{y}| \rightarrow \infty$. However this definition is going to break down for the finite systems, and in that case condensate wave function can be obtained as the eigenfunction of the largest eigenvalue N_0 (which should be of the order of N for the Bose-condensed system) of the the $\rho_1(\mathbf{x}, \mathbf{y})$ [143]. This two definitions represent two main characteristics of Bose-Einstein condensate: spreading of the coherence length over the whole system, and having macroscopically occupied single-particle state. In the next step of the derivation we use the Heisenberg equation for the bosonic field:

$$\begin{aligned} i\hbar \frac{\partial \hat{\Psi}(\mathbf{x}, t)}{\partial t} &= [\hat{\Psi}(\mathbf{x}, t), \hat{H}] \\ &= \left(-\frac{\hbar^2}{2m} \nabla^2 + V_{ex}(\mathbf{x}) \right) \hat{\Psi}(\mathbf{x}) + \frac{g}{2} \hat{\Psi}^\dagger(\mathbf{x}) \hat{\Psi}(\mathbf{x}) \hat{\Psi}(\mathbf{x}) \end{aligned} \quad (\text{A.36})$$

where we have used the following commutation relation $[\hat{\Psi}^\dagger(\mathbf{x}), \hat{\Psi}^\dagger(\mathbf{y})] = \delta(x - y)$. When system has a macroscopically occupied single particle state it is expected that depletion term $\hat{\xi}(\mathbf{x}, t)$ is small. In that case $\hat{\Psi}(\mathbf{x}, t)$ can be substituted with $\Phi(\mathbf{x}, t)$ in Eq. (A.37) and the obtained equation is called Gross-Pitaevskii equation:

$$i\hbar \frac{\partial \hat{\Psi}(\mathbf{x}, t)}{\partial t} = \left(-\frac{\hbar^2}{2m} \nabla^2 + V_{ex}(\mathbf{x}) \right) \Phi(\mathbf{x}, t) + g |\Phi(\mathbf{x}, t)|^2 \Phi(\mathbf{x}, t) \quad (\text{A.37})$$

Appendix A. Appendix

This equation is satisfied for the systems with the s-wave scattering length much smaller than the average distance between atoms and the number of atoms in the condensate should be of the order of the total number of atoms in the system. Applicability of the Gross-Pitaveskii equation for the 1D systems is a delicate question which is related to the question whether Bose-condensates can be obtained for 1 dimensional systems. First question is whether it is possible to have macroscopically occupied single particle mode for the finite and zero temperature 1D systems. As it was demonstrated by Hohenberg[144] by obtaining Shwartz type inequality, the momentum distribution has infrared divergence of the form $1/k^2$ for the case of the finite temperature, and it was also demonstrated by Pitaveskii and Stringari[145] that in the limit of $T = 0$ that divergence is of the form $1/k$. As a consequence, number of particles is macroscopic both in the condensate and out of the condensate which brings a contradiction. We conclude that for a homogeneous atomic gas can not be in the Bose-condensed phase. However quasi off diagonal long range order can exist for the same systems due to phonon like dispersion relation. As it was shown in the section on Luttinger liquid in the limit of weak interactions $K \gg 1$ one body density matrix decays very slowly in the limit of large distances. All these discussions were done for the infinite systems. It turns out that finite systems can have a macroscopically occupied single-particle ground state in experimentally accessible interval of temperatures and thus Gross-Pitaveskii equation can be applied for obtaining qualitative information about the system.

APPENDIX B

Appendix

B.1 Peierls substitution for the Bose-Hubbard ladder model

In this appendix we review the 'Peierls substitution' in the Bose-Hubbard ladder, corresponding to applying of two different 'magnetic fluxes' to the two-ring lattice system (see Eq.(3.10)).

The hopping element t can be expressed through Wannier functions $\phi(\mathbf{x} - \mathbf{R}_i)$ and single particle Hamiltonian h_1 in the subsequent form:

$$t_0 = \int d\mathbf{x}^3 \phi^*(\mathbf{x} - \mathbf{R}_i) h_1 \phi(\mathbf{x} - \mathbf{R}_{i+1}), \quad (\text{B.1})$$

The Wannier functions $\phi(\mathbf{x} - \mathbf{R}_i)$ are localized around \mathbf{R}_i lattice sites. In the absence of 'electromagnetic fields' the single particle Hamiltonian is given by

$$h_1 = \frac{\mathbf{p}^2}{2m} + V(\mathbf{x}), \quad (\text{B.2})$$

where the first term is kinetic energy and second term is a one-body potential energy. Once the synthetic gauge field $\mathbf{A}(\mathbf{x}, t)$ is generated we can take it into account by substitution $\mathbf{p} \rightarrow \mathbf{p} - \mathbf{A}(\mathbf{x}, t)$ in the single-particle Hamiltonian. We can rewrite the hopping element in the presence of the

synthetic gauge field in the following form:

$$t = \int dx^3 \tilde{\phi}^*(\mathbf{x} - \mathbf{R}_i) h_1 \tilde{\phi}(\mathbf{x} - \mathbf{R}_{i+1}), \quad (\text{B.3})$$

where $\tilde{\phi}(\mathbf{x} - \mathbf{R}_i) = e^{-i\Lambda(\mathbf{x}, t)} \phi^*(\mathbf{x} - \mathbf{R}_i)$ with $\Lambda(\mathbf{x}, t) = \int_{\mathbf{x}_0}^{\mathbf{x}} \mathbf{A}(\mathbf{x}, t) d\mathbf{x}$, where \mathbf{x}_0 is an arbitrary point. Assuming that $\mathbf{A}(\mathbf{x}, t)$ is slowly varying function on an atomic scale

$$\tilde{\phi}(\mathbf{x} - \mathbf{R}_i) \approx e^{-i\Lambda(\mathbf{R}_i, t)} \phi^*(\mathbf{x} - \mathbf{R}_i), \quad (\text{B.4})$$

By substituting Eq.(B.4) in Eq.(B.3) we finally get

$$t = e^{i\Phi} t_0, \quad \Phi = \int_{\mathbf{R}_i}^{\mathbf{R}_{i+1}} \mathbf{A}(\mathbf{x}, t) d\mathbf{x} \quad (\text{B.5})$$

The idea, that all the effect of electromagnetic field in the lattice can be absorbed in the hopping matrix element is called Peierls substitution. We would like to emphasize, that the inter-ring hopping element g is not affected by the Peierls substitution because the synthetic gauge field is assumed to have components longitudinal to the rings only.

B.2 Effective qubit dynamics for the AQUID

In this section, we demonstrate how the effective phase dynamics indeed defines a qubit. To this end, we elaborate on the imaginary-time path integral of the partition function of the model Eq.(3.7) in the limit of small fluctuations of the number of bosons at each site. We first perform a local gauge transformation $a_l \rightarrow a_l e^{il\Phi}$ eliminating the contribution of the magnetic field everywhere except at the weak link site where the phase slip is concentrated [101]. In the regime under scrutiny, the dynamics is

B.2. Effective qubit dynamics for the AQUID

governed by the Quantum-Phase Hamiltonian[146]

$$H_{QP} = \sum_{i=0}^{N-2} [U n_i^2 - J \cos(\phi_{i+1}, -\phi_i)] + \quad (B.6)$$

$$[U n_{N-1}^2 - J' \cos(\phi_0, -\phi_{N-1}, -\Phi)] \quad (B.7)$$

where n_i and ϕ_i are conjugated variables and with $J = t \langle n \rangle$ and $J' = t' \langle n \rangle$.

The partition function of the model Eq.(3.10) is

$$Z = Tr(e^{-\beta H_{BH}}) \propto \int D[\{\phi_i\}] e^{-S[\{\phi_i\}]} \quad (B.8)$$

where the effective action is

$$\begin{aligned} S[\{\phi_i\}] &= \int d\tau \sum_{i=0}^{N-2} \left[\frac{1}{U} (\dot{\phi}_i)^2 - J \cos(\phi_{i+1}, -\phi_i) \right] \\ &+ \left[\frac{1}{U} (\dot{\phi}_{N-1})^2 - J' \cos(\phi_0, -\phi_{N-1}, -\Phi) \right] \end{aligned} \quad (B.9)$$

Because of the gauge transformations, the phase slip is produced only at the boundary. We define $\theta \doteq \phi_{N-1}, -\phi_0$. The goal, now, is to integrate out the phase variables in the bulk. To achieve the task, we observe that in the phase-slips-free-sites the phase differences are small, so the harmonic approximation can be applied:

$$\sum_{i=0}^{N-2} \cos(\phi_{i+1} - \phi_i) \simeq \sum_{i=0}^{N-2} \frac{(\phi_{i+1} - \phi_i)^2}{2}. \quad (B.10)$$

In order to facilitate the integration in the bulk phases, we express the single ϕ_0 and ϕ_{N-1} as: $\phi_0 = \tilde{\phi}_0 + \theta/2$, $\phi_{N-1} = \tilde{\phi}_0 - \theta/2$. We observe that the sum of the quadratic terms above involves $N - 1$ fields with periodic boundary conditions: $\{\tilde{\phi}_0, \phi_1, \dots, \phi_{N-2}\} \equiv \{\psi_0, \psi_1, \dots, \psi_{N-2}\}$, $\psi_{N-1} =$

Appendix B. Appendix

ψ_0 . Therefore

$$\sum_{i=0}^{N-2} (\phi_{i+1} - \phi_i)^2 = \sum_{i=0}^{N-2} (\psi_{i+1} - \psi_i)^2 + \frac{1}{2}\theta^2 + \theta(\psi_{N-2} - \psi_1). \quad (\text{B.11})$$

The effective action, $S[\{\phi_i\}]$, can be split into two terms $S[\{\phi_i\}] = S_1[\theta] + S_2[\{\psi_i\}]$ with

$$S_1[\theta] = \int d\tau \left[\frac{1}{U}(\dot{\theta})^2 + \frac{J}{2}\theta^2 - J' \cos(\theta - \Phi) \right] \quad (\text{B.12})$$

$$S_2[\{\psi_i\}, \theta] = \int d\tau \left[\frac{1}{U}(\dot{\psi}_0)^2 + \sum_{i=0}^{N-2} \left[\frac{1}{U}(\dot{\psi}_i)^2 + \frac{J}{2}(\psi_{i+1} - \psi_i)^2 \right] \right] \\ + \int d\tau J\theta(\psi_{N-2} - \psi_1) \quad (\text{B.13})$$

The integration of the fields ψ_i proceeds according to the standard methods (see [102]). The fields that need to be integrated out are expanded in Fourier series (N is assumed to be even): $\psi_l = \psi_0 + (-)^l \psi_{N/2} + \sum_{k=1}^{(N-2)/2} \left(\psi_k e^{\frac{2\pi i k l}{N-1}} + c.c. \right)$, with $\psi_k = a_k + i b_k$. The coupling term in Eq. (B.27) involves only the imaginary part of ψ_k : $\psi_{N-2} - \psi_1 = \sum_k b_k \zeta_k$, being $\zeta_k = \frac{4}{\sqrt{N-1}} \sin\left(\frac{2\pi k}{N-1}\right)$. Therefore:

$$S_2[\{\psi_i\}, \theta] = \int d\tau \frac{1}{U} \sum_k (\dot{a}_k)^2 + \omega_k^2 a_k^2 + \int d\tau \frac{1}{U} \sum_k (\dot{b}_k)^2 + \omega_k^2 b_k^2 + J U \zeta_k \theta b_k \quad (\text{B.14})$$

where $\omega_k = \sqrt{2JU \left[1 - \cos\left(\frac{2\pi k}{N-1}\right) \right]}$. The integral in $\{a_k\}$ leads to a Gaussian path integral; it does not contain the interaction with θ , and therefore brings a prefactor multiplying the effective action, that does not affect the dynamics. The integral in $\{b_k\}$ involves the inter-

B.2. Effective qubit dynamics for the AQUID

action and therefore leads to a non local kernel in the imaginary time: $\int d\tau d\tau' \theta(\tau) G(\tau - \tau') \theta(\tau')$. The explicit form of $G(\tau - \tau')$ is obtained by expanding $\{b_k\}$ and θ in Matsubara frequencies ω_l . The corresponding Gaussian integral yields to the

$$\int D[b_k] e^{-\int d\tau S_{02}} \propto \exp \left(-\beta U J^2 \sum_{l=0}^{\infty} \tilde{Y}(\omega_l) |\theta_l|^2 \right) \quad (\text{B.15})$$

with $\tilde{Y}(\omega_l) = \sum_{k=1}^{(N-2)/2} \frac{\zeta_k^2}{\omega_k^2 + \omega_l^2}$. The $\tau = \tau'$ term is extracted by summing and subtracting $\tilde{Y}(\omega_l = 0)$; this compensates the second term in Eq.(B.26).

The effective action finally reads as:

$$S_{eff} = \int_0^\beta d\tau \left[\frac{1}{2U} \dot{\theta}^2 + U(\theta) \right] - \frac{J}{2U(N-1)} \sum \int d\tau d\tau' \theta(\tau) G(\tau - \tau') \theta(\tau') \quad (\text{B.16})$$

where

$$U(\theta) \doteq \frac{J}{N-1} (\theta - \Phi)^2 - J' \cos \theta. \quad (\text{B.17})$$

The kernel in the non-local term is given by

$$G(\tau) = \sum_{l=0}^{\infty} \sum_{k=1}^{\frac{N-2}{2}} \frac{\omega_l^2 (1 + \cos[\frac{2\pi k}{N-1}])}{2JU(1 - \cos[\frac{2\pi k}{N-1}]) + \omega_l^2} e^{i\omega_l \tau}. \quad (\text{B.18})$$

The external bath vanishes in the thermodynamic limit and the effective action reduces to the Caldeira-Leggett one [102]. Finally it is worth noting that the case of a single junction needs a specific approach but it can be demonstrated consistent with Eq.(B.16).

B.3 Effective qubit dynamics for a double-ring setup

In this section, we demonstrate that the effective phase dynamics of the system given by Bose-Hubbard ladder Hamiltonian is indeed defines a qubit. To this end, we elaborate on the imaginary-time path integral of the partition function of the model Eq.(3.9) in the limit of small fluctuations of the number of bosons at each lattice site. We first perform a local gauge transformation $a_l \rightarrow a_l e^{il\Phi_a}$, $b_l \rightarrow b_l e^{il\Phi_b}$, eliminating the contribution of the magnetic field everywhere except at a given site of the ring (twisted boundary conditions[101]). In the regime under scrutiny, the partition function of the model Eq.(3.9) is [6, 146]

$$Z = Tr (e^{-\beta H_{BH}}) \propto \int D[\{\phi_i\}] e^{-S[\{\phi_i\}]} \quad (\text{B.19})$$

where the effective action is

$$S[\{\phi_i\}] = S_0[\{\phi_i\}] + S_{int}[\{\phi_i\}] \quad (\text{B.20})$$

$$\begin{aligned} S_0[\{\phi_i\}] &= \int_0^\beta d\tau \sum_{\substack{i=0 \\ \alpha=\{a,b\}}}^{N-2} \left[\frac{1}{U} (\dot{\phi}_{i,\alpha})^2 - E_J \cos(\phi_{i+1,\alpha} - \phi_{i,\alpha}) \right] \\ &\quad + \int_0^\beta d\tau \sum_{\alpha=\{a,b\}}^{N-2} \left[\frac{1}{U} (\dot{\phi}_{N-1,\alpha})^2 - E_J \cos(\phi_{0,\alpha} - \phi_{N-1,\alpha} - \Phi_\alpha) \right] \end{aligned} \quad (\text{B.21})$$

$$S_{int}[\{\phi_i\}] = -E'_J \int_0^\beta d\tau \sum_{i=0}^{N-1} \cos \left(\phi_{i,a} - \phi_{i,b} - \frac{\Phi_a - \Phi_b}{N} i \right) \quad (\text{B.22})$$

with $E_J = t\langle n \rangle$ and $E'_J = g\langle n \rangle$.

Because of the gauge transformations, the phase slip is produced only at the boundary. We define $\theta_\alpha \doteq \phi_{N-1,\alpha} - \phi_{0,\alpha}$. The goal now is to integrate

B.3. Effective qubit dynamics for a double-ring setup

out the phase variables in the bulk. Assuming that the two rings are weakly coupled and that $U/E_J \ll 1$, the bulk variables are not involved in the inter-ring tunneling term because we can take $\phi_{i,a} \approx \phi_{i,b}$ everywhere except at the boundary:

$$\sum_{i=0}^{N-1} \cos \left(\phi_{i,a} - \phi_{i,b} - \frac{\Phi_a - \Phi_b}{N} i \right) = \sum_{i=0}^{N-2} \cos \left(\frac{\Phi_a - \Phi_b}{N} i \right) + \cos \left(\theta_a - \theta_b - \frac{\Phi_a - \Phi_b}{N} (N-1) \right) \quad (\text{B.23})$$

where, without loss of generality, we can assume $\phi_{0,a} \equiv \phi_{0,b}$. Therefore the non-trivial path integration corresponds to $S_0[\{\phi_i\}]$ only. To achieve the task we observe that in the phase-slips-free-sites the phase differences are small, so the harmonic approximation can be applied:

$$\sum_{i=0}^{N-1} \cos(\phi_{i+1,\alpha} - \phi_{i,\alpha}) \mapsto \cos(\theta_\alpha - \Phi_\alpha) - \sum_{i=0}^{N-2} \frac{(\phi_{i+1,\alpha} - \phi_{i,\alpha})^2}{2} . \quad (\text{B.24})$$

In order to facilitate the integration in the bulk phases, we express the single $\phi_{0,\alpha}$ and $\phi_{N-1,\alpha}$ as: $\phi_{0,\alpha} = \tilde{\phi}_{0,\alpha} + \theta_\alpha/2$, $\phi_{N-1,\alpha} = \tilde{\phi}_{0,\alpha} - \theta_\alpha/2$. We observe that the sum of the quadratic terms above involves $N-1$ fields with periodic boundary conditions: $\{\tilde{\phi}_{0,\alpha}, \phi_{1,\alpha}, \dots, \phi_{N-2,\alpha}\} \equiv \{\psi_{0,\alpha}, \psi_{1,\alpha}, \dots, \psi_{N-2,\alpha}\}$, $\psi_{N-1,\alpha} = \psi_{0,\alpha}$. Therefore,

$$\sum_{i=0}^{N-2} (\phi_{i+1,\alpha} - \phi_{i,\alpha})^2 = \sum_{i=0}^{N-2} (\psi_{i+1,\alpha} - \psi_{i,\alpha})^2 + \frac{1}{2} \theta_\alpha^2 + \theta_\alpha (\psi_{N-2,\alpha} - \psi_{1,\alpha}) . \quad (\text{B.25})$$

The effective action, $S_0[\{\phi_i\}]$, can be split into two terms $S_0[\{\phi_i\}] =$

Appendix B. Appendix

$S_{01}[\theta_\alpha] + S_{02}[\{\psi_{i\alpha}\}]$ with

$$S_{01}[\theta_\alpha] = \int_0^\beta d\tau \left[\frac{1}{U} (\dot{\theta}_\alpha)^2 + \frac{E_J}{2} \theta_\alpha^2 - E_J \cos(\theta_\alpha - \Phi_\alpha) \right] \quad (\text{B.26})$$

$$\begin{aligned} S_{02}[\{\psi_{i,\alpha}\}, \theta_\alpha] &= \int_0^\beta d\tau \left\{ \frac{1}{U} (\dot{\psi}_{0,\alpha})^2 + \sum_{i=0}^{N-2} \left[\frac{1}{U} (\dot{\psi}_{i,\alpha})^2 + \frac{E_J}{2} (\psi_{i+1,\alpha} - \psi_{i,\alpha})^2 \right] \right\} \\ &+ \int_0^\beta d\tau E_J \theta_\alpha (\psi_{N-2,\alpha} - \psi_{1,\alpha}) \end{aligned} \quad (\text{B.27})$$

The integration of the fields $\psi_{i,\alpha}$ proceeds according to the standard methods (see [102]). The fields that need to be integrated out are expanded in Fourier series (N is assumed to be even): $\psi_{l,\alpha} = \frac{1}{\sqrt{N-1}} [\psi_{0,\alpha} + (-)^l \psi_{N/2,\alpha} + \sum_{k=1}^{(N-2)/2} (\psi_{k,\alpha} e^{\frac{2\pi i k l}{N-1}} + c.c.)]$, with $\psi_{k,\alpha} = a_{k,\alpha} + i b_{k,\alpha}$. The coupling term in Eq. (B.27) involves only the imaginary part of $\psi_{k,\alpha}$: $\psi_{N-2,\alpha} - \psi_{1,\alpha} = \sum_k b_{k,\alpha} \zeta_k$, being $\zeta_k = \frac{4}{\sqrt{N-1}} \sin\left(\frac{2\pi k}{N-1}\right)$. Therefore:

$$\begin{aligned} S_{02}[\{\psi_{i,\alpha}\}, \theta_\alpha] &= \int_0^\beta d\tau \frac{1}{U} \sum_k [(\dot{a}_{k,\alpha})^2 + \omega_k^2 a_{k,\alpha}^2] \\ &+ \int_0^\beta d\tau \frac{1}{U} \sum_k [(\dot{b}_{k,\alpha})^2 + \omega_k^2 b_{k,\alpha}^2 + E_J U \zeta_k \theta_\alpha b_{k,\alpha}] \end{aligned} \quad (\text{B.28})$$

where $\omega_k = \sqrt{2E_J U [1 - \cos(\frac{2\pi k}{N-1})]}$. The integral in $\{a_{k,\alpha}\}$ leads to a Gaussian path integral; it does not contain the interaction with θ_α , and therefore brings a prefactor multiplying the effective action, that does not affect the dynamics. The integral in $\{b_{k,\alpha}\}$ involves the interaction and therefore leads to a non local kernel in the imaginary time: $\int d\tau d\tau' \theta_\alpha(\tau) G(\tau - \tau') \theta_\alpha(\tau')$. The explicit form of $G(\tau - \tau')$ is obtained by expanding $\{b_{k,\alpha}\}$ and θ_α in Matsubara frequencies ω_l . The corresponding

B.3. Effective qubit dynamics for a double-ring setup

Gaussian integral yields to the

$$\int D[b_{k,\alpha}] e^{-\int_0^\beta d\tau S_{02}} \propto \exp \left(-\beta U E_J^2 \sum_{l=0}^{\infty} \tilde{Y}(\omega_l) |\theta_l|^2 \right) \quad (\text{B.29})$$

with $\tilde{Y}(\omega_l) = \sum_{k=1}^{(N-2)/2} \frac{\zeta_k^2}{\omega_k^2 + \omega_l^2}$. The $\tau = \tau'$ term is extracted by summing and subtracting $\tilde{Y}(\omega_l = 0)$; this compensates the second term in Eq.(B.26).

The effective action finally reads as

$$\begin{aligned} S_{eff} &= \int_0^\beta d\tau \left[\frac{1}{2U} \sum_{\alpha=a,b} \dot{\theta}_\alpha^2 + U(\theta_a, \theta_b) \right] \\ &- \frac{E_J}{2U(N-1)} \sum_{\alpha=a,b} \int_0^\beta d\tau d\tau' \theta_\alpha(\tau) G_\alpha(\tau - \tau') \theta_\alpha(\tau') \end{aligned} \quad (\text{B.30})$$

where

$$\begin{aligned} U(\theta_a, \theta_b) \doteq & \sum_{\alpha=a,b} \left[\frac{E_J}{2(N-1)} (\theta_\alpha - \Phi_\alpha)^2 - E_J \cos(\theta_\alpha) \right] \\ & - E'_J \cos[\theta_a - \theta_b - \frac{N-2}{N}(\Phi_a - \Phi_b)] . \end{aligned} \quad (\text{B.31})$$

We observe that for large N , the potential $U(\theta_a, \theta_b)$ provides the effective phase dynamics of Josephson junctions flux qubits realized by Mooij *et al.* (large N corresponds to large geometrical inductance of flux qubit devices) [64]. In that article, the landscape was thoroughly analyzed. The qubit is realized by superposing the two states $|\theta_1\rangle$ and $|\theta_2\rangle$ corresponding to the minima of $U(\theta_a, \theta_b)$. The degeneracy point is achieved at $\Phi_b - \Phi_a = \pi$ (See Fig.6.1). We comment that the ratio E'_J/E_J controls the relative size of the energy barriers between minima intra- and minima inter-'unit cells' of the (θ_a, θ_b) phase space, and therefore is important for designing the qubit. In our system E'_J/E_J can be fine tuned with the scheme shown in Fig.2.13.

Appendix B. Appendix

The kernel in the non-local term is given by $G_a(\tau) = G_b(\tau) = G(\tau)$, with:

$$G(\tau) = \sum_{l=0}^{\infty} \sum_{k=1}^{\frac{N-2}{2}} \frac{\omega_l^2 (1 + \cos[\frac{2\pi k}{N-1}])}{2E_J U(1 - \cos[\frac{2\pi k}{N-1}]) + \omega_l^2} e^{i\omega_l \tau}. \quad (\text{B.32})$$

The external bath vanishes in the thermodynamic limit and the effective action reduces to the Caldeira-Leggett one [102, 147].

B.4 Solution in terms of elliptic functions

As it was shown in Sect. 6.3, the dynamics of the population imbalance and the phase difference of the condensates in the two coupled rings is given by

$$\frac{\partial Z}{\partial \tilde{s}} = -\sqrt{1 - Z^2} \sin \Theta \quad (\text{B.33})$$

$$\frac{\partial \Theta}{\partial \tilde{s}} = \Delta + \lambda \rho Z + \frac{Z}{\sqrt{1 - Z^2}} \cos \Theta \quad (\text{B.34})$$

In this appendix we discuss the analytical solutions of the equations above, for the two different cases: $\Delta = 0$ and $\Delta \neq 0$.

The Eqs.(B.33) and (B.34) can be derived from the Hamiltonian

$$H(Z(\tilde{s}), \Theta(\tilde{s})) = \frac{\lambda \rho Z^2}{2} + \Delta Z - \sqrt{1 - Z^2} \cos \Theta = H_0, \quad (\text{B.35})$$

where Z and Θ are canonically conjugate variables. Indeed, $H(Z(t), \Theta(t)) = H(Z(0), \Theta(0)) = H_0$ because the energy of the system is conserved. Combining Eqs.(B.33) and (B.35) Θ can be eliminated, obtaining

$$\dot{Z}^2 + [\frac{\lambda \rho Z^2}{2} + \Delta Z - H_0]^2 = 1 - Z^2, \quad (\text{B.36})$$

B.4. Solution in terms of elliptic functions

that is solved by quadratures:

$$\frac{\lambda \varrho \tilde{s}}{2} = \int_{Z(0)}^{Z(\tilde{s})} \frac{dZ}{\sqrt{f(Z)}} \quad (\text{B.37})$$

where $f(Z)$ is the following quartic equation

$$f(Z) = \left(\frac{2}{\lambda\rho}\right)^2 (1 - Z^2) - \left[Z^2 + \frac{2Z\Delta}{\lambda\rho} - \frac{2H_0}{\lambda\rho}\right]^2 \quad (\text{B.38})$$

There are two different cases: $\Delta = 0$ and $\Delta \neq 0$.

I) $\Delta = 0$. – In this case the solution for the $Z(t)$ can be expressed in terms of 'cn' and 'dn' Jacobian elliptic functions as([33]):

$$\begin{aligned} Z(\tilde{s}) &= C \operatorname{cn}[(C\lambda\rho/k(\tilde{s} - \tilde{s}_0), k)] \quad \text{for } 0 < k < 1 \\ &= C \operatorname{sech}(C\lambda\rho(\tilde{s} - \tilde{s}_0)), \quad \text{for } k = 1 \\ &= C \operatorname{dn}[(C\lambda\rho/k(\tilde{s} - \tilde{s}_0), 1/k)] \quad \text{for } k > 1; \end{aligned} \quad (\text{B.39})$$

$$k = \left(\frac{C\lambda\rho}{\sqrt{2}\zeta(\lambda\rho)}\right)^2 = \frac{1}{2} \left[1 + \frac{(H_0\lambda\rho - 1)}{(\lambda\rho)^2 + 1 - 2H_0\lambda\rho}\right], \quad (\text{B.40})$$

where

$$\begin{aligned} C^2 &= \frac{2}{(\lambda\rho)^2} ((H_0\lambda\rho - 1) + \zeta^2), \\ \alpha^2 &= \frac{2}{(\lambda\rho)^2} (\zeta^2 - (H_0\lambda\rho - 1)), \\ \zeta^2(\lambda\rho) &= 2\sqrt{(\lambda\rho)^2 + 1 - 2H_0\lambda\rho}, \end{aligned} \quad (\text{B.41})$$

and \tilde{s}_0 fixing $Z(0)$. Jacobi functions are defined in terms of the incomplete elliptic integral of the first kind $F(\phi, k) = \int_0^\phi d\theta (1 - k \sin^2 \theta)^{-1/2}$ by the following expressions: $\operatorname{sn}(u|k) = \sin \phi$, $\operatorname{cn}(u|k) = \cos \phi$ and $\operatorname{dn}(u|k) = (1 - k \sin^2 \phi)^{1/2}$ [148]. The Jacobian elliptic functions $\operatorname{sn}(u|k)$, $\operatorname{cn}(u|k)$ and $\operatorname{dn}(u|k)$ are periodic in the argument u with period $4K(k)$, $4K(k)$ and

Appendix B. Appendix

$2K(k)$, respectively, where $K(k) = F(\pi/2, k)$ is the complete elliptic integral of the first kind. For small elliptic modulus $k \simeq 0$ such functions behave as trigonometric functions; for $k \simeq 1$ they behave as hyperbolic functions. Accordingly, the character of the solution of Eqs.(B.33) and (B.34) can be oscillatory or exponential, depending on k . For $k \ll 1$, $cn(u|k) \approx \cos u + 0.25k(u - \sin(2u)/2) \sin u$ is almost sinusoidal and the population imbalance is oscillating around zero average value. When k increases, the oscillations become non-sinusoidal and for $1-k \ll 1$ the time evolution is non-periodic: $cn(u|k) \approx \sec u - 0.25(1-k)(\sinh(2u)/2 - u) \tanh u \sec u$. From the last expression we can see that at $k = 1$, $cn(u|k) = \sec u$ so oscillations are exponentially suppressed and $Z(\tilde{s})$ taking 0 asymptotic value. For the values of the $k > 1$ such that $[1-1/k] \ll 1$ and $Z(s)$ is still non-periodic and is given by: $dn(u|1/k) \approx \sec u + 0.25(1-1/k)(\sinh(2u)/2 + u) \tanh u \sec u$. Finally when $k \gg 1$ then the behavior switches to sinusoidal again, but $Z(\tilde{s})$ does oscillates around a non-zero average: $dn(u|1/k) \approx 1 - \sin^2 u/2k$. This phenomenon accounts for the MQST.

The periods of oscillations in the regimes considered above result to be

$$\begin{aligned} \tau &= \frac{4kK(k)}{C\lambda\rho} \quad \text{for } 0 < k < 1, \\ &= \log(4/\sqrt{1-k}) \quad \text{for } k = 1, \\ &= \frac{2K(1/k)}{C\lambda\rho} \quad \text{for } k > 1 \end{aligned} \tag{B.42}$$

For $k \rightarrow 1$ the period becomes infinite and diverging logarithmically.

$\Pi)\Delta \neq 0$.– In this case $Z(s)$ is expressed in terms of the Weierstrass elliptic function([128, 33]):

$$Z(\tilde{s}) = Z_1 + \frac{f'(Z_1)/4}{\varrho(\frac{\lambda\rho}{2}(\tilde{s} - \tilde{s}_0); g_2, g_3) - \frac{f''(Z_1)}{24}} \tag{B.43}$$

B.4. Solution in terms of elliptic functions

where $f(Z)$ is given by an expression (B.38), Z_1 is a root of quartic $f(Z)$ and $\tilde{s}_0 = (2/\lambda\rho) \int_{Z_1}^{Z(0)} \frac{dz'}{\sqrt{f(z')}}.$ For $\sin \Theta_0 = 0$ (which is the case discussed in the text), $Z_1 = Z_0$ and consequently $s_0 = 0.$ The Weierstrass elliptic function can be given as the inverse of an elliptic integral $\varrho(u; g_2, g_3) = y,$ where

$$u = \int_y^\infty \frac{ds}{\sqrt{4s^3 - g_2 s - g_3}}. \quad (\text{B.44})$$

The constants g_2 and g_3 are the characteristic invariants of $\varrho:$

$$\begin{aligned} g_2 &= -a_4 - 4a_1a_3 + 3a_2^2 \\ g_3 &= -a_2a_4 + 2a_1a_2a_3 - a_2^3 + a_3^2 - a_1^2a_4, \end{aligned} \quad (\text{B.45})$$

where the coefficients a_i , where $i = 1, \dots, 4,$ are given as

$$\begin{aligned} a_1 &= -\frac{\Delta}{\lambda\rho}; a_2 = \frac{2}{3(\lambda\rho)^2}(\lambda\rho H_0 - (\Delta^2 + 1)) \\ a_3 &= \frac{2H_0\Delta}{(\lambda\rho)^2}; a_4 = \frac{4(1 - H_0^2)}{(\lambda\rho)^2} \end{aligned} \quad (\text{B.46})$$

In the present case $\Delta \neq 0,$ the discriminant

$$\delta = g_2^3 - 27g_3^2 \quad (\text{B.47})$$

of the cubic $h(y) = 4y^3 - g_2y - g_3$ governs the behavior of the Weierstrass elliptic functions (we contrast with the case $\Delta = 0,$ where the dynamics is governed by the elliptic modulus $k).$

At first we consider the case $\delta = 0.$

If $g_2 < 0, g_3 > 0$ then ([148])

$$Z(\tilde{s}) = Z_1 + \frac{f'(Z_1)/4}{c + 3c \sinh^{-2} [\frac{\sqrt{3}\bar{c}\lambda\rho}{2}(\tilde{s} - \tilde{s}_0)] - \frac{f''(Z_1)}{24}} \quad (\text{B.48})$$

Appendix B. Appendix

Namely, the oscillations of Z are exponentially suppressed and the population imbalance decay (if $Z_0 > 0$) or saturate (if $Z_0 < 0$) to the asymptotic value given by $Z(\tilde{s}) = Z_1 + \frac{f'(Z_1)/4}{c - f''(Z_1)/24}$.

If $g_2 > 0, g_3 > 0$ then([148])

$$Z(\tilde{s}) = Z_1 + \frac{f'(Z_1)/4}{-c + 3c \sin^{-2} [\frac{\sqrt{3c}\lambda\rho}{2}(\tilde{s} - \tilde{s}_0)] - \frac{f''(Z_1)}{24}} \quad (\text{B.49})$$

where $c = \sqrt{g_2/12}$. We see that the population imbalance oscillates around a non-zero average value $\bar{Z} \doteq Z_1 + \frac{f'(Z_1)/4}{2(2c - f''(Z_1)/24)}$, with frequency $\omega = 2g\sqrt{3c}\lambda\rho$.

We express the Weierstrass function in terms of Jacobian elliptic functions. This leads to significant simplification for the analysis of these regimes.

For $\delta > 0$, it results

$$Z(\tilde{s}) = Z_1 + \frac{f'(Z_1)/4}{e_3 + \frac{e_1 - e_3}{sn^2[\frac{\lambda\rho\sqrt{e_1 - e_3}}{2}(\tilde{s} - \tilde{s}_0), k_1]} - \frac{f''(Z_1)}{24}} \quad (\text{B.50})$$

where $k_1 = \frac{e_2 - e_3}{e_1 - e_3}$ and e_i are solutions of the cubic equation $h(y) = 0$.

In this case the population imbalance oscillates about the average value $\bar{Z} = Z_1 + \frac{f'(Z_1)/4}{2(e_1 - f''(Z_1)/24)}$.

The asymptotics of the solution is extracted through: $k \ll 1$, $sn(u|k) \approx \sin u - 0.25k(u - \sin(2u)/2)\cos u$. When k increases oscillations starting to become non-sinusoidal and when $1 - k \ll 1$ it becomes non-periodic and takes form: $cn(u|k) \approx \tanh u - 0.25(1 - k)(\sinh(2u)/2 - u)\sec^2 u$.

For $\delta < 0$ the following expression for $Z(s)$ is obtained:

$$Z(\tilde{s}) = Z_1 + \frac{f'(Z_1)/4}{e_2 + H_2 \frac{1+cn[\lambda\rho\sqrt{H_2}(\tilde{s} - \tilde{s}_0), k_2]}{1-cn[\lambda\rho\sqrt{H_2}(\tilde{s} - \tilde{s}_0), k_2]} - \frac{f''(Z_1)}{24}}, \quad (\text{B.51})$$

B.4. Solution in terms of elliptic functions

where $k_2 = 1/2 - \frac{3e_2}{4H_2}$ and $H_2 = \sqrt{3e_2^2 - \frac{g_2}{4}}$. The asymptotical behavior of the function $cn(u|k)$ has been discussed in the previous subsection. As it is seen from this expression $Z(\tilde{s})$ oscillates about the average value $\bar{Z} = Z_1 + \frac{f'(Z_1)/4}{2(e_2 - f''(Z_1)/24)}$.

The period of the oscillations of the $Z(\tilde{s})$ in this case is given by

$$\begin{aligned}\tau &= \frac{K(k_1)}{\lambda\rho\sqrt{e_1 - e_3}} \quad \text{for } \delta > 0, \\ &= \frac{K(k_2)}{\lambda\rho\sqrt{H_2}} \quad \text{for } \delta < 0.\end{aligned}\tag{B.52}$$

The inter-ring tunneling Josephson current is given by

$$I = \frac{\dot{Z}N_T}{2} = I_0\sqrt{1 - \bar{Z}^2} \sin\Theta,\tag{B.53}$$

APPENDIX C

Appendix

C.1 Momentum distribution for $\Lambda = 0$ and various interaction strengths

The signature of a non vanishing current flow along the ring lattice is a ring-shaped configuration of the momentum distribution (see C.2 for a derivation in the non-interacting limit). Fig. C.1 shows the predicted TOF images in the absence of the barrier for various interaction strengths. The perfect ring shape reflects angular momentum conservation at all interaction strengths, consistent with Leggett's theorem establishing that the persistent currents through a rotationally invariant system are not affected by the interactions. We note, however, that the detectability in the time-of-flight images is reduced at large interactions, due to the enhanced role of phase fluctuations.

C.2 Momentum distribution for $U = 0$ and weak barrier limit

In the noninteracting regime the many-body problem reduces to a single-particle one. In the absence of the barrier the Schrödinger equation, in polar coordinates and scaling the energies in units of $E_0 = \hbar^2/2mL^2$, with

Appendix C. Appendix

m being the particle mass, and L the system size, reads

$$\left(-i \frac{\partial}{\partial \theta} - \frac{\Omega}{2\pi} \right)^2 \psi(\theta) = E \psi(\theta) ,$$

where $\theta \in [0, 2\pi]$. The wavefunction for a state with defined angular momentum is a plane wave $\psi(\theta) = (1/\sqrt{2\pi})e^{in\theta}$, where $n \in \mathbb{Z}$ to satisfy periodic boundary conditions, and the corresponding spectrum is $E_n = (n - \Omega/2\pi)^2$. The momentum distribution then reads

$$\begin{aligned} n(\mathbf{k}) &= \int d\mathbf{x} \int d\mathbf{x}' e^{i\mathbf{k}\cdot(\mathbf{x}-\mathbf{x}')} \psi^*(\mathbf{x}) \psi(\mathbf{x}') \\ &\sim \left| \int_0^{2\pi} d\theta e^{i(k_x R \cos \theta + k_y R \sin \theta)} \psi^*(\theta) \right|^2 \\ &= |e^{im\gamma} J_m(|\mathbf{k}|R)|^2 = |J_n(|\mathbf{k}|R)|^2 , \end{aligned} \quad (\text{C.1})$$

where $R = L/2\pi$ is the ring radius, we have defined γ as $k_x = |\mathbf{k}| \sin \gamma$, $k_y = |\mathbf{k}| \cos \gamma$, and J_n is the n -th order Bessel function of the first kind. For $n = 0$ the momentum distribution is peaked at $\mathbf{k} = 0$, while for $n > 0$ it is ring shaped, with a radius that grows with n . In the presence of a

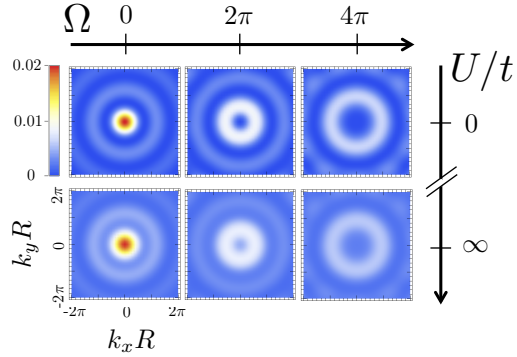


Figure C.1: Ground state momentum distribution (TOF) in the absence of the barrier, for different values of the Coriolis flux: $\Omega = 0, 2\pi, 4\pi$ and different regimes of interaction strength: non-interacting (upper line) and infinite interactions for $N = 5$ (lower line).

C.2. Momentum distribution for $U = 0$ and weak barrier limit

localized barrier of strength λ the Schrödinger equation becomes

$$\left(-i \frac{\partial}{\partial \theta} - \frac{\Omega}{2\pi} \right)^2 \psi(\theta) + \lambda \delta(\theta) \psi(\theta) = E \psi(\theta) .$$

The effect of the δ -barrier is to mix states with different angular momentum. For a small barrier we can reduce to the simplest case of mixing of states that differ by just one quantum of angular momentum, and apply degenerate perturbation theory. We write the Hamiltonian in the following form

$$H = \begin{pmatrix} E_n & \lambda/2\pi \\ \lambda/2\pi & E_{n+1} \end{pmatrix} ; \quad (\text{C.2})$$

the corresponding eigenvalues and eigenvectors reads:

$$\varepsilon_{1,2} = \frac{E_{n+1} + E_n}{2} \pm \frac{\sqrt{\delta E^2 + \lambda^2/\pi^2}}{2} ,$$

where $\delta E = E_{n+1} - E_n$, and

$$w_1 = \begin{pmatrix} \sin(\varphi/2) \\ \cos(\varphi/2) \end{pmatrix} , \quad w_2 = \begin{pmatrix} \cos(\varphi/2) \\ -\sin(\varphi/2) \end{pmatrix} ,$$

where

$$\cos^2(\varphi/2) = \frac{\sqrt{\delta E^2 + \lambda^2/\pi^2} - \delta E}{2\sqrt{\delta E^2 + \lambda^2/\pi^2}} . \quad (\text{C.3})$$

We then write the wavefunction as

$$\psi(\theta) = \frac{1}{\sqrt{2\pi}} \sin(\varphi/2) e^{in\theta} + \frac{1}{\sqrt{2\pi}} \cos(\varphi/2) e^{i(n+1)\theta} ,$$

where φ depends on λ and Ω .

The momentum distribution in this case becomes

$$\begin{aligned}
n(\mathbf{k}) &\sim \left| \int_0^{2\pi} d\theta e^{i(k_x R \cos \theta + k_y R \sin \theta)} \psi^*(\theta) \right|^2 \\
&= \left| \sin(\varphi/2) e^{in\gamma} J_n(|\mathbf{k}|R) + \cos(\varphi/2) e^{i(n+1)\gamma} J_{n+1}(|\mathbf{k}|R) \right|^2 \\
&= \sin^2(\varphi/2) J_n^2(|\mathbf{k}|R) + \cos^2(\varphi/2) J_{n+1}^2(|\mathbf{k}|R) \\
&\quad + 2 \sin(\varphi/2) \cos(\varphi/2) \cos(\gamma) J_n(|\mathbf{k}|R) J_{n+1}(|\mathbf{k}|R),
\end{aligned} \tag{C.4}$$

where an interference term, proportional to $\cos \gamma$, appears between the two states with defined angular momentum, giving rise to a 2π -periodic angular modulation of the ring shape found previously. This behavior is the same found in Fig. 5.1, where we observe an analogous modulation in the weak barrier and weak interaction case, that we can interpret than as direct consequence of the superposition of two states that differ by one quantum of angular momentum.

C.3 Derivation of the Energy gap with the WKB approximation

Here we are using a general expression, which is applicable to any double well potential [103], for the energy gap between the ground and first excited states to obtain the energy gap, at the frustration point $\Phi = \pi$, for the double well potential given by Eq.(4.4). This general result, which is correct when $V(0) = J' \gg E$, reads as:

$$\varepsilon = \frac{\omega_{eff}}{\pi} \exp [\mu \omega_{eff} x_0^2], \tag{C.5}$$

C.3. Derivation of the Energy gap with the WKB approximation

where $\omega_{eff} = \sqrt{V''(x_0)/\mu}$ is a frequency of the particle confined in "harmonic potential" (here we expand the potential around the position of the minimum x_0). Since our potential is not a simple function, we simplify it at first by going to the new variable $\tilde{\theta} = \theta - \pi$, and then by applying the Taylor expansion $\cos \tilde{\theta} = 1 - \tilde{\theta}^2/2 + \tilde{\theta}^2/4!$. In order to find the x_0 we solve the equation $V'(x_0) = 0$ and obtain that $x_0 = \sqrt{6(1 - 1/\delta)}$. In the next step we calculate $V''(x_0)$, and obtain that $V''(x_0) = 1 - 1/\delta$. After substituting expressions for x_0 and $V''(x_0)$ in Eq.(C.5) we recover the result given by Eq. (4.6).

APPENDIX D

Appendix

D.1 Infinite interaction limit of BH model:

$$U \rightarrow \infty$$

In the limiting case of infinite repulsive contact interaction between the particles ($U \rightarrow \infty$), the so-called hard-core bosons or Tonks-Girardeau gas, an exact approach can be pursued to diagonalize Hamiltonian (3.8). Since multi-occupancy of one site is forbidden by the infinite interaction energy, it can be simplified into

$$H = -t \sum_{i=1}^M (e^{-i\Omega/M} b_i^\dagger b_{i+1} + h.c.) + t \sum_{i=1}^M \Lambda_i n_i^b \quad (\text{D.1})$$

where the bosonic annihilation and creation operators have the additional on-site constraints $b_i^2 = b_i^{\dagger 2} = 0$ and $b_i b_i^\dagger + b_i^\dagger b_i = 1$. By applying the Jordan-Wigner transformation

$$b_j = \prod_{l=1}^{j-1} e^{i\pi f_l^\dagger f_l} f_j ,$$

where f_i (f_i^\dagger) are fermionic annihilation (creation) operators, the Hamiltonian (D.1) can be mapped into the one for spineless fermions:

$$H = -t \sum_{i=1}^M (e^{-i\Omega/M} f_i^\dagger f_{i+1} + h.c.) + t \sum_{i=1}^M \Lambda_i n_i^f \quad (\text{D.2})$$

This Bose-Fermi mapping is the analogous, for a discrete system, of the one introduced by Girardeau for a continuous system [139]. Hamiltonians (D.1) and (D.2) have the same spectrum, but non-trivial differences appear in the off-diagonal correlation functions: $\langle f_i^\dagger f_j \rangle$ vs $\langle b_i^\dagger b_j \rangle$, which we have calculated following the same procedure described in [149]. Such difference affects, for example, the momentum distribution, which is much narrower for hard-core bosonic systems than for non-interacting fermions. The density, and all the quantities related to it, are instead identical. The momentum distribution for the low filling (and one should be in this limit in order to perform Bose-Fermi mapping) is going to behave in the same way as for the Lieb-Liniger model in the hard-core limit, since there is a one to one mapping between this systems in the limit of the low-filling [150]. So again, close to the zero, the momentum distribution behaves as $1/\sqrt{k}$, and in the limit ($k \rightarrow \infty$) it scales as $1/k^4$.

This 1D peculiar strongly correlated TG phase has been demonstrated in several experiments for quasi-one dimensional systems of cold atoms confined in cigar-shaped and lattice potentials [151, 152].

D.2 Exact diagonalization schemes

D.2.0.1 Working in the full Hilbert space

The exact diagonalization (ED) is a computational method in many-body physics [153, 154] which gives exact eigenstates and eigenvalues of the Hamiltonian without making any simplifying assumptions about the physical system. However the method is applicable to small systems and small fillings N/M . The reason for that is provided by the fact that the Hilbert space spanned by the many-particle Fock states cannot be too large. Specif-

D.2. Exact diagonalization schemes

ically, to implement the exact diagonalization, one has to consider all the possible combinations of N particles over M sites, modulo the permutations of identical particles. The dimension of the Hilbert space is given by [155]:

$$D = \frac{(M + N - 1)!}{(M - 1)!N!} \quad (\text{D.3})$$

In Section 5.2, we considered values of the filling: $5/11, 15/11, 24/9$. Correspondingly, the Hilbert space dimensions for that fillings are $3003; 3268760; 10518300$.

The non-diagonal part of the Bose-Hubbard model can be written efficiently with the help of sparse matrices routine. The ground and the first excited state state eigenvalues and eigenvectors of the system can be found explicitly with help of Lanczos algorithm [153, 154].

D.2.0.2 Working in the truncated Hilbert space

To study the system for larger sizes and larger fillings, the exact diagonalization scheme works upon reducing the dimension of the Hilbert space in a controlled way. This is achieved by restricting (truncating) the lattice site occupation number up to some given integer number K . The main difficulty of the truncated ED is the generation of the truncated Hilbert space in a numerically efficient way¹. Here we are using the following algorithm to achieve the goal. At first we write the function $f(M, n, K)$ which splits a positive integer M into a sum of n positive integers (where each of the integers is smaller than K) up to commutativity (so this function is returning matrix). Then we define the number s , where $s = [M/K] + 1$, if $M/K - [M/K] > 0$ and else $s = [M/K]$. Then the truncated Hilbert space

¹One algorithm was suggested in A. Szabados, P. Jeszenski and P. Surjan, Chem. Phys. **401**, 208 (2012). It turns out, however, that that method is not efficient for generation of the big truncated Hilbert spaces ($D_K \sim 10^6$).

Appendix D. Appendix

can be generated in the following 3 steps: 1) to apply function $f(M, n, K)$ by changing n from s to N with a step 1; 2) to concatenate each line in the matrix which return $f(M, n, K)$ with required amount of zeros to make lines of matrix N dimensional arrays; 3) to generate all possible permutations for any line of the matrix. The dimension of the truncated Hilbert space is given by the following expression [4]:

$$D_K = \sum_{i=1}^{\lfloor \frac{N}{K+1} \rfloor} (-1)^j \binom{M+N-1-j(K+1)}{M-1} \binom{M}{j} \quad (\text{D.4})$$

where the brackets $\lfloor \rfloor$ stand for the floor function.

For example for the case of the filling 24/9 and $K = 6$ which is considered in Section 5.2, $D_6 = 2345553$ which is almost 4.5 times smaller the dimension of the full Hilbert space. Indeed, in this way one can reduce D for the several order of magnitudes, but that will introduce errors, especially at small U . Here we estimate the errors in the following way. We calculate the particle number fluctuations (variance) per lattice site

$$\sigma_i = \sqrt{\langle n_i^2 \rangle - \langle n_i \rangle^2} \quad (\text{D.5})$$

We assume that: if $\langle n_i \rangle + 5\sigma_i < K, \forall i$ then error (in calculating expectation values) is smaller than 0.0006%, if $\langle n_i \rangle + 4\sigma_i < K$ then error is smaller than 0.006%, if $\langle n_i \rangle + 3\sigma_i < K$ then error is smaller than 3% and if $\langle n_i \rangle + 2\sigma_i < K$ for any i then error is smaller than 5%. For the filling 24/9 an estimated error for $U = 10$ is less than 0.006% and for $U = 1$ it becomes 5%.

The momentum distribution in Fig. 5.3 is calculated with the scheme detailed above.

D.3 DMRG method

The modified Bose-Hubbard model of Eq. (3.8) can be quite naturally numerically treated by a Density Matrix Renormalization Group (DMRG) approach, i.e., by optimising a Matrix Product State (MPS) representation of the many-body wavefunction [156, 157]. A first requirement, as for almost any numerical treatment of bosons, is to truncate the local Hilbert space down to few states, $d = n_{\max} + 1$, with n_{\max} the maximum allowed particle occupation per site. The MPS ansatz is, at first sight, well suited for periodic boundary conditions [158] but a practical implementation of an algorithm over it has to face a number of subtleties and numerical instabilities [157], especially in the case of a non-homogeneous system, like here. At a difference to another recent work [86], then, it has been decided to opt here not for an explicitly periodic MPS but rather to employ a more standard open boundary (OBC) scheme with a trick. Namely, we represented a ring of M sites as two adjacent stripes of length $M/2$ linked by only two extremal rungs on first and last site.

On one hand, such an approach implies an effective local dimension $d_{\text{eff}} = d^2$, as well as a larger bond dimension m (i.e., the matrix dimension), and therefore a priori an extra cost in the tensor contractions involved in the optimization process. On the other hand, though, it allows us to rely on a unitary gauge from the left and the right border, with deep computational advantages:

- i) The optimization problem can be casted into a standard eigenvalue problem, by means of exact contractions scaling as $O(m^3)$. This has to be confronted with the situation for explicit PBC's: there one has to face the instabilities of a generalised eigenvalue solver, whose defining operators are moreover obtained exactly with $O(m^5)$ operations [158]; approximate,

Appendix D. Appendix

slightly better scaling, strategies for PBC's are also available, but they work best on very long and uniform chains, which is not the case here [159, 160].

- ii) The preservation of quantum numbers related to Abelian symmetries, such as the $U(1)$ particle number, is simple to implement, boost the computational efficiency [156], and eliminates an uncertainty source by not invoking any chemical potential [86].
- iii) The splitting of a two-site (four-legged) optimised tensor into two single-site (three-legged) ones assumes the clear meaning of an entanglement renormalization (from $m d_{\text{eff}}$ to m states), thus giving a quantitative indication of the performed approximation and permitting a dynamical allocation of symmetry sectors inside the tensors [156]. Such features compensate well the extra d_{eff} cost involved in the contractions with respect to single-site optimization.

In our simulations ², we chose the local Hilbert dimension up to $d_{\text{eff}} = 25$ (i.e., $n_{\text{max}} = 4$) in the softer core case $U = 1$: this can be checked “ex post” to be appropriate, by looking at the decay of site occupation probability and confronting it to other approximations incurring in the algorithm. The other main source of numerical uncertainty is given, of course, by the number of states kept in the RG procedure (i.e., the bond dimension of the MPS ansatz): for moderate ring sizes up to 80-100 sites, as considered here, we have seen that $m \simeq 200$ already provides reliable results.

²The data presented in this work have been obtained by an open-source code available at www.dmrg.it

D.3. DMRG method
